UNIVERSITÀ DEGLI STUDI DI PADOVA

Dipartimento di Fisica e Astronomia "Galileo Galilei"

Corso di Laurea Magistrale in Fisica

Tesi di Laurea

Lift-off stress of viscoelastic fluids flowing in herringbones decorated microfluidic channels

Relatore
Ch.mo Prof. Matteo Pierno
Controrelatore
Ch.mo Prof. Alessandro Patelli

Laureando
Andrea Vezzani

Anno Accademico 2019/2020

Contents

Riassunto

In questa tesi è stato studiato il flusso tridimensionale lungo la direzione trasversa di un'emulsione in un canale microfluidico con pareti decorate da microstrutture a spina di pesce su scale spaziali dell'ordine della taglia delle goccie. L'emulsione è un esempio di Soft Glassy Material (SGM), un gruppo di materiali che comprende gel, schiume, creme, paste e fanghi. Questi materiali presentano una complessa reologia, che dipende dalla frazione di volume occupata dai loro costituenti. Studi recenti indicano che, per alte frazioni di volume, il comportamento dei SGM possa essere determinato dal confinamento del sistema per mezzo di una complicata reologia non-locale, e che inoltre si possa controllare specifiche proprietà del flusso di questi materiali tramite microstrutture sulle superfici dei canali. In questa tesi è stato studiata la struttura tridimensionale del flusso in un canale con microstrutture a spina di pesce, la cui asimmetria longitudinale definisce due differenti direzioni di flusso, chiamate *forward* e *backward*.
I risultati mostrano profonde differenze tra i flussi nelle due direzioni, anche a frazioni di volume relativamente basse, un risultato non riportato in letteratura. Questo risultato è rafforzato da esperimenti con un liquido *Newtoniano* ed uno *Shear-thinning*, che mostrano come la differenza osservata non possa essere spiegata né da errori sistematici del sistema di misura, né dalla reologia di *bulk*. Questo suggerisce che la differenza sia in effetti causata da una reologia non-locale, indotta da effetti di taglia finita dei costituenti dell'emulsione, già presente a concentrazioni di volume inferiori a quelle considerate come limite inferiore in letteratura.

Abstract

In this thesis we study the three dimensional cross section of the flow of emulsion in microfluidic channels with walls decorated by herringbone structured grooves with spatial dimension comparable with the droplets size. The emulsion is an example of a Soft Glassy Material (SGM), a class of materials that comprehend also gels, foams, creams, pastes and muds. These materials have a complex rheology, that depends on the volume fractions occupied by the components. Recent studies have suggested that, for high volume fractions, the behaviour of SGMs could be determined by the confinement of the system by means of a complex non-local rheology and that microstructures on the channel surfaces could be used to control specific properties of their flow. In this work we study the three-dimensional structure of the flow in the herringbone pattern decorated channel, whose longitudinal asymmetry defines two different flowing directions, labeled *forward* and *backward*.
The results show profound differences between the flows in the two directions, even at a volume fraction relatively low, a result not reported in literature. This result is reinforced by our tests on a *Newtonian* fluid and a *Shear-thinning* one, that show that neither experimental biases or bulk rheology could be the cause of the difference observed, suggesting that the non-local rheology induced by finite-size effect of the constituents is already present at lower concentrations than those considered as lower limit in literature.

Introduction

The study of the response of materials to external forces is cross-disciplinary, being the intersection point of physics, chemistry, engineering and material science. The comprehension of the physics behind the behaviour of the materials is at the root of many industrial and technological applications. For example, the study of the flow of fluids in microfluidic channels paved the way to the emergence of devices like the Lab-on-a-Chip, a miniaturized laboratory, able to perform many experimental procedures like sample enrichment, mixing, product separation, isolation and analysis on a small quantity of substance and without requiring an entire facility.

It is not always an easy task, however, to understand and predict how a material will respond to a given applied stress: most solid respond with an elastic, reversible deformation, while most fluid cannot sustain a shear stress. There are however materials that can show both this behaviours, solid-like at small applied stresses and liquid like at high stresses. Everyday examples are toothpaste and mayonnaise, but this class of materials include all kind of emulsions, gels, foams, creams, pastes and muds.

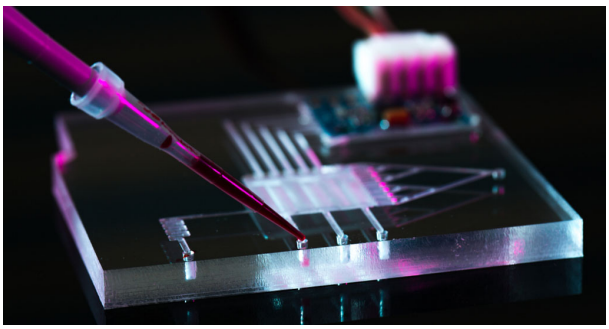

Figure 1: Lab-on-a-Chip device (Lab-on-a-Chip © science photo/shutterstock.com).

These multi-component materials are collectively known as Soft Glassy Materials (SGM), and their study require a comprehension of the mechanical dynamics of the constituents of the dispersed phase, like droplets in emulsions or bubbles in foams. In these materials, the response at an external stress is characterized by successive steps of elastic deformation and plastic rearrangements of the constituents. This is well explored in literature for SGM in which the volume fraction occupied by the dispersed phase is so high that the constituents are in a *jammed* configurations, incapable of moving without disrupting the arrangement of constituents around them. Despite this knowledge, however, the dynamics of these materials at different scales remains a great challenge. Goyon et al. [19] found that the viscosity of emulsion at high volume fractions is not controlled by the bulk rheology but depends on the confinement of the system. Moreover, Mansard [27], Derzsi and Filippi [15, 16] showed that the fluidization of emulsion at high volume fractions can be enhanced or hindered by suitable wall roughness textured on the channel walls. Successive works [32, 61] explored the difference induced in the flow of the emulsion by the use of herringbone decorated channels, characterized by a roughness that is non-symmetric along the longitudinal direction, naturally defining two different flowing directions, labeled *forward* and *backward*.

Currently, no work has addressed the role of the herringbone decoration along the whole cross section of the flow. Aim of this thesis is to explore the effect of herringbone grooves on the three dimensional structure of the flow through both in-flow directions.

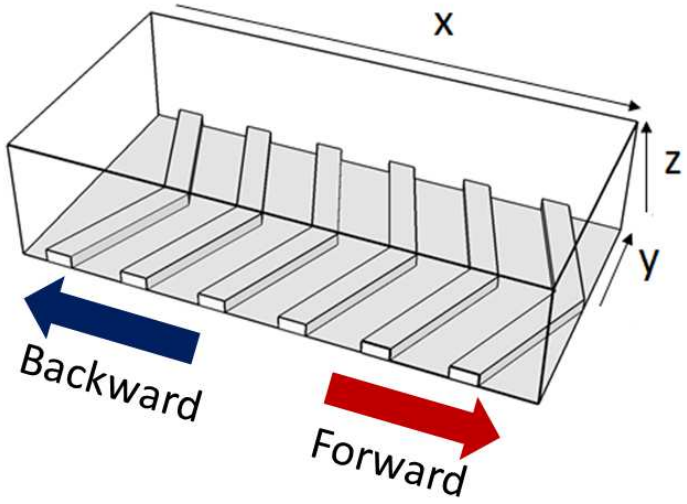

Figure 2: Scheme of a herringbone decorated channel. Picture taken from [17].

Thesis outline:
This thesis is composed by four chapters. The first is dedicated to the introduction to the important literature for this thesis. The second describe the experimental materials, set and procedures. The third present the result obtained and the fourth is the conclusion of this thesis.
First chapter: We give an introduction to the classification and properties of the complex fluids, as well as introducing the fundamental concepts of rheology, the discipline that study the how materials react to external forces, and fluid dynamics, focusing on the peculiarities of the confinement at the microscale.
After that we introduce the Soft Glassy Materials and the emulsions, the focus material for this thesis, detailing their rheology and their flow behaviour in a confined system. The chapter concludes with an overview of the studies on the three-dimensional flow of fluids in the herringbone decorated channel.
Second chapter: We describe the experimental procedure for this work: the fluids used for the experiments, the microfluidic channels, the Micro Particle Tracking Velocimetry, which is the technique used in this thesis to characterize the fluid flow, and the experimental setup, procedure and data analysis to obtain a three dimensional measure of the flow speed in the channels.
Third chapter: We present the three dimensional flow characterization for the emulsion flowing in the forward and backward directions in a herringbone decorated microfluidic channel. We then present the results of the experiment performed with two polymeric solutions characterized by a shear-thinning rheology, which is the same as the emulsion, and pure Glycerine, a Newtonian fluid. The chapter ends with a discussion of the results obtained and an interpretation based on the existing literature available is proposed.
Fourth chapter: This last chapter summarizes and concludes the work of this thesis.

Chapter 1

Complex fluids

In this first chapter we will introduce the foundamental concepts of the *complex* fluids rheology: a generalization of the concept of fluid to all the materials that can *flow*. In section 1.1 we will describe deformation and flow of materials under applied external forces. In section 1.2 we will use those concepts to build a classification for the complex fluids and give a description of the properties of the various classes with the purpose of writing *constitutive equations* for those materials. In section 1.3 we will then make use of these constitutive equations to obtain equations of motion for the fluids of interest for this thesis. We will then proceed to a more in-depth description of the Soft Glassy Materials in section 1.4, and their study in previous works that led to the present thesis in section 1.4.4.

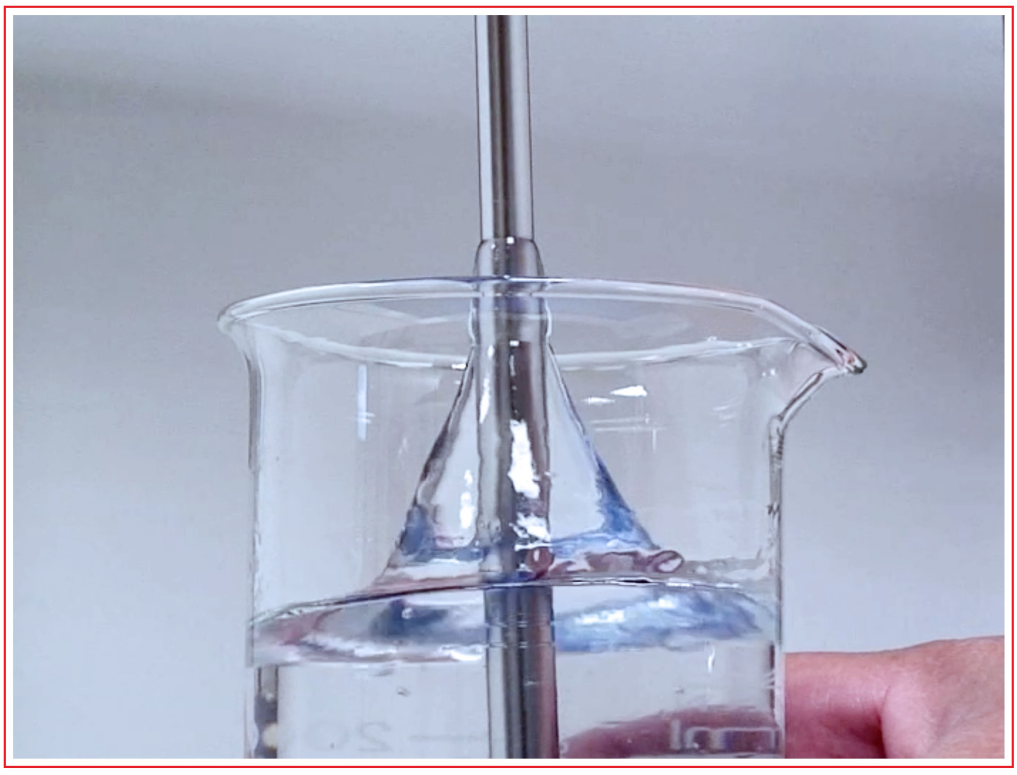

1.1 Complex fluids rheology

When a body is not deformed, all the parts of the body are in mechanical equilibrium and the molecular arrangement is that of a state of thermal equilibrium. When a deformation occurs, the arrangement is modified and the body is no longer in equilibrium. Thus, new forces arise inside the body, due to molecular interactions, trying to return the body to the equilibrium state. This internal forces are called *internal stresses*.
Lets consider the total force acting on a portion of the body: the total force has to be equal to the sum of all the forces acting on all the volume 'sub-elements' of that portion, and so can be written as the integral over the portion:

$$\int \boldsymbol{F} dV \,, \tag{1.1.1}$$

$\boldsymbol{F}$ being the force per unit volume, and $\boldsymbol{F}dV$ the force acting on the volume element dV. When considering the forces that the 'sub-elements' exert on one another, it is clear that their resultant total force must be zero due to Newton's third law. The relevant total force must then be due to the forces exerted on the portion of the body by the portions surrounding it. Since this forces must act on the surface of the portion considered, the resultant can be represented as a surface integral. The integral of a vector over a given volume can be transformed into an integral over the surface surrounding the volume if the vector is the divergence of a tensor of rank two. The three components of vector $\boldsymbol{F}$ must then have the form:

$$F_i = \frac{\partial T_{ik}}{\partial x_k} \,. \tag{1.1.2}$$

The tensor $\mathbf{T} = T_{ik}$ is the *total stress tensor*.

Pressure and Stress tensor $\boldsymbol{\sigma}$

A particular case of total stress tensor is the uniform pressure p. It is a uniform normal stress $T_{11} = T_{22} = T_{33}$, and is the only stress that can be sustained by a fluid at rest without flowing. So, for a fluid at rest, the total stress tensor reads as:

$$\mathbf{T} = \begin{bmatrix} -p & 0 & 0 \\ 0 & -p & 0 \\ 0 & 0 & -p \end{bmatrix} = -p \cdot \begin{bmatrix} 1 & 0 & 0 \\ 0 & 1 & 0 \\ 0 & 0 & 1 \end{bmatrix} = -p \cdot \mathbf{I} \,. \tag{1.1.3}$$

The negative sign is used because compression is considered to be negative. Generally, when dealing with nearly incompressible materials, the overall pressure cannot influence material behaviour. It thus make sense to substract the effect of pressure from the total stress tensor:

$$\mathbf{T} = -p \cdot \mathbf{I} + \boldsymbol{\sigma} \,. \tag{1.1.4}$$

The tensor $\boldsymbol{\sigma}$ is called *stress tensor* or *viscous stress tensor* and contains all the effects of deformation on the material. Since with experiments we can only measure forces that, once divided by the area, give the components of $\mathbf{T}$, we are interested in removing the pressure term from $\mathbf{T}$. This is not a problem for the *shear* terms, for which:

$$T_{ik} = \sigma_{ik} \,, \tag{1.1.5}$$

but the *tensile* or normal terms will differ by an additional term p:

$$T_{ii} = -p + \sigma_{ii} \,. \tag{1.1.6}$$

To solve this problem we use stress *differences*:

$$T_{11} - T_{22} = \sigma_{11} - \sigma_{22} \tag{1.1.7}$$

$$T_{22} - T_{33} = \sigma_{22} - \sigma_{33}\,. \tag{1.1.8}$$

The third difference $T_{11} - T_{33}$ is usually not considered as is just the sum of the other two.
To obtain an expression for the stress tensor $\boldsymbol{\sigma}$ it is necessary to have a mathematical description of the deformation inside the material. This is a vast and complex subject, in this thesis we will focus on the simple shear stress, when 'planes' of material glide over each other. In fig. 1.1, we can see an example of simple shear deformation. The planes of material slide in the $\hat{\boldsymbol{x}}_1$ direction.

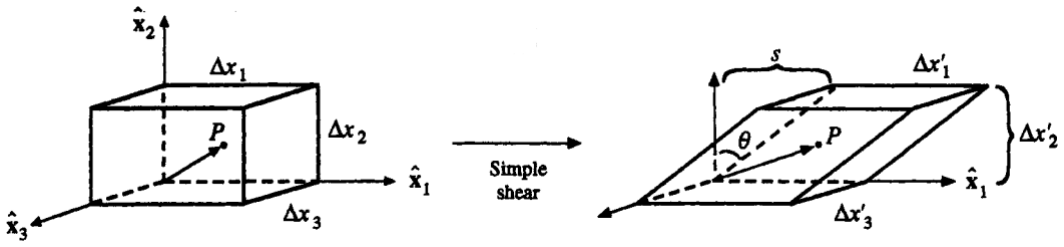

Figure 1.1: A block of material undergoing simple shear stress in $\hat{\boldsymbol{x}}_1$ direction. Adapted from [26].

In the case of simple shear the differences $T_{11} - T_{22}$ and $T_{22} - T_{33}$ are denoted as

$$T_{11} - T_{22} = N_1 \quad \text{and} \quad T_{22} - T_{33} = N_2\,. \tag{1.1.9}$$

with N_1 being called *first normal difference* and N_2 *second normal difference*.

The displacement of P, using the notation shown in fig. 1.1, reads as:

$$x'_1 = x_1 + \frac{s}{\Delta x_2} x_2 = x_1 + \gamma x_2 \tag{1.1.10}$$

$$x'_2 = x_2 \tag{1.1.11}$$

$$x'_3 = x_3\,, \tag{1.1.12}$$

where $\gamma = s/\Delta x_2$ is called *shear strain*. The *rate of deformation tensor* $\mathbf{D}$ is a symmetric tensor [26] that describe the rate of stretching inside the material. It is possible to show [26] that in the case of a simple shear stress the rate of deformation tensor $\mathbf{D}$ becomes:

$$2\mathbf{D} = \begin{bmatrix} 0 & \dot{\gamma} & 0 \\ \dot{\gamma} & 0 & 0 \\ 0 & 0 & 0 \end{bmatrix}\,, \tag{1.1.13}$$

where $\dot{\gamma} = \mathrm{d}\gamma/\mathrm{d}t$ is called *shear rate*. We have written the expression for $2 \cdot \mathbf{D}$ instead of the simple $\mathbf{D}$ to follow the most common notation [26].
If a fluid is subjected to a simple shear stress it is put in motion in a *simple shear flow*, as depicted in fig. 1.2.

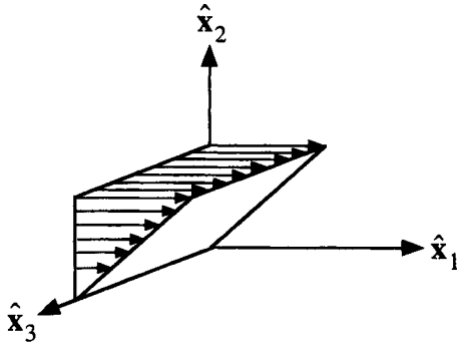

Figure 1.2: Velocity profile in a simple shear flow. Adapted from [26].

If we choose a coordinate system in which the fluid flow direction is along one axis, such as $\hat{\mathbf{x}}_\mathbf{1}$ in fig. 1.2, and assuming simmetry in the $\hat{\mathbf{x}}_3$ the expression of the shear rate $\dot{\gamma}$ reduces to:

$$\dot{\gamma} = \frac{\delta \mathbf{u}(x_2)}{\delta \mathbf{x}_2}\,, \tag{1.1.14}$$

where $\mathbf{u}(x_2)$ is the velocity profile of the fluid flow.

Invariants of $2\mathbf{D}$

Like any symmetrical tensor $2\mathbf{D}$ can be diagonalized at any given point. Physically, it means that is always possible to find a system of coordinates in which $2\mathbf{D}$ has only diagonal components, and thus all the shear components equal to zero. It is to be noted, that if the tensor $2\mathbf{D}$ is diagonalized at a point P, it will be in general not diagonal at any other point.

We are interested in finding quantities that are independent on the choice of coordinates. We do so by solving the characteristic equation of $2\mathbf{D}$:

$$\det(2\mathbf{D} - \lambda \mathbf{I}) = 0\,. \tag{1.1.15}$$

By expanding the determinant we obtain:

$$\lambda^3 - I_{2\mathbf{D}}\lambda^2 + II_{2\mathbf{D}}\lambda - III_{2\mathbf{D}} = 0\,. \tag{1.1.16}$$

The coefficients:

$$I_{2\mathbf{D}} = \mathrm{tr} 2\mathbf{D} \tag{1.1.17}$$

$$II_{2\mathbf{D}} = \frac{1}{2}[I_{2\mathbf{D}}^2 - \mathrm{tr}(2\mathbf{D})^2] \tag{1.1.18}$$

$$III_{2\mathbf{D}} = \det 2\mathbf{D}\,, \tag{1.1.19}$$

are called *first invariant* ($I_{2\mathbf{D}}$), *second invariant* ($II_{2\mathbf{D}}$) and *third invariant* ($III_{2\mathbf{D}}$) of the tensor $2\mathbf{D}$. They retain the same value whichever system of coordinates is chosen to express $2\mathbf{D}$. For the case of simple shear stress, the invariants are:

$$I_{2\mathbf{D}} = 0 \tag{1.1.20}$$

$$II_{2\mathbf{D}} = -\dot{\gamma}^2 \tag{1.1.21}$$

$$III_{2\mathbf{D}} = 0\,. \tag{1.1.22}$$

1.2 Complex fluids

With the term *complex fluids* we indicate all the materials that can *flow*. The complex fluids comprehend a vast range of materials, and in the following sections we will give a brief introduction to the subject, while elaborate on those materials more relevant to this thesis.
Broadly speaking, complex fluids can be divided in three main categories:

- Time-independent fluids;
- Time-dependent fluids;
- Viscoelastic fluids.

1.2.1 Time-independent fluids

The fluids that belong to this category are also called *generalized Newtonian* fluids. The fundamental property of those materials is that it exist a functional dependence between $\dot{\gamma}$ and σ. We can thus write:

$$\dot{\gamma} = f(\sigma) \quad \text{or} \quad \sigma = f^{-1}(\dot{\gamma})\,. \tag{1.2.1}$$

The generalized Newtonian fluids can be further divided in categories. A graphic representation of those categories by means of their $\sigma - \dot{\gamma}$ characteristic is reported in fig. 1.3.

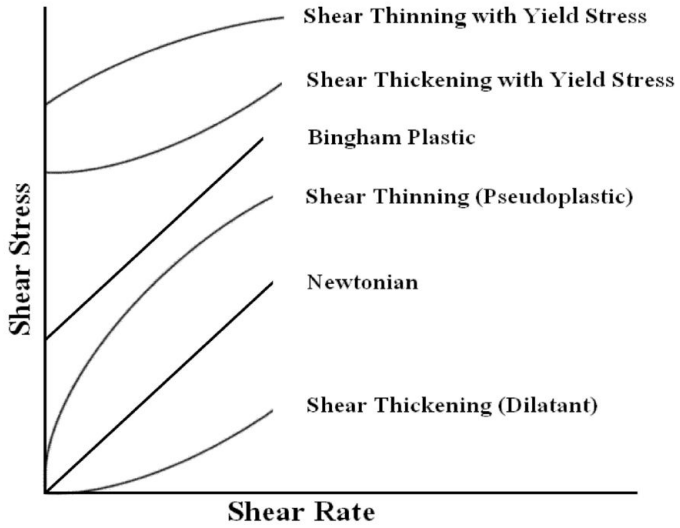

Figure 1.3: Schematic representation of the classes of fluids and viscoplastic materials with relative nomenclature.

The generalized Newtonian fluids for which the $\sigma(\dot{\gamma})$ intercept the origin are called *general viscous fluids*. The ones that does not are called *viscoplastic fluids*, and are characterized by a threshold shear stress called *yield stress*. We will begin by describing the general viscous fluid and in particular the *Newtonian* fluid, for which we will give the definition of *viscosity*. In the case of a Newtonian fluid, the viscosity will be constant

with respect to the shear rate $\dot{\gamma}$. In general, for a vast range of fluids, viscosity is not a constant but rather a function of the rate of deformation. For these kind of materials we define the *apparent* viscosity as $\eta = \sigma/\dot{\gamma}$. Those materials are known as *Non-Newtonian* fluids and make up all the other complex fluids that we will describe.

General viscous fluids The general viscous fluids are divided in three main categories: *Newtonian* fluids, *shear thinning* or *pseudoplastic* fluids and *shear thickening* or *dilatant* fluids.

- Newtonian fluids: A Newtonian fluid is defined as a fluid in which the stress arising from a flow is linearly correlated to the rate of change of its deformation over time [23]. The constitutive equation for Newtonian fluids is the Newton's law [26]:

$$\boldsymbol{\sigma} = \eta 2\mathbf{D}\,, \tag{1.2.2}$$

that, in terms of the total stress $\mathbf{T}$ is:

$$\mathbf{T} = -p\mathbf{I} + \eta 2\mathbf{D}\,. \tag{1.2.3}$$

The proportionality term η in eq. (1.2.2) is called *viscosity*. The viscosity strongly depends on the intrinsic characteristics of the fluid considered, such as molecular weight and inter molecular forces. Its values span greatly between different materials, for example, the viscosity of air is $\eta \sim 10^{-5}\,\mathrm{Pa\,s}$, while that of glycerol is $\eta \sim 1.5\,\mathrm{Pa\,s}$. In a Newtonian fluid, η is constant. If we consider the steady simple shear flow of eq. (1.1.13), eq. (1.2.2) becomes:

$$\mathbf{T} = -p\begin{bmatrix}1 & 0 & 0\\ 0 & 1 & 0\\ 0 & 0 & 1\end{bmatrix} + \eta\begin{bmatrix}0 & \dot{\gamma} & 0\\ \dot{\gamma} & 0 & 0\\ 0 & 0 & 0\end{bmatrix}\,. \tag{1.2.4}$$

Hydrostatic pressure is the only normal stress in a steady shear flow. The normal differences of eq. (1.1.9) are zero.
Usually, the eq. (1.2.2) is written in its scalar form:

$$\sigma_{12} = \sigma_{21} \equiv \sigma = \eta\dot{\gamma}\,. \tag{1.2.5}$$

- Shear thinning fluids: This is the most common type of generalized Newtonian fluid, and are characterized by a gradual decrease of the viscosity η as the shear rate increases. This imply that the fluid flows more easily when the shear rate increases. The shear thinning fluids behave similarly to Newtonian fluids at low shear rates, in fact, in this region the viscosity is almost independent from the shear rate. This limit is called η_0. In shear thinning polymer solutions it is observed that also at high shear rates the viscosity approach a limit value, i.e. a Newtonian plateau, called η_∞. An example of this behaviour can be seen in fig. 1.5.

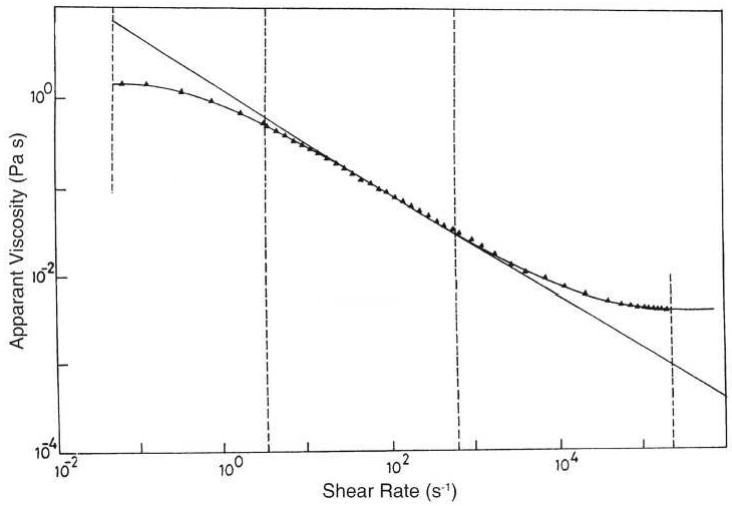

Figure 1.4: The apparent viscosity η as a function of the shear rate $\dot{\gamma}$ for a polymer solution. We can see the curve approaching both the η_0 and the η_∞ plateau at low and high shear rates. Adapted from [12]

The origin of this thinning behaviour lies in the physical structure of the material considered. In the polymer solution case, in fig. 1.5 we can see a qualitative description of the phenomenon that causes the apparent viscosity variation. At low shear rates, the polymer chains are entangled and coiled. As we increase the shear rate, the chains start to disentangle and stretch in the direction of the flow. At some point, if we keep increasing the shear rate, all the chains are disentangled and aligned with the flow: the fluid is free to flow easily.

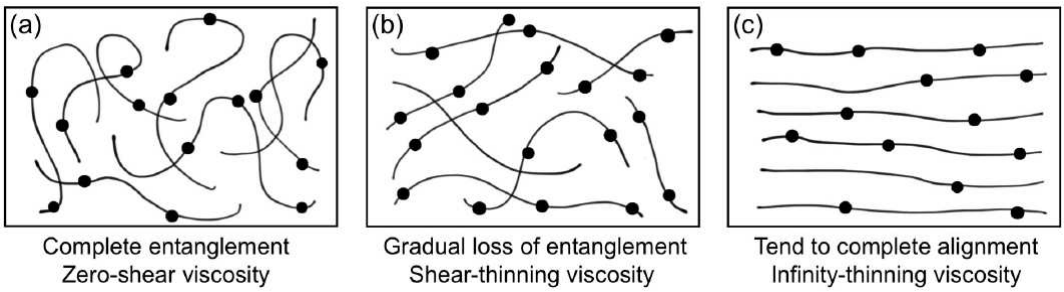

Figure 1.5: Schematic representation of polymer chains under the influence of shear. Picture taken from [17]

- Shear thickening fluids: The shear thickening fluids are characterized by the increase of the apparent viscosity as the shear rate increases. In this case we can give a qualitative explanation for the physical origin of the behaviour in the case of the suspensions. When the shear rate is low, the motion of the particles is slow enough so that the continuous phase is able to efficiently fill the voids between them and acts as a lubricant that ease the flow of the fluid. The resulting stress is thus low. If we increase the strain rate the fluid *dilates* and the continuous phase is not enough anymore to lubricate efficiently all the solid particles. This results in a solid-solid friction that increase the shear stress and thus the apparent viscosity. For the shear thickening fluids, is not possible to say if the limit values η_0 and η_∞ of the apparent viscosity exist or not [12].

The mathematical model for the *general viscous fluid* start from a different constitutive equation than eq. (1.2.2):

$$\mathbf{T} = f(2\mathbf{D})\,. \tag{1.2.6}$$

Expanding eq. (1.2.6) in a power series we get:

$$\mathbf{T} = f_0\mathbf{D}^0 + f_1\mathbf{D}^1 + f_2\mathbf{D}^2 + \dots\,. \tag{1.2.7}$$

Note that $\mathbf{D}^0 = \mathbf{I}$ and, for an incompressible fluid, $f_0 = -p$. Using the Cayley-Hamilton theorem [11] and a result from Rivlin [45] we get eq. (1.2.7) to the form:

$$\mathbf{T} = -p\mathbf{I} + \eta_1(II_{\mathbf{2D}}, III_{\mathbf{2D}})2\mathbf{D} + \eta_2(II_{\mathbf{2D}}, III_{\mathbf{2D}})(2\mathbf{D})^2\,, \tag{1.2.8}$$

where η_1 and η_2 are functions of the (non-zero) invariants of $2\mathbf{D}$. Equation (1.2.8) is known as Reiner-Rivlin fluid equation [26]. We can see that the Newtonian fluid is a special case of eq. (1.2.8) with:

$$\eta_1(II_{\mathbf{2D}}, III_{\mathbf{2D}}) = \eta = \text{const} \quad \text{and} \quad \eta_2(II_{\mathbf{2D}}, III_{\mathbf{2D}}) = 0\,. \tag{1.2.9}$$

The term with η_2 would give rise to normal stresses in shear flows, i.e. diagonal terms in the stress tensor, but the results qualitatively disagree with experimental observations [26]. Thus, it is usually discarded. The general viscous fluid equation then becomes:

$$\mathbf{T} = -p\mathbf{I} + \eta(II_{\mathbf{2D}}, III_{\mathbf{2D}})2\mathbf{D}\,, \tag{1.2.10}$$

Since we will be mostly concern with simple shear stress flow, where we found $III_{\mathbf{2D}} = 0$ (eq. (1.1.22)), we will examine functional form for η assuming $\eta(II_{\mathbf{2D}})$ only:

$$\mathbf{T} = -p\mathbf{I} + \eta(II_{\mathbf{2D}})2\mathbf{D} \quad \text{or} \quad \boldsymbol{\sigma} = 2\eta(II_{\mathbf{2D}})\mathbf{D}\,. \tag{1.2.11}$$

The most widely used form for eq. (1.2.11) is the **Power law model**:

$$\sigma_{ij} = A|II_{\mathbf{2D}}|^{(n-1)/2}2D_{ij}\,. \tag{1.2.12}$$

In the steady simple shear, recalling eq. (1.1.13) and eq. (1.1.21), eq. (1.2.12) becomes:

$$\sigma_{12} = \sigma_{21} = A\dot{\gamma}^n\,, \tag{1.2.13}$$

where A is called *flow consistency index*, n is the *flow behavior index*. Therefore, by choosing for the apparent viscosity η:

$$\eta = A\dot{\gamma}^{n-1}\,, \tag{1.2.14}$$

we recover the functional expression for the stress given by eq. (1.2.5). For a shear thinning fluid we have $n < 1$, while for a shear thickening one $n > 1$.

A well known issue of the power law is that it fails to describe the low and high shear rate regions for the shear thinning fluids [26]. Since n is less than one, at low shear rate η goes to infinity rather than to a constant η_0. Also the second plateau η_∞ is not described by the power law model.
Other models have been proposed to overcome this limit and give the Newtonian limits η_0 and η_∞:

- **Cross model:** A common approach is given by the Cross model [13]:

$$\frac{\eta - \eta_\infty}{\eta_0 - \eta_\infty} = \frac{1}{1 + (K^2 |II_{2\mathbf{D}}|)^{(1-n)/2}}\,, \tag{1.2.15}$$

  This equation becomes, in simple shear flow:

$$\frac{\eta - \eta_\infty}{\eta_0 - \eta_\infty} = \frac{1}{1 + (K\dot{\gamma})^{(1-n)}}\,, \tag{1.2.16}$$

  whose boundaries are η_0 for low $\dot{\gamma}$, η_∞ for high $\dot{\gamma}$ and for intermediates shear rates it has a the power law region where:

$$(\eta - \eta_0) \simeq (\eta_0 - \eta_\infty)(A\dot{\gamma})^{n-1}\,, \tag{1.2.17}$$

$$A = K^{n-1}\,. \tag{1.2.18}$$

- **Yasuda-Carreau model:** Another model has been proposed by Yasuda et al. [9] to fit even better the data:

$$\frac{\eta - \eta_\infty}{\eta_0 - \eta_\infty} = \frac{1}{[1 + (\lambda |II_{2\mathbf{D}}|^{1/2})^a]^{(1-n)/a}}\,, \tag{1.2.19}$$

  that in simple shear flow becomes:

$$\frac{\eta - \eta_\infty}{\eta_0 - \eta_\infty} = \frac{1}{[1 + (\lambda\dot{\gamma})^a]^{(1-n)/a}}\,. \tag{1.2.20}$$

  This equation adds to the Cross model a fifth parameter a. When $a = 2$ eq. (1.2.20) is known as Carreau model. The Cross and Yasuda models are reliable in a wide rage of $\dot{\gamma}$, correctly giving both the low and high shear rates Newtonian plateaus.

- **Ellis model:** Frequently the high shear rate region is not observed, and the η_∞ is set to 0 in eq. (1.2.16), giving a three parameters model. This is known as Ellis model:

$$\frac{\eta}{\eta_0} = \frac{1}{1 + (K\dot{\gamma})^{1-n}}\,. \tag{1.2.21}$$

  The Ellis model is simple enough to allow analytical solution of some complex flow problems [26] and is reliable in the low to intermediate $\dot{\gamma}$ region.

Viscoplastic fluids Many materials have a *plastic* behaviour, showing no deformation up to a certain stress, called *yield stress* σ_y, but flowing readily for higher stresses. Ketchup, mayonnaise and house paint are common examples of this behaviour. These materials are called *viscoplastic*. In many cases, stress is not constant inside a body, and for a viscoplastic material this means that different parts of it will behave differently. In specific the portions of it that correspond to stresses that exceed σ_y will flow, while others, correspondent to $\sigma < \sigma_y$, will form solid-like plugs.
It has been hypothesized that for low $\dot{\gamma}$ there might be a Newtonian regime intead of a Hookean one, leading to a *two-viscosity* interpretation. In this context, σ_y would be a result of instrument limitations, and not a physical reality [4].
We saw that the viscous fluids can be roughly classified in three categories, based on the $\eta(\dot{\gamma})$ behaviour: shear thinning, Newtonian and shear thickening. The same classification holds for the viscoplastic materials, depending on the flow behaviour above the yield stress.

- Newtonian viscoplastic fluid: The viscoplastic materials that behave like a Newtonian fluid above the yield stress are called *Bingham plastics*. In Bingham's original paper [8] he proposed a simple model:

$$\dot{\gamma} = 0 \quad \text{for} \quad \sigma < \sigma_y \,, \tag{1.2.22}$$

and

$$\sigma = \eta\dot{\gamma} + \sigma_y \quad \text{for} \quad \sigma \geq \sigma_y \,. \tag{1.2.23}$$

This can be generalized by letting the material behave like a *Hookean* solid for $\sigma < \sigma_y$:

$$\sigma = G\gamma \quad \text{for} \quad \sigma < \sigma_y \,, \tag{1.2.24}$$

and

$$\sigma = \eta\dot{\gamma} + \sigma_y \quad \text{for} \quad \sigma \geq \sigma_y \,. \tag{1.2.25}$$

- Shear thinning and Shear thickening viscoplastic fluids: There exist many models [26] created to describe materials that combine the presence of a yield stress with a non linear rheology (pseudoplastic or dilatant). One of the most common approach is the *Herschel-Bulkley* model. Following the *two-viscosity* interpretation, Herschel and Bulkley proposed, in 1926, a model for viscoplastic material. Instead of a yield stress σ_y, they used a *critical shear rate* $\dot{\gamma}_c$. The model also integrated the power law model (eq. (1.2.12)) to describe a broader range of materials. In the three-dimensional form the Herschel-Bulkley model is:

$$\boldsymbol{\sigma} = 2\eta\mathbf{D} \quad \text{for} \quad II_{2\mathbf{D}}^{1/2} < \dot{\gamma}_c \,, \tag{1.2.26}$$

and

$$\boldsymbol{\sigma} = \left[\frac{\sigma_y}{|II_{2\mathbf{D}}|^{1/2}} + A|II_{2\mathbf{D}}|^{(n-1)/2}\right] 2\mathbf{D} \quad \text{for} \quad II_{2\mathbf{D}}^{1/2} \geq \dot{\gamma}_c \,. \tag{1.2.27}$$

There is another model that is often called 'Herschel-Bulkley': it comes from eq. (1.2.22) and eq. (1.2.23) and incorporates the power law model of eq. (1.2.13). It usually given in the shear flow form:

$$\dot{\gamma} = 0 \quad \text{for} \quad \sigma < \sigma_y \,, \tag{1.2.28}$$

and

$$\sigma = \eta\dot{\gamma}^n + \sigma_y \quad \text{for} \quad \sigma \geq \sigma_y \,. \tag{1.2.29}$$

A contribution from Papanastasiou [39], incorporate into eq. (1.2.27) an exponential, with the purpose of avoiding the discontinuity in the flow curve due to the yield criterion. The Herschel-Bulkley model with Papanastasiou modification is:

$$\boldsymbol{\sigma} = \left[\frac{\sigma_y(1 - \exp(-a|II_{2\mathbf{D}}|^{1/2}))}{|II_{2\mathbf{D}}|^{1/2}} + A|II_{2\mathbf{D}}|^{(n-1)/2}\right] 2\mathbf{D} \,. \tag{1.2.30}$$

Both the use of $\dot{\gamma}_c$ instead of σ_y and Papanastasiou modification has been shown to be extremely beneficial to numerical simulations [1, 7].

1.2.2 Time-dependent fluids

These materials includes fluids that are not described by eq. (1.2.1). The apparent viscosity of this class of materials depends on the kinematic history. Moreover, generally the apparent viscosity η is a function of both the shear rate $\dot{\gamma}$ and the stress σ. A severe consequence of this is that experimental measures of the viscosity are heavily influenced by the applied experimental procedure. Different values of the viscosity η would be measured for different duration of the stress applied. These materials can be classified into two groups: *thixotropic* and *rheopectic* fluids. A thixotropic fluid has its apparent viscosity decreasing with the duration of the shearing. Microscopically, we could explain this phenomenon by considering the progressive braking of the inner structure of the material as the shear continues to be applied [35]. This breaking reduce the number of bonds between particles, and causes a decrease of the viscosity. For these materials a dynamic equilibrium is still possible, if the rate of bonds breaking is equal to the rate of bonds re-building.
On the opposite side, if the apparent viscosity increases with the duration of the applied shear, the material is called a rheopectic fluid. For these materials the formation of internal bonds is promoted by the application of a shear. This causes the increase of the apparent viscosity while the shear is applied [51].

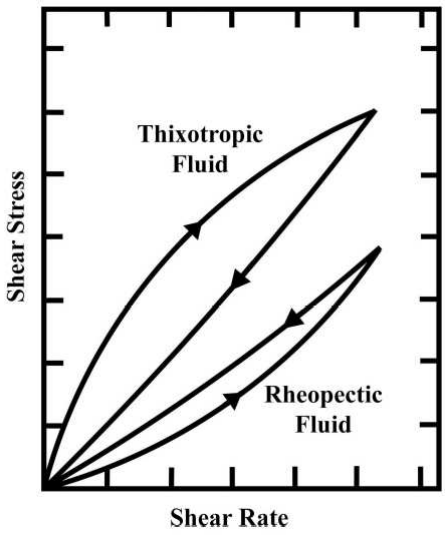

Figure 1.6: Scheme representing the different behaviour of a rheopectic and a thixotropic fluid. It is possible to see the hysteresis that indicate a dependence on the history of the fluid. Image adapted from [12]

1.2.3 Viscoelastic fluids

A viscoelastic fluid is a material that combine the elastic response typical of Hookean solids with the viscous one of liquids. This is the case for all the polymeric materials. When subject to a stress, a viscoelastic material will rapidly deform like an elastic solid, but then it will undergo a continuous deformation, much like a viscous fluid. This means that every viscoelastic material show a time-dependent behaviour. In fig. 1.7 are represented the responses to a step increase in strain γ for the Hookean solid, the Newtonian fluid and a viscoelastic one. The viscoelastic fluid stress *relaxes* to zero over time in an

exponential fashion. A viscoelastic *solid* would relax to a finite stress σ_{ves} instead. This behaviour led to the concept of *stress relaxation*.

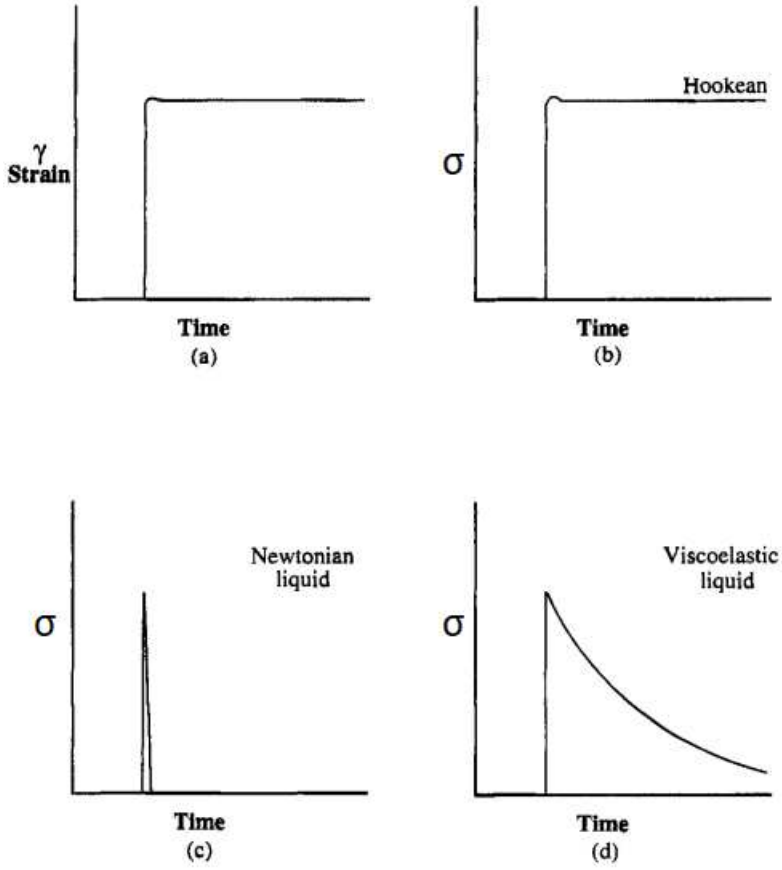

Figure 1.7: Stress response for three classes of materials to a step increase in strain γ as in (a). In (b) we see the response of a Hookean solid, with no variation as long as the strain is acting on the material. In (c) the response of Newtonian fluid: as the strain became constant, the stress drops immediately to zero. Lastly, the viscoelastic fluid response, that decrease in an exponential fashion over time. Adapted from Macosko [26].

We can introduce a *relaxation modulus* $G(t)$, also called *Young modulus*:

$$G(t,\gamma) = \frac{\sigma(t,\gamma)}{\gamma}\,. \tag{1.2.31}$$

For small strains, usually $\gamma < 0.5$ for polymeric liquids, the relaxation modulut G is actually independent on the strain γ [26]:

$$G(t,\gamma) = G(t)\,. \tag{1.2.32}$$

Equation (1.2.32) is called the *linear viscoelasticity* equation. For larger strains eq. (1.2.32) is no longer valid and we have to rely on the general eq. (1.2.31), the *nonlinear viscoelasticity* equation.

Linear viscoelasticity: We start the description of the linear viscoelastic fluid behaviour by deriving a one-dimensional constitutive model. Considering a small variation in stress due to a change of imposed strain, eq. (1.2.32) becomes:

$$\mathrm{d}\sigma = G\mathrm{d}\gamma\,, \tag{1.2.33}$$

which we can write as:

$$\mathrm{d}\sigma = G\frac{\mathrm{d}\gamma}{\mathrm{d}t}\mathrm{d}t = G\dot{\gamma}\mathrm{d}t\,. \tag{1.2.34}$$

We can describe any deformation in the material as the integral over all past times of the infinitesimal deformations:

$$\int_0^\sigma \mathrm{d}\sigma = \sigma = \int_{-\infty}^t G(t-t')\dot{\gamma}(t')\mathrm{d}t'\,, \tag{1.2.35}$$

where the *past* time t' is the variable of integration. We need to choose a functional form for $G(t)$. A first approach would be that of an exponential decay [26]:

$$G(t) = G_0 e^{-t/\lambda}\,, \tag{1.2.36}$$

where λ is the *relaxation time*. Equation (1.2.35) with $G(t)$ given in eq. (1.2.36) is called single relaxation or simple Maxwell model. This model usually does not fit the data very well. It can be improved by using more than one relaxation time:

$$G(t) = \sum_{k=1}^{N} G_k e^{-t/\lambda_k}\,. \tag{1.2.37}$$

If we put eq. (1.2.37) in eq. (1.2.35) we obtain the *general linear viscoelastic model*:

$$\sigma = \int_{-\infty}^t \sum_{k=1}^{N} G_k e^{-(t-t')/\lambda_k}\dot{\gamma}(t')\mathrm{d}t'\,. \tag{1.2.38}$$

Using non-linear regressing methods, this model can fit experimental data quite well [26]. Equation (1.2.35) can be readily put in three dimensional form:

$$\boldsymbol{\sigma} = \int_{-\infty}^t G(t-t')2\mathbf{D}(t')\mathrm{d}t'\,. \tag{1.2.39}$$

As we saw in eq. (1.1.13), for simple shear the tensor $2\mathbf{D}$ does not have diagonal terms, so this linear viscoelastic model cannot predict normal stresses in shear flow.

Nonlinear viscoelasticity: In section 1.2.3, we saw that the Reiner-Rivlin fluid of eq. (1.2.8), and every model derived from it, are unable to predict the normal stresses observed in shear flow experiments. We have also said previously in this section that the linear viscoelastic model is also inadequate at this task. Those normal stresses, and the associated normal differences of eq. (1.1.9), are manifestations of a *nonlinear rheology*. This is an extremely vast subject, and still not well understood [26], thus we will not elaborate on the of the many theoretical and empirical models that has been proposed in literature [26], due to their limitations: every model must be accurately studied for the material considered and it is not possible to generalize it to the entire viscoelastic category.

1.3 Physics of fluids in a laminar flow

The physics of fluids observed at the microscopic scale is very different than its macriscopic counterpart. While flowing in microfluidic channels, the reduced dimensions allow for the

manifestation of molecular effect that would have been negligible at bigger scales. One of the consequences is that it is very hard to induce turbulence in a microfluidic flow. This can be seen by considering the *Reynolds number* (Re) of the system. For a system with a single characteristic spatial scale L, the Reynolds number reads as [23]:

$$Re = \rho \frac{uL}{\eta}\,, \tag{1.3.1}$$

where ρ is the density of the fluid, u its velocity and η its viscosity. In a typical microfluidic channel L is of the order of $100\,\mu$m. If the fluid considered is water ($\rho = 1000\,\mathrm{kg/m^3}$, $\eta = 10^{-3}\mathrm{Pa\,s}$) moving at few mm/s the Reynolds number is $Re \sim 0.1$. A Reynolds number less than 2100 is indicative of a *laminar flow*, in which the fluid particles follows smooth paths in adjacent layers, with each layer moving smoothly past the next ones with little or no mixing. This allows for exceptional experimental control of the flow inside the channel.

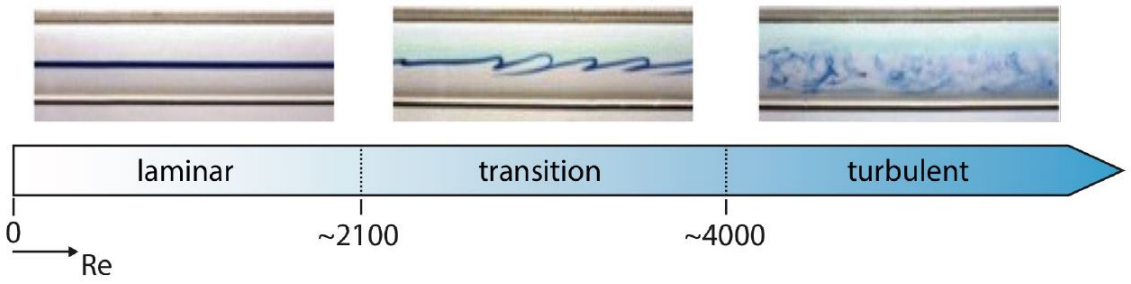

Figure 1.8: Transition from laminar to turbulent flow. The lower arrow indicate the relative Reynolds number. Adapted from [17].

1.3.1 Hydrodynamics at the microscale

In the following treatment, we will consider the fluid as a continuum. This means that it is possible to define a "fluid particle", that is, a volume region containing a large number of the particles constituting the fluid that is much smaller than the size of the system. This means that we are integrating all the quantum and molecular fluctuation in our formalism. At the microscale, for most materials, this is an acceptable approximation [23]. The two differential equations that constitute the hydrodinamic model are the *continuity equation*:

$$\frac{\partial \rho}{\partial t} + \nabla(\rho \mathbf{u}) = 0\,, \tag{1.3.2}$$

and the *Navier-Stokes* equation:

$$\rho\left(\frac{\partial \mathbf{u}}{\partial t} + \mathbf{u}\nabla\mathbf{u}\right) = \mathbf{F}_{ext} + \nabla\sigma\,, \tag{1.3.3}$$

where ρ is the fluid density, $\mathbf{u}$ the fluid velocity, $\mathbf{F}_{ext}$ the external forces acting on the fluid and **sigma** is the stress tensor defined in section 1.1.
The Navier-Stokes equation is a vectorial differential equation for which an analytical solution is still missing. While for practical application usually it is solved by numerical means, in special geometry and with opportune boundary conditions it can be solved. In particular, it can be solved for the flow between two infinite parallel planes, a geometry called *Hele-Shaw*. The microfluidic channels used for this thesis that will be described in chapter 2 are well described by this approximation [17].

1.3.2 Hele-Shaw flow for a Newtonian fluid

For a Newtonian fluid the constitutive equation is that of eq. (1.2.5), when substitute in eq. (1.3.3) we obtain:

$$\rho\left(\frac{\partial \mathbf{u}}{\partial t}+\mathbf{u}\nabla\mathbf{u}\right)=\mathbf{F}_{ext}-\nabla p+\eta\nabla^2\mathbf{u}\,, \tag{1.3.4}$$

where ∇p is the pressure (p) gradient and $\eta\nabla^2\mathbf{u}$ the viscous force. For a steady state fluid with $Re << 1$, it is possible to show [23] that the inertial term $\mathbf{u}\nabla\mathbf{u}$ is negligible. The Navier-Stokes equation then reduces to the *Stokes* equation:

$$\mathbf{F}_{ext}-\nabla p+\eta\nabla^2\mathbf{u}=0\,. \tag{1.3.5}$$

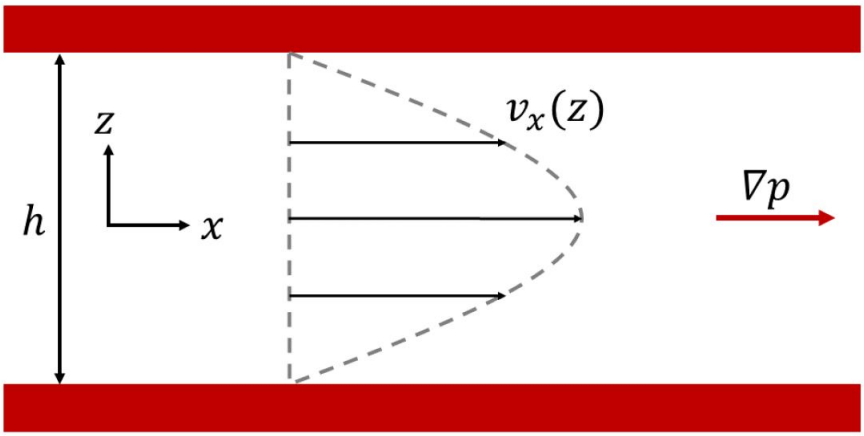

Figure 1.9: Schematic representation of the Hele-Shaw geometry. The velocity profile represented is the parabolic flow typical of a Newtonian fluid. Figure reproduced from [32].

For a Hele-Shaw flow, with the plates separated by a distance h along the z direction as in fig. 1.9, the velocity $\mathbf{u}$ has only one non zero component:

$$\mathbf{u}=(u(z),0,0)\,, \tag{1.3.6}$$

where z is the transverse direction normal to the direction of the flow. If the flow is fully developed, we are in a steady state and we have no variation in time and in x, y directions.

$$\frac{\partial}{\partial t}=\frac{\partial}{\partial x}=\frac{\partial}{\partial y}=0\,. \tag{1.3.7}$$

Since the parallel plates are infinite, the flow is completely independent of y, and thus we have:

$$\frac{\partial p}{\partial y}=0\,. \tag{1.3.8}$$

Using these equations the Stokes equation 1.3.5 can be simplified to obtain:

$$\frac{\partial p}{\partial x}=\eta\left(\frac{\partial^2 u_x}{\partial x^2}+\frac{\partial^2 u_x}{\partial y^2}+\frac{\partial^2 u_x}{\partial z^2}\right)\,. \tag{1.3.9}$$

Since the flow speed is independent of x and y due to the infinite geometry, we are left with:

$$\frac{\partial p}{\partial x}=\eta\left(\frac{\partial^2 u_x}{\partial z^2}\right)\,. \tag{1.3.10}$$

By using non-slip boundary conditions at the walls, located at $z = \pm h/2$:

$$u\left(z = \pm\frac{h}{2}\right) = 0\,, \tag{1.3.11}$$

we obtain a solution for eq. (1.3.10):

$$u_x(z) = \frac{1}{2\eta}\frac{\partial p}{\partial x}\left(z^2 - \frac{h^2}{4}\right)\,. \tag{1.3.12}$$

This is the velocity profile along the z direction, which is clearly parabolic with the maximum occurring at mid-channel. By using eq. (1.2.5) it is possible to obtain the stress profile along the z direction as:

$$\sigma = \eta\frac{\mathrm{d}u}{\mathrm{d}z}\,. \tag{1.3.13}$$

In fig. 1.10 are reported the velocity distribution and the stress profile along the z direction.

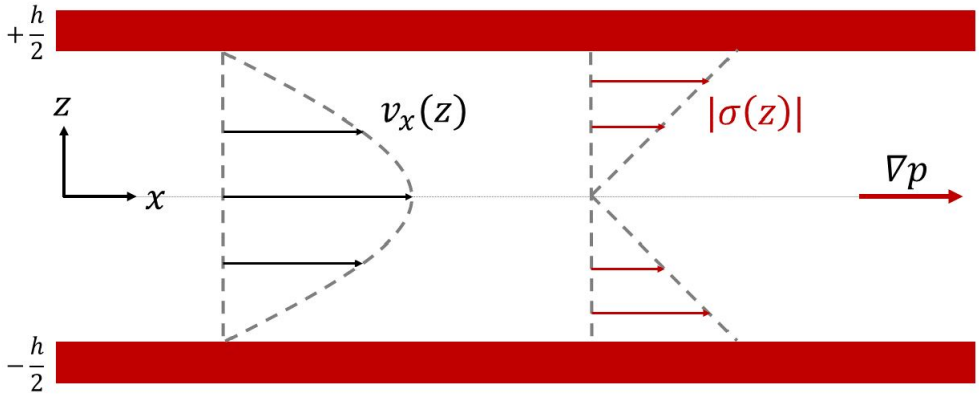

Figure 1.10: Schematic representation of the velocity distribution $v_x(z)$ and the modulus of the stress profile $|\sigma(z)|$ of a developed laminar flow of Newtonian fluid in a Hele-Shaw geometry. Figure reproduced from [32].

1.3.3 Yield stress fluid flow

In the case of a non-Newtonian fluids, we have to consider more complicated constitutive equations than eq. (1.2.5). We will focus our description on the important case of the Bingham plastic fluid. As we saw in section 1.2, the constitutive equation for this class of fluids are the eq. (1.2.22) and eq. (1.2.23) that we report here:

$$\dot{\gamma} = \frac{\mathrm{d}u_x}{\mathrm{d}z} = 0 \quad \text{for} \quad \sigma < \sigma_y$$

$$\dot{\gamma} = \frac{\mathrm{d}u_x}{\mathrm{d}z} = \frac{\sigma - \sigma_y}{\eta} \quad \text{for} \quad \sigma \geq \sigma_y\,,$$

where σ_y is the yield stress. In a Hele-Shaw geometry we have a non uniform stress along the channel, as represented in fig. 1.11. In the central zone of the channel we have that the stress is below the yield stress σ_y, thus inhibiting the flow of the fluid. Since in this

zone the shear rate is null, we have a flat velocity profile. It is possible to derive the size of the region in which we have the flat velocity profile [17]:

$$z_p = \left(\frac{\mathrm{d}p}{\mathrm{d}x}\right)^{-1} \sigma_y \tag{1.3.14}$$

We thus can express the shear rate as a function of the position in the channel. Due to the symmetry of the channel, it is sufficient to study the flow in the upper part of the channel, from $z = 0$ the the top plate at $z = h/2$. The lower part of the channel will show the same behaviour. The equations now reads:

$$\frac{\mathrm{d}u_x}{\mathrm{d}z} = 0 \quad \text{for} \quad 0 < z < z_p \,, \tag{1.3.15}$$

$$\frac{\mathrm{d}u_x}{\mathrm{d}z} = \frac{\mathrm{d}p}{\mathrm{d}x}\left(\frac{z - z_p}{\eta}\right) \quad \text{for} \quad z_p < z < +\frac{h}{2} \,. \tag{1.3.16}$$

Solving those differential equations leads to:

$$u_x(z) = C_1 = u_p \quad \text{for} \quad 0 < z < z_p \,, \tag{1.3.17}$$

$$u_x(z) = \frac{1}{\eta}\frac{\mathrm{d}p}{\mathrm{d}x}\left(\frac{z^2}{2} - z \cdot z_p\right) + C_2 \quad \text{for} \quad z_p < z < +\frac{h}{2} \,. \tag{1.3.18}$$

The integration constants C_1 and C_2 can be evaluated using the boundary conditions:

$$u_p = u_x(z = z_p) \,, \tag{1.3.19}$$

$$u_x(z = H/2) = 0 \,. \tag{1.3.20}$$

Finally, we obtain the velocity profile for a Bingham plastic in a Hele-Shaw geometry.

$$u_x(z) = u_p = \frac{1}{2\eta}\frac{\mathrm{d}p}{\mathrm{d}x}\left(z_p^2 - \frac{h^2}{4}\right) + \frac{\sigma_y}{\eta}\left(z_p - \frac{h}{2}\right) \quad \text{for} \quad 0 < z < z_p \,, \tag{1.3.21}$$

$$u_x(z) = \frac{1}{2\eta}\frac{\mathrm{d}p}{\mathrm{d}x}\left(z^2 - \frac{h^2}{4}\right) + \frac{\sigma_y}{\eta}\left(z - \frac{h}{2}\right) \quad \text{for} \quad z_p < z < +\frac{h}{2} \,. \tag{1.3.22}$$

We report, in fig. 1.11, a schematic representation of the behaviour of the Bingham plastic in the upper part of the channel. The *plug region*, where the velocity profile is flat, is the part between the center line at $z = 0$ and the line at $z = z_p$.

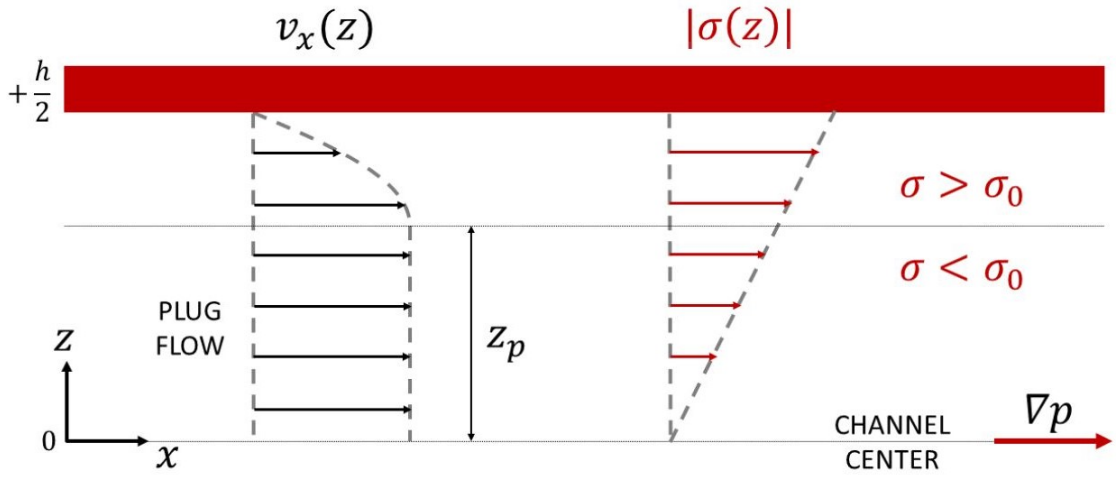

Figure 1.11: Schematic representation of the velocity distribution $v_x(z)$ and the stress profile $|\sigma(z)|$ of a developed laminar flow of a Bingham plastic fluid in a Hele-Shaw geometry. Only the upper part is represented. Figure reproduced from [32].

1.3.4 Power law fluid flow

In this section we will describe a derivation of an equation of motion for a fluid that obeys the power law model of eq. (1.2.13).
To derive an equation of motion for the fluid, we start by considering the forces acting on the faces of a small volume of a liquid in a pressure driven flow. Lets assume *body* forces like gravity are negligible. This is a sensible assumption in the context of the microfluidic channels [23]. In fig. 1.12 we can see a two-dimensional schematic representation of the model we are studying.

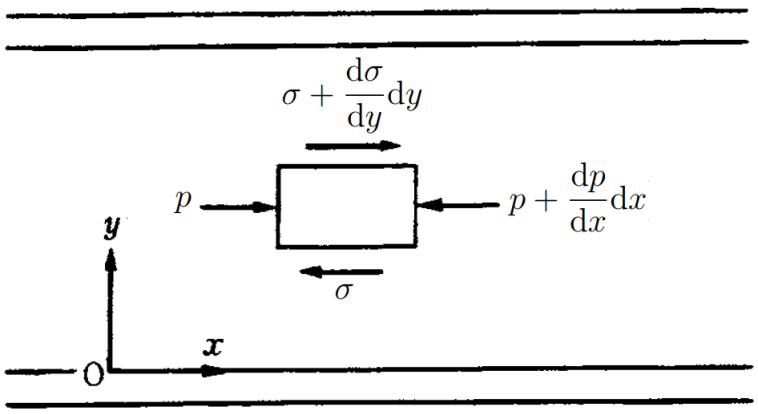

Figure 1.12: Schematic representation of the forces acting on a volume of fluid. Adapted from [31].

Assuming there is no change of momentum between the two faces, we obtains [31]:

$$p\mathrm{d}y - \big(p + \frac{\mathrm{d}p}{\mathrm{d}x}\mathrm{d}x\big)\mathrm{d}y - \sigma\mathrm{d}x + \big(\sigma + \frac{\mathrm{d}\sigma}{\mathrm{d}y}\mathrm{d}y\big)\mathrm{d}x = 0\,. \tag{1.3.23}$$

We therefore obtain:

$$\frac{\mathrm{d}\sigma}{\mathrm{d}y} = \frac{\mathrm{d}p}{\mathrm{d}x} \quad or \quad \partial_z\sigma(z) = -\nabla p\,, \tag{1.3.24}$$

where, in our geometry

$$\nabla p = \nabla_x p \equiv \frac{\partial p}{\partial x} \,. \tag{1.3.25}$$

Experimentally, we can impose the pressure gradient along x by controlling the pressure load applied to a channel of length L:

$$\nabla_x p = \frac{p(x_\mathrm{f}) - p(x_\mathrm{i})}{L} \,. \tag{1.3.26}$$

where in our convention $\nabla_x p$ is positive ($\nabla_x p > 0$). Let us consider a channel whose thickness ranges from $z = -h/2$ to $z = +h/2$, where h is the height of the channel, and let us call z_{MAX} the coordinate at which the velocity attains its maximum U_{MAX}. By integrating the differential equation eq. (1.3.24), using eq. (1.2.5), we get the following profile:

$$u(z) = -\left(\frac{n}{n+1}\right)\left(\frac{\nabla_x P}{A}\right)^{1/n} |z - z_{\mathrm{MAX}}|^{\frac{1+n}{n}} + U_{\mathrm{MAX}} \,. \tag{1.3.27}$$

We plot eq. (1.3.27) to highlight the role of each fitting parameter in the shape of the flow profile in fig. 1.13.

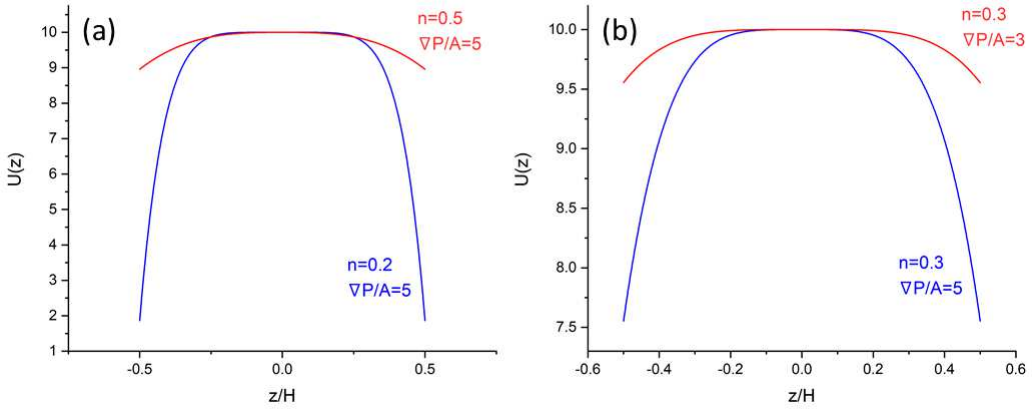

Figure 1.13: Plot of eq. (1.3.27) at various combinations of flow index n and $\nabla p/A$, reported in the figures: within each panel blue (red) text corresponds to blue (red) curves. At constant $\nabla p/A$ the increase of n accounts for the transition from plug to Poiseulle flow (a). Conversely at fixed thinning $n = 0.3$ an increase of $\nabla p/A$ steepens the side of the curve (c).

1.3.5 Slip velocity

In order to obtain the velocity profiles in section 1.3.2 and section 1.3.3 we imposed no-slip boundary conditions at the walls. This condition, illustrated in fig. 1.14(a), means that the velocity of the fluid decrease with the normal distance to the static wall until it reaches zero when in contact with the surface. This assumption has been experimentally observed especially in the case of Newtonian fluids in laminar flow [33, 34], but it cannot be derived from first principles [24]. The no-slip condition is generally assumed to be the result of viscous or frictional forces at the surface, that inhibit the motion of the particles in contact.

Conversely, it has been experimentally observed for a wide range of materials a slip velocity at the walls different from zero [42, 46, 62]. Even in the case of a non zero slip

velocity it is still useful to introduce a zero velocity boundary condition for the solution of the differential equations by introducing the concept of *slip length*, the extrapolation distance at which the fluid velocity relative to the walls vanishes. In the case of a *partial slip*, represented in fig. 1.14(c), the slip length b is always positive and the zero velocity point lies inside the solid, while if a *stagnant layer* is present (fig. 1.14(b)) this quantity could also be negative and the zero velocity point could lie inside the fluid. A stagnant layer could be explained by assuming the fluid-solid interaction is stronger than the interaction between the fluid particles themselves.

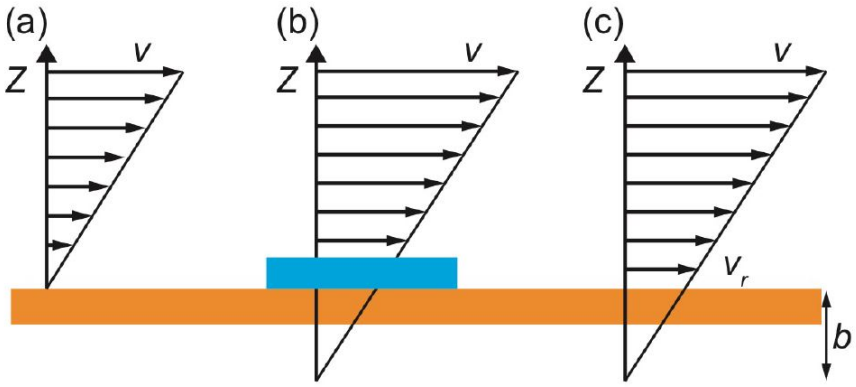

Figure 1.14: Schematic representations of the the no-slip (a), the stagnant layer (b) and the partial slip (c) boundary conditions. The slip length b is indicated for the stagnant layer and partial slip conditions. Figure reproduced from [17].

The wall slip condition is often described as the result of many factors that contributes to the fluid-surface interaction. Those are primarily the fluid properties such as viscosity, density and yield stress [6, 47, 57] as well as the physical and chemical properties of the surface, such as roughness and wettability [15, 16, 59]. Moreover, the flow regime, indicated by the Reynolds number, has been shown to affect the slip velocity [2, 14, 54]. Finally, the wall slip appears to be also dependent on the ambient conditions such as temperature and pressure [56].
The wall slip phenomenon affect also the non-Newtonian complex fluids [20], in fact, it appears to be more common than in Newtonian fluids systems [22]. This is due to the complex structure of non-Newtonian fluids, that introduce numerous factors contributing to the fluid-surface interaction that could promote the wall slip phenomenon. In the case of emulsions, for example, the wall slip can depend on parameters such as the concentration, size, shape a molecular weight of the particles of the dispersed phase. Experimental observations suggest that wall slip contribution to the flow rate if the fluid increases with increasing wall shear stress in shear-thickening fluids, while it decreases in the case of shear-thinning fluids [5]. The same behaviour has been observed for the yield-stress fluids. Those fluids bring another layer of complexity to the problem of wall slip, as there is normally an apparent yield at stresses lower than the bulk yield stress σ_y due to the wall slip velocity. Even if the local stress is below yield value, is possible for it to be above it in a very thin layer of fluid adjacent to the wall surface, which then acts as a lubricant film. This mechanism could hide the viscoplastic nature of the fluid due to the apparent flow. Another possibility, for multi-component fluids, is the formation of an inhomogeneous layer of continuum phase that serves the same purpose of lubricating film. This description leads to the model of *apparent slip*: the slip does not happen at the

fluid-surface interface, but instead at a fluid-fluid interface, as depicted in fig. 1.15(b). In these systems, the lubricating film is bound to the surface with no relative velocity, but the velocity gradient in the fluid next to the surface is so high that the particles in the adjacent layers appears to be sliding on the surface itself.

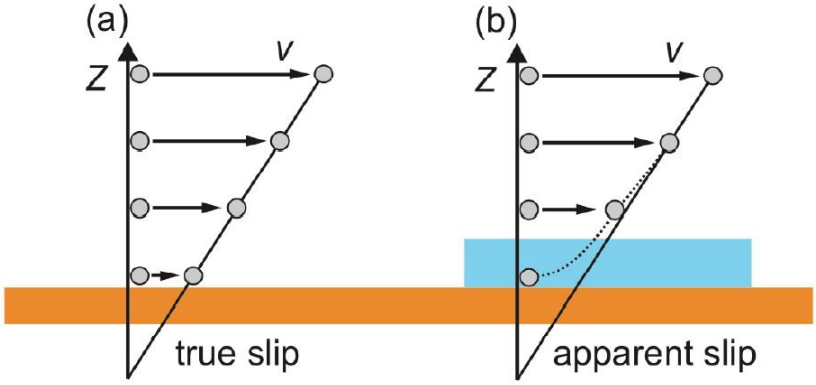

Figure 1.15: Schematic representation of true slip (a) and apparent slip (b). The light blue region indicates a thin layer of liquid with zero relative velocity with respect to the solid wall. Figure reproduced from [17].

In general we could distinguish three regimes of slip for yield stress fluids, depending on the value of the applied stress: at low stress ($\sigma \leq \sigma_y$) the flow is due to wall slip, slightly above σ_y both bulk flow and slip contributes to the fluid motion, and well above σ_y the slip is negligible and the flow is due to the bulk deformation.

1.4 Soft Glassy Materials

Soft materials are materials that are easily deformed by thermal stresses. In this category are included substances like liquids, foams, polymers, colloids, gels, granular materials, and soft biological materials. An interesting class of soft materials are the *Soft Glassy Materials* (SGMs). The important properties of this materials are a microscopically disordered structure and an extremely slow internal dynamics. The inner structure of those material make the SGMs show both liquid-like and solid-like behaviours. In section 1.2 we introduced the viscoplastic fluids: the SGMs are generally viscoplastic shear thinning materials, and are thus characterized by a yield stress. Materials that made up the SGMs category are gels, foams, pastes, concentrated emulsions and suspensions. In the description of the behaviour of the SGMs it is important to introduce the concept of *jamming*: a SGM is called *jammed* if the relaxation time for its inner structure is much greater than the observation time [36]. This condition means that the particles appear to be stuck in a stable configuration. This is the microscopic mechanism that originates the yield stress in the SGMs. Another important parameter, strictly related to the jamming notion, is the volume fraction ϕ of the inner constituents of the material. If the volume fraction is low, the particles have more mobility inside the fluid and the system is not globally jammed. While the volume fraction raises, it is more and more difficult for the particles to move avoiding their neighbours. At high ϕ, the particles are stuck, meaning the system is jammed and loses the ability to flow. It is now necessary a threshold stress to induce movement of the particles: the yield stress.

It is possible to define a critical volume fraction ϕ_{RCP}, which is defined as the random close packing condition for monodisperse, undeformed spheres [30]. This critical volume fraction, at zero temperature, is known as *jamming point* [38]. The yield stress have a dependency on ϕ, in fact it has a maximum for $\phi \sim 1$ and it decreases with ϕ towards the critical volume fraction ϕ_{RCP}. The yield stress have been shown to persist even for $\phi < \phi_{RCP}$ in many materials [29].

1.4.1 Emulsion

The concentrated emulsion is a SGM composed by a mixture of two or more liquids. The liquids that compose the emulsion are immiscible. In the case of two fluids, one is dispersed into the other, and we refer to it as the *dispersed phase*, while the other fluid is called *continuous phase*. An important class of emulsions, and the one discussed in this thesis, are the oil in water emulsion.
The process to prepare an emulsion is called *emulsification*: it consist of dispersing one fluid into the other via creation of an interface between them. This is an endothermic process, and the originated system is in a metastable equilibrium. The thermodynamic equilibrium is reached when the system is composed of two continuous separated phases [25].
To increase the stability of the system, so to avoid the phase-separation, it is possible to add to the mixture molecules called *surfactants*: those are *amphiphilic* molecules, meaning that they show both an hydrophilic and a lipophilic end, allowing to easily create bonds both with the continuous water phase and the dispersed oil phase. The introduction of surfactants lower the surface tension between the two fluids, thus easing the process of droplets creation. Moreover, the surfactants tends to completely cover the surface between the water and the oil, thus preventing the coalesce of the droplets and stabilizing the mixture. The introduction of surfactants in the oil in water emulsions could increase the lifetime of the metastable phase from a few days or less to years.

1.4.2 Emulsion rheology

The rheological behaviour of emulsions is highly dependent on the internal structure of the specific emulsion considered. In particular, it could depend on the composition of the emulsion, the size and distribution of the droplets, the interaction between the droplets and the interaction between the walls and the emulsion. Another important parameter that could influence the rheological behaviour is the volume fraction ϕ introduced in section 1.4. In fig. 1.16 is reported the evolution of the rheological properties of an emulsion as a function of the volume fraction ϕ.

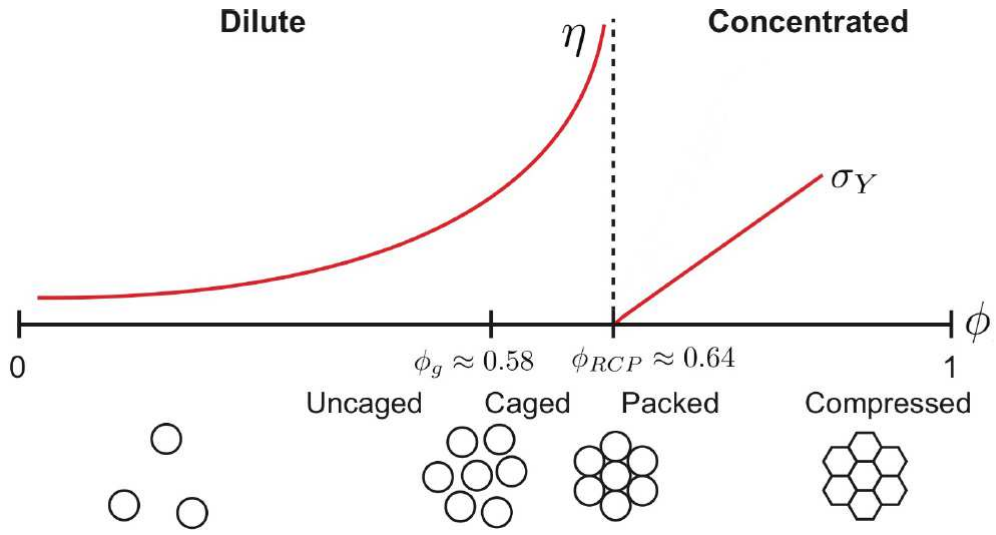

Figure 1.16: Scheme representing the emulsion rheological behaviour and the droplets configuration as a function of the volume fraction ϕ. In the left side of the picture, i.e. the the low volume fraction region, is represented the behaviour of the viscosity η, while in the right side, for volume fractions $\phi > \phi_{RCP}$, is represented the yield stress σ_Y behaviour. Image adapted from [17].

At low ϕ, in the *dilute* regime, in absence of shear the droplets are spherical. The low concentration allows the droplet to move freely in the dispersed phase. The emulsion behave like a Newtonian fluid with $\eta \sim$ const. At intermediate concentration the emulsion shows weak non-Newtonian behaviour. As we increase the volume fraction. we reach the value $\phi_g = 0.58$, the concentration value for the *hard sphere glass transition*. At this concentration the droplets becomes transiently caged by other droplets. At this concentrations, strong non-Newtonian effect may be present, and the system could have yield stress, thus becoming a viscoplastic.
If we increase again the volume fraction we reach the value $\phi_{RCP} = 0.64$ introduced in section 1.4. The droplets are now packed, and furhter increasing of ϕ leads to compression and deformation of the droplets. Above ϕ_{RCP} the emulsion has the rheology of a viscoplastic with a yield stress.
Many models have been proposed and experimentally tested over the years to explain this phenomenon [37, 41, 43]. The general assumption of those models is that whenever the volume fraction overcomes ϕ_{RCP} so that the droplets gets compressed and start to deform, energy is stored in the surface between the droplets. This deformation is reversible and elastic, and the energy is released if the droplet is set free and regain a spherical shape.
If the stress applied is high enough, above the yield stress, we can induce irreversible plastic rearrangements of the droplets, in which the configuration of neighbours changes as a result of the motion of the trapped droplets. This rearrangements release some of the energy stored by dissipating in the fluid flow. Thus this is a microscopic description that explain the existence of the yield stress and its relation with the liquid-like flow of the material.

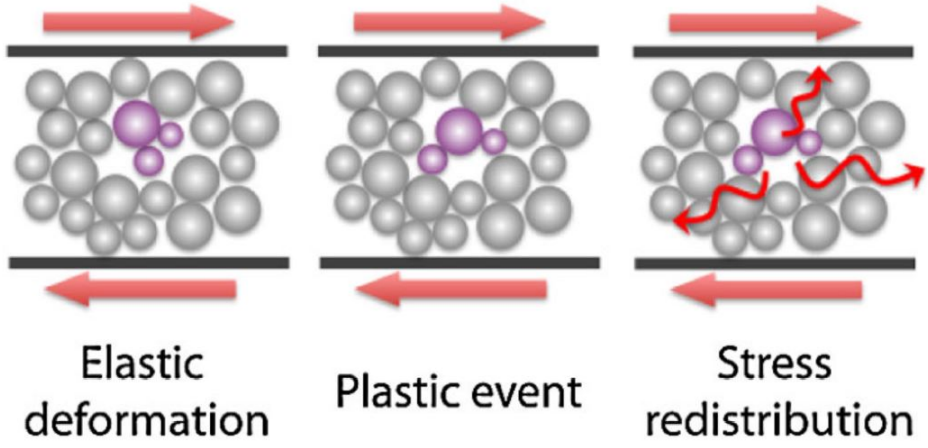

Figure 1.17: Scheme of the droplets stress accumulation and release through plastic rearrangements in an emulsion. Image reproduced from [10]

1.4.3 Emulsion flow

There has been an important research effort in the study of the flow of the emulsion, especially for high concentrations ($\phi > \phi_{RCP}$). A first comprehensive study was first published by Mason et al. [30] who found out that for emulsions with $\phi > \phi_{RCP}$ the yield stress had a dependence on the volume fraction described by:

$$\sigma_y \propto \left(\frac{\gamma}{a}\right)(\phi - \phi_{RCP})^2\,, \tag{1.4.1}$$

γ being in this case the surface tension and a the radius of the droplets. Moreover, they showed that the shear rate-stress relation for the concentrated emulsion is well described by a Herschel–Bulkley model (eq. (1.2.29)) with an exponent n which they found to be $n = 0.5$. Conversely, emulsions with volume fraction $\phi < \phi_{RCP}$ show a shear-thinning behaviour without a threshold stress value. Other works studied the flow of emulsions under confinement, finding numerous differences with the bulk flow of such materials. Goyon et al. [19] compared the flow of concentrated emulsion in two different confined geometries finding local shear rate-stress relations not reconcilable with the single master curve of the non confined system (see fig. 1.18): for a given applied shear stress we could have different shear rates for different conditions.
This is called a *non-local* behaviour, in which the flow of the system cannot be described by a *local* relation, but finite size effects must be considered. This non-locality has been confirmed to be connected to the plastic rearrangements of the material constituents introduced in section 1.4.2 [18, 48]. The flow of the fluid is related to these long range interactions, hence it cannot be described by a single local relation between shear rate and applied shear stress.

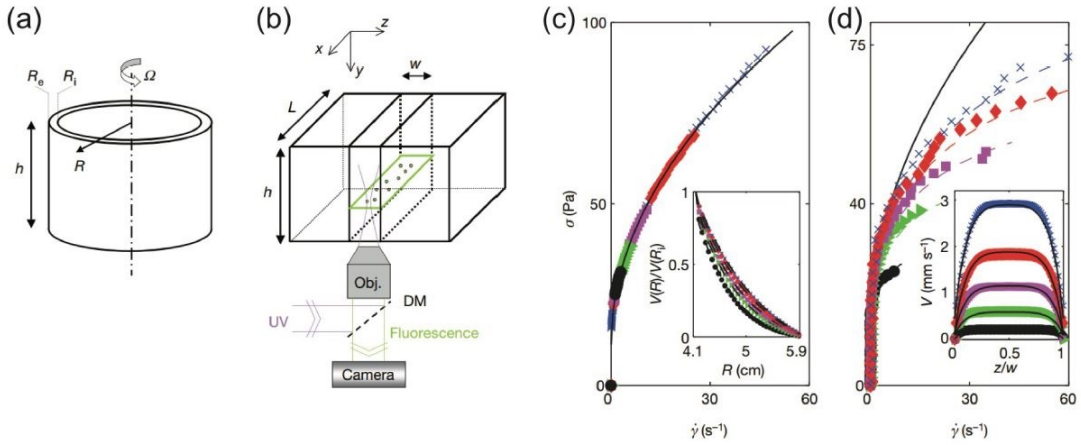

Figure 1.18: Schematic representation of a wide gap Couette cell (a) and a microfluidic channel (b). The shear rate-stress relations obtained for the two geometries are reported respectively in (c) and (d). For the microfluidic channels, we have different curves for different velocities given by different pressure drops. Data reproduced from [19]

Bocquet et al. used this phenomenology to construct a theoretical framework that accounts for the non-local effects: the Kinetic Elasto-Plastic (KEP) model [10].
The model describes the non local effects using a diffusion-relaxation relation for the *fluidity* $f = 1/\eta = \dot{\gamma}/\sigma$ in which arises a *cooperativity length* ξ, a characteristic length scale which represent the spatial extension of the correlations due to the finite size effect of the plastic rearrangements that give rise to the non-local behaviour. Physically, ξ measures the spatial spreading of the plastic rearrangements. It is found that the ξ is only a function of the volume fraction ϕ [16, 19]. The models also suggest that the *rate of plastic rearrangements* Γ is proportional to the fluidity, i.e. $\Gamma \propto f$.
The discovery that these non-local behaviour affect on the fluid flow in a confined geometry raises interest in the study of the microscopic interaction of the emulsion with the walls, and how it can trigger the plastic rearrangements. This interaction was studied in a limited number of papers, such as [16], [15], [27] and [40]. Mansard, Bocquet et al. studied the flow of concentrated emulsions in microfluidic channels with pillars decorated walls [27]. By varying the pillars height, they observed that the wall fluidization was in fact a non monotonous function of the pillars height. This was explained by an 'activation' of the plastic rearrangements caused by the wall roughness (the pillars). Moreover, Paredes et al. [40] showed that the wetting properties of the walls affects the local fluidization of the emulsion. They observed that droplets could be adsorbed by the walls that acts as 'soft' roughness, inducing plastic rearrangements in the fluid.
Other works [15, 16] have studied the effect of wall roughness on the flow of concentrated emulsion in microfluidic channels by using grooves patterned channels that varies in the shapes of the grooves, the gap g between the grooves and the grooves width w. In [16] they studied the difference in the flow against a smooth wall and a grooved one, finding that the rate of plastic rearrangements is enhanced by the grooves. If the surface of the wall is patterned in a periodic fashion with the grooves, it is found that the fluidization is a power-law scaling function of the roughness periodicity. A low periodicity, i.e. a bigger $\lambda = g + w$, results in less rearrangements and a less fluid-like behaviour of the emulsion. In [15] they found that the emulsion behaviour changes depending on the relative size of the grooves with respect to the droplet size. If the gap g between the grooves is suffi-

ciently large ($g \gtrsim 3$ droplet diameters) the emulsion flow is enhanced by the roughness by the interaction with the wall, but if the the gap is narrow ($g \lesssim 3$ droplet diameters) droplets might get trapped in the gaps, thus behaving in a similar fashion to an adsorbed droplet, i.e. a 'soft' roughness. The two situations are reported in fig. 1.19

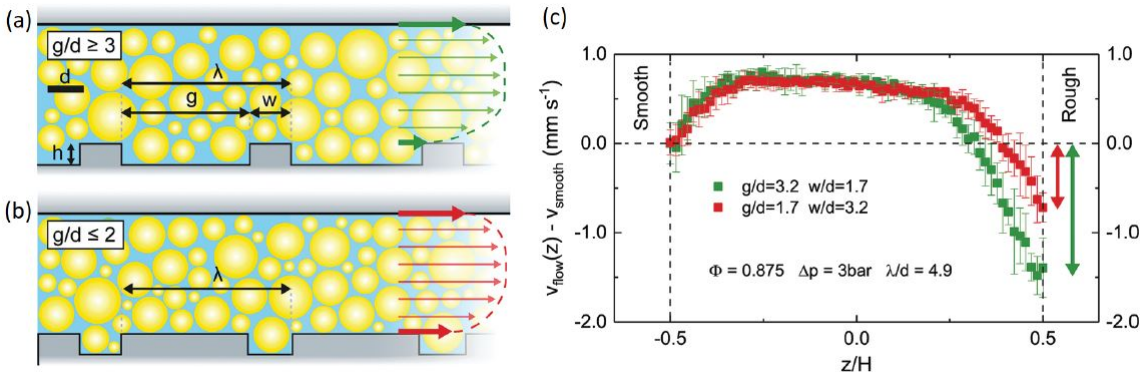

Figure 1.19: Scheme representing the wall roughness effect on concentrated emulsion flow. In (a) is represented the large gap grooves channel, while in (b) the narrow gap one. In (c) are reported the velocity profiles for these two behaviours. Figure reproduced from [15].

1.4.4 Emulsion flow in herringbone decorated microfluidic channels

A particular geometry for the grooves patterned walls inside a microfluidic channels is the *herringbones* one. An example of such geometry is represented in fig. 1.20.

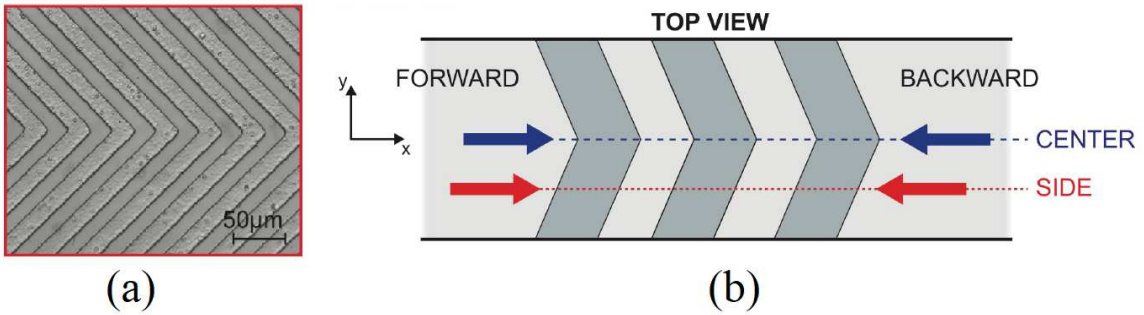

Figure 1.20: Herringbone geometry. In (a) is reported a picture of the actual device used in [17], while in (b) is represented the nomenclature for this geometry. Figure adapted from [17].

This kind of grooves introduce a symmetry breaking for the flow direction, meaning that the roughness encountered by the fluid is different if the channel is crossed in a direction or in the opposite one. In fig. 1.20 (b) is represented the nomenclature used to describe the channel, in particular, the *forward* direction, following the points of the grooves, and its opposite *backward* direction. The difference between the forward plug velocity and the backward one is called *plug velocity difference* Δv_{plug}. Moreover, in fig. 1.20 are represented the *center* of the channel, in correspondence of the points of the grooves, and the *side* position, located at mid distance between the center and the lateral

walls.
In [17], they found a Δv_{plug} different from zero at the center of the channel for concentrated emulsion ($\phi = 0.85$). This difference is greatly reduced at the side position, approximately 1 mm away from the center. Those results are confirmed for emulsions at $\phi = 0.875$ and $\phi = 0.75$ [32]. These works also showed that the Δv_{plug} is a monotonous function of the pressure drop imposed to the flow [32].

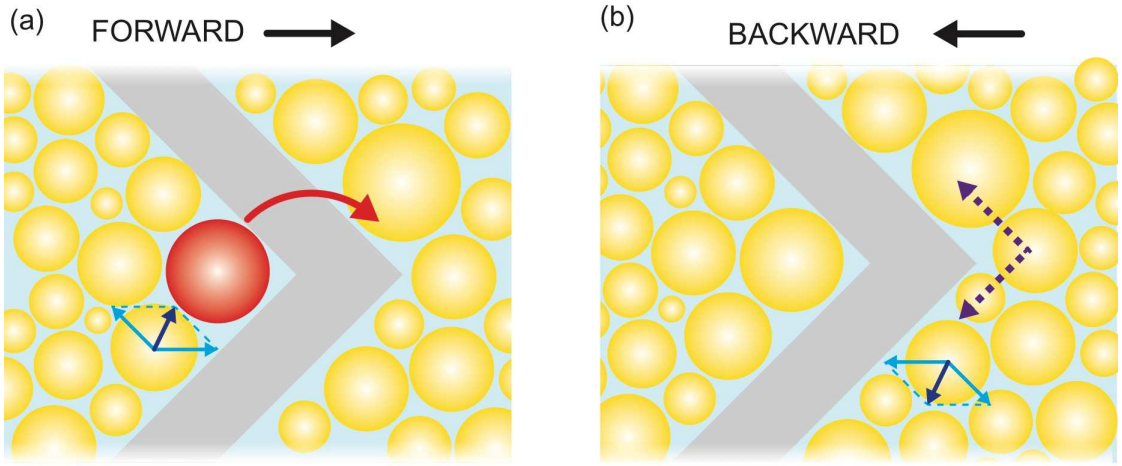

Figure 1.21: Schematic representation of the flow of concentrated emulsion across the roughness of a herringbone grooves decorated channel. (a) Oil droplets flowing at the center of the channel in the forward direction. (b) Droplets flowing in the backward direction. Figure taken from [17].

A justification for these results was given in terms of a different mechanical behavior of the emulsion flow moving in the two directions. While moving in the forward direction (fig. 1.21 (a)), a droplet near the patterned wall can get caught in the gap, and can either jump over it or slide along the grooves. The combination of the normal force of the roughness with the force caused by the pressure drop induce a motion toward the center of the grooves, where it has no other possibility than to jump over the groove. Since this jumps can trigger plastic rearrangements, this explain the enhanced fluidization of the emulsion in the center of the channel for the forward flow. Conversely, in the backward direction (fig. 1.21 (b)), the droplets slides to the side toward the lateral walls, preventing an accumulation of droplets in the center. There is thus no enhancement of fluidization because there is no mechanism to increase the rate of plastic rearrangements.
The same model was used to explain the reduced Δv_{plug} at the side position.

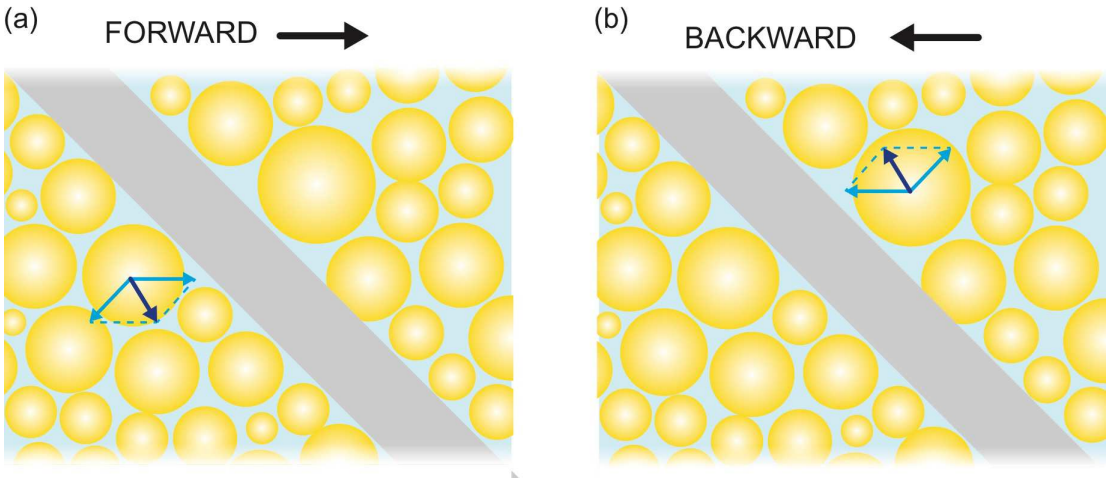

Figure 1.22: Schematic representation of the flow of concentrated emulsion near to the roughness of a herringbone grooves decorated channel. (a) Oil droplets flowing at the side position of the channel in the forward direction. (b) Droplets flowing in the backward direction. Figure taken from [17].

In fig. 1.22 we could see that at the side position the difference between forward and backward flow is less pronounced. Far enough from the center of the grooves and from the lateral walls, the geometry seen from the droplets is that of a tilted groove, symmetric in the two directions. There is thus the same enhancement of the plastic rearrangements rate and consequently of the fluidization of the emulsion.
In [61] it was found that Δv_{plug} is also a non monotonous function of the emulsion volume fraction ϕ [61]. It has to be noted that a Δv_{plug} different from zero exist also for volume fractions $\phi < \phi_{RCP}$ [61]. In fact, the biggest Δv_{plug} is found for an emulsion with $\phi = 0.6$, suggesting that the value ϕ_{RCP} might not be in fact the limit for the non-Newtonian behaviour.
The results presented in this section raise interest in studying how the Δv_{plug} behave along the channel, as the only available data points are an apparent maximum at the center of the channel and an apparent minimum and the side position. This can be done by means of a 3D mapping of the flow inside the channel.
The study of the 3D flow of fluids inside herringbones decorated microfluidic channels in literature is strictly related to the problem of the laminar mixing: in a microfluidic channel the flow is laminar for a great range of flow velocities, it is thus very difficult to have an efficient mixing of fluids in such channels, as the only mixing mechanism is the molecular diffusion. In a remarkable paper, Stroock et al. [53] found that *alternate staggered herringbones* geometry drastically increased the mixing of two fluids flowing inside the channel by inducing complex flow patterns that greatly enhanced the molecular diffusion between the two fluids. A representation of a staggered herringbone channel and the flow pattern generated is reported in fig. 1.23. Other works [28] found enhanced mixing also in the case of a symmetric herringbones pattern.

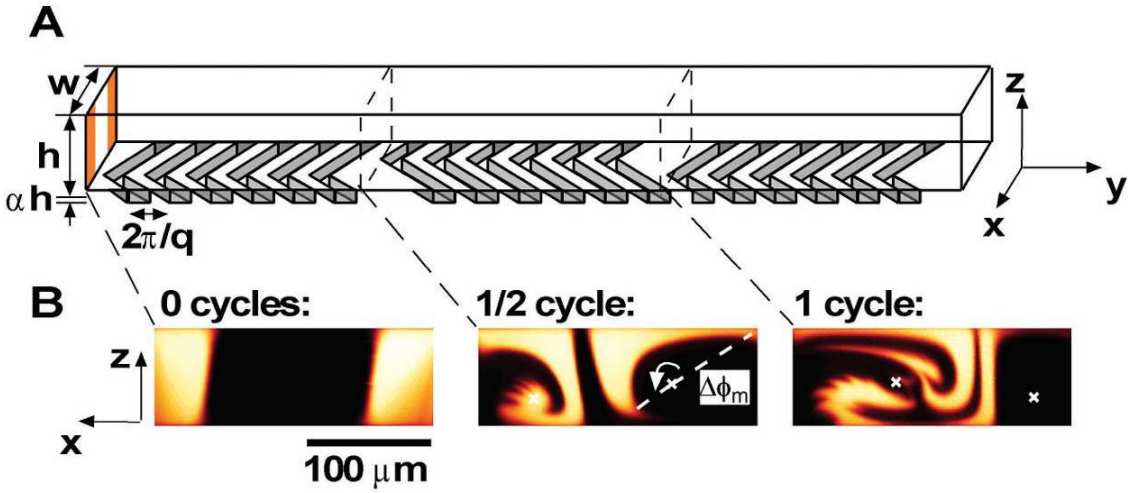

Figure 1.23: (A) Schematic diagram of the staggered herringbones mixer. A mixing cycle is composed of two consequential regions of grooves. (B) Vertical cross sections of the channel. Figure taken from [53].

These works, while highlighting how a patterned surface can induce complex motions in a fluid, does not focus on the difference of the flow in the two directions inside the channel and on the microscopical mechanisms responsible for resulting differences. The purpose of this Thesis is to study the 3D flow of emulsion inside a herringbone decorated channel in the forward and backward direction. Since the maximum Δv_{plug} was found for $\phi = 0.6$ in [61], this is the chosen concentration for this work.

Chapter 2

Materials and methods

In this chapter we will introduce the preparation and characterization of the fluids used in the experiment, as well the apparatus and the procedures that were employed to collect data.
In section 2.1 we will describe the experimental setup and procedure for the rheological characterization of the fluids. We will then proceed to describe the fluids utilized in this thesis: in section 2.2 we will describe the emulsion, its preparation and its characterization, while in section 2.3.1 we will describe those of the Xanthan gum solution. In section 2.4 we will describe in detail the microfluidic channels and their geometry. In section 2.5 we will describe the experimental setup for the flow profiles data collection while in section 2.6 we will describe the protocol for the measure.
Finally, in section 2.7 will be shown the data post-processing and analysis to obtain the flow profiles of the fluid in the channel.

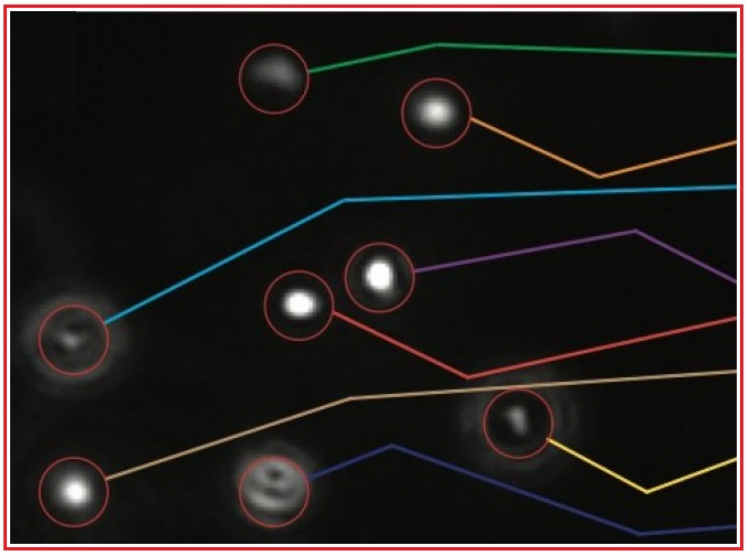

2.1 Rheological measure

To obtain the rheology of the fluids studied, we employed a cone-plate rheometer (ARES 4400, TA Instruments). This rheometer uses a cone that turns under a torque Γ at angular velocity ω with respect to a static plate. The angle α the cone makes with the static plane is $\alpha = 0.04$ radiant. The cone is mantained at a fixed distance from the static plane: the gap $g(r)$ between the two surfaces is thus a function of the distance r from the tip of the cone: $g(r) = \tan(\alpha) \cdot r$. The shear rate $\dot{\gamma}$ in this geometry is given by:

$$\dot{\gamma} = \frac{\omega r}{g(r)} = \frac{\omega}{\tan(\alpha)}\,, \tag{2.1.1}$$

while the stress σ is instead given by:

$$\sigma = \frac{3\Gamma}{2\pi R_0^3}\,, \tag{2.1.2}$$

with R_0 being the radius of the cone of the rhoemeter. A scheme of the device is reported in fig. 2.1.

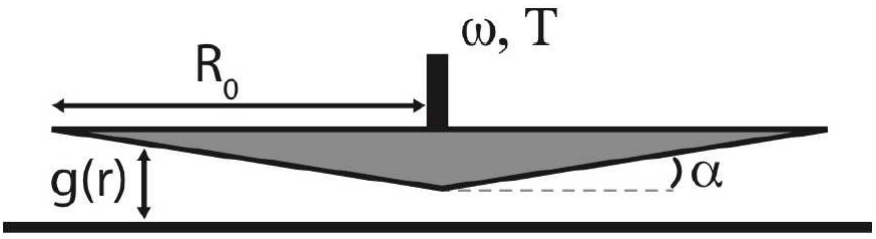

Figure 2.1: Scheme of the cone-plate rheometer. Image taken from [17].

The rhometer used was a *stress controlled* type one. In this devices the torque Γ is imposed while the the angular velocity and thus the shear rate $\dot{\gamma}$ is measured.

2.2 Emulsion

The emulsion used in this thesis is an oil in water emulsion produced at LAFSI lab. The dispersed phase is composed of silicone oil (Rhodosil 47 v 1000, Bluestar Silicones, France), while the continuous phase is a mixture composed by:

- Distilled water
- Glycerol (Sigma-Aldritch, Germany)
- Tetradecyltrimethyl-ammonium bromide $C_{17}H_{38}N^+Br^+$, also known as *TTAB*
- FluoSpheres®, carboxylate modified microspheres, size $d \sim 0.2\,\mu$m (ThermoFisher, USA)

The process of emulsification is widely covered in literature [3, 21, 50]. For the batch used, the preparation starts with mixing the distilled water and the glycerol to obtain the continuous liquid phase. In order to obtain an optically homogeneous emulsion, the glycerol-water ratio in the continuous phase was chosen to match the refractive index of

the silicone oil. The match was obtained with a 54% (w/w). The TTAB was then added to the mixture at 1% (w/w) as a surfactant. This helps keeping the silicone droplets disperded. Lastly the continuous phase is completed by the addition of the fluorescent nanoparticles (0.002% (w/w)) to be used as tracers during the experiment. At this point the process of emulsification starts with the addition of the silicone oil at a slow pace ($\sim 1\,\mathrm{ml/min}$) to create the droplets. The addition continues until the volume fraction of oil with respect to the total mixture is about $\phi = 0.93$.
This emulsion is unstable to coalescing of the droplets, so the next step is to dilute it with the same continuous phase to a volume fraction of $\phi = 0.875$. A visual example of the emulsion at this stage in reported in fig. 2.2. In this form the emulsion is then stored in centrifuge tubes of 50 ml.
In order to be used in the experiments, the emulsion was diluted to reach the desired volume fraction required. This last step requires the emulsion to be centrifuged to remove the air bubbles that forms during mixing and that could interfere with the measures.

Figure 2.2: Emulsion at $\phi = 0.875$. Picture taken from [32].

2.2.1 Emulsion characterization

One of the properties that characterize an emulsion is the droplet size and size distribution. The characterization work on the batch of emulsion used in this thesis has been done in [17], [32] and it is reported here for completeness.
The procedure consists in taking images under bright field optical microscope using a 100x magnification lens, then the software NIS Elements was used to determine the dimension of the droplets. An example of a microscope image and the analysed counterpart is reported in fig. 2.3.

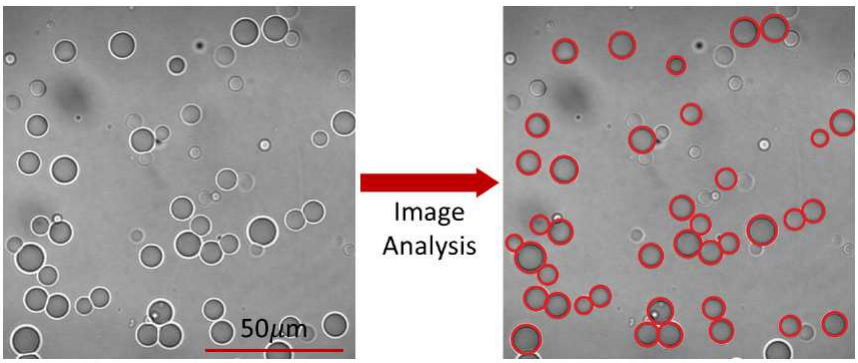

Figure 2.3: Image of a dilute emulsion. The red circles are the particles detected during the size distribution analysis. Picture adapted from [17].

The two parameters measured were the *mean droplet diameter* $\langle d \rangle$ and the *polydispersity index*, which is the coefficient of the variance of droplet size distribution: $C.V. = \sigma/d$ x 100%. The results obtained were $\langle d \rangle = 8.9\,\mu$m and $C.V. = 51\%$. The emulsion was also tested for stability of the droplets in [17], in a two months span, no significant difference was observed in the droplets size and size distribution.

2.2.2 Emulsion rheology characterization

We have taken a rheological characterization of the emulsion at concentration $\phi = 0.6$, the one used in this thesis. The $\eta - \dot{\gamma}$ behaviour is represented in fig. 2.4.

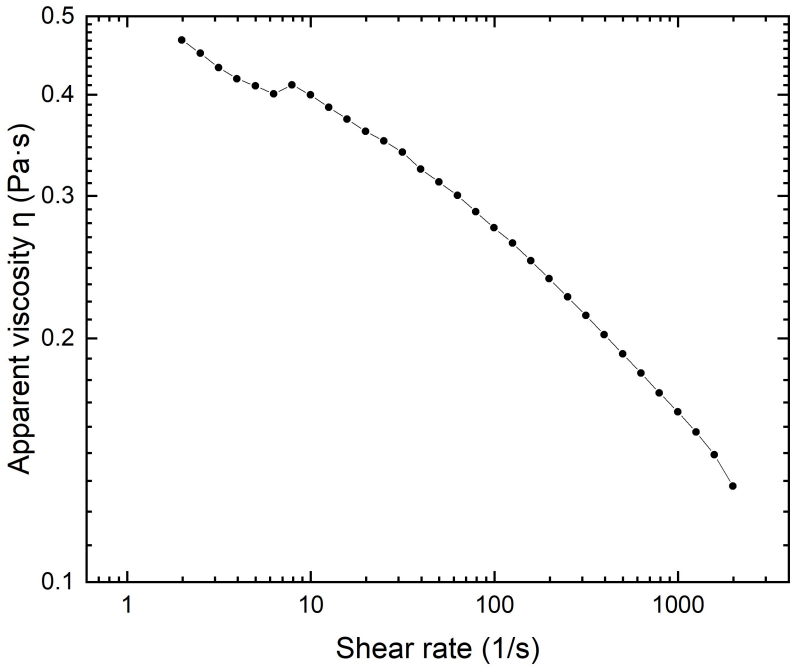

Figure 2.4: Viscosity characterization for the emulsion at concentration $\phi = 0.6$.

The emulsion clearly show a power law region described by (eq. (1.2.13)). The fitting parameters are $n = 0.849 \pm 0.006$ and $A = 0.53 \pm 0.01$. Since we have $n < 1$, the emulsion is a *shear thinning* fluid.

2.3 Polymer solutions

Polymer solutions typically shows non-Newtonian behaviors that depends on the mechanical and elastic properties of the polymeric chains and on the polymer concentration. A polymeric solution can be visualized as random coiled chains that occupy a spherical region, as shown in fig. 2.5. Depending on the concentration of the solution, it is possible to distinguish three possible regimes: *dilute*, *semidilute* and *concentrated*.

- **Diluted solution**: The polymer chains are well separated and behave almost independently, the interactions are mainly with the solvent molecules;
- **Semidilute solution**: The spheres that contains the polymer chains are packed. The chains are now entangled and their mobility is greatly reduced with respect to the chains in the dilute regime.
- **Concentrated solution**: In this regime the polymer chains are completely overlapped and entangled. The chains collectively forms an intricate network.

For a high molecular weight polymer (from $M_w \sim 10^5\,\mathrm{g\,mol^{-1}}$) a broad range of concentrations fall in the semidilute regime, with different degrees of overlapping.

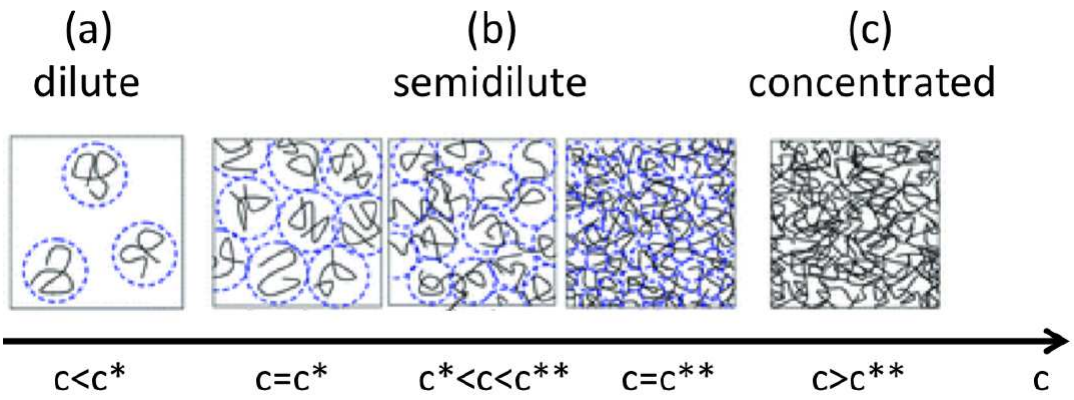

Figure 2.5: Concentration regimes for polymer solutions. The values c^* and $c^*\!*$, delimiting respectively the dilute and semidilute phase, are also reported. Picture reproduced from [58].

An important parameter to characterize the polymer solution is the overlapping concentration c^*. This is the concentration value at which the spheres containing the polymer chains touch each other, occupying the volume in a packed arrangement, and is the transition value from the dilute to the semidilute regime. The expression for c^* is given by:

$$c^* = \frac{1}{\frac{4\pi}{3}R_g^3}\frac{M_w}{N_A}\,. \tag{2.3.1}$$

In the expression N_A is the Avogadro's number, M_w/N_A the mass of each chain and R_g is the gyration radius of the polymer chain, that gives the radius of the sphere. The transition from semidilute to the concentrated regime is given by the concentration value c^{**} for which the volume fraction occupied by the polymer exceeds the values $0.2 - 0.3$.

2.3.1 Xanthan

The Xanthan gum is a polysaccharide with many industrial uses, including as a common food additive. It is a siff rod-like polymer, and when diluted in distilled water, the resulting polymeric aqueous solution is mainly characterized by its shear-thinning viscosity. In many works, its normal stresses were claimed to be negligible when compared to the shear rate dependence of the viscosity [44, 58].

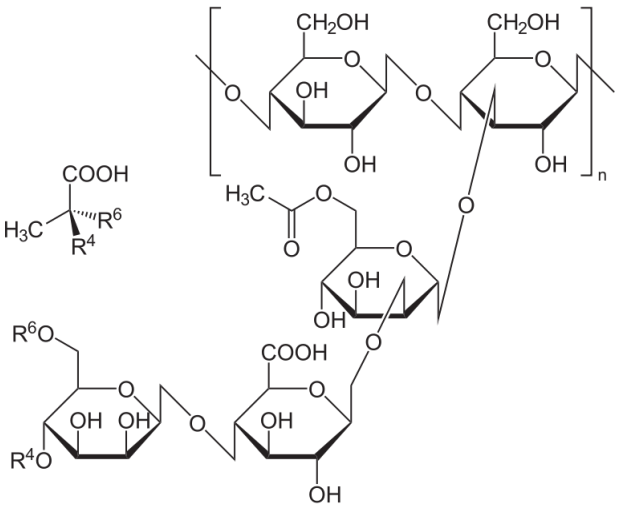

Figure 2.6: Xanthan structure.

The Xanthan/water solution used has been prepared using Xanthan gum provided by Sigma Aldrich (molecular weight, $M_w \sim 10^6\,\mathrm{g\,mol^{-1}}$). The distilled water is provided by a Milli-Q® (Merck Millipore) device and then refiltered using a $0.2\,\mu$m syringe filter (Whatman®, Cytiva).
We prepared solutions at 5000 ppm and 2500 ppm at room temperature, and mixed using a magnetic mixer and a stir bar for 24 hours. Those solution is in the *semidilute* regime, with a concentration of the order $c \simeq 10^2 c^*$ Before the experiment, dye tracers (FluoSpheres®, carboxylate modified microspheres, size $d \sim\ 0.2\,\mu$m (ThermoFisher, USA)) are added to the solution at a concentration of 0.002% (w/w), to be used as tracers during the experiment.

2.3.2 Xanthan rheology characterization

Here we present the rheological data for the Xanthan solutions used in this thesis. We have taken the $\eta - \dot{\gamma}$ behaviour for the 5000 ppm and the 2500 ppm. A comprehensive study for lower concentrations can be found in [60].

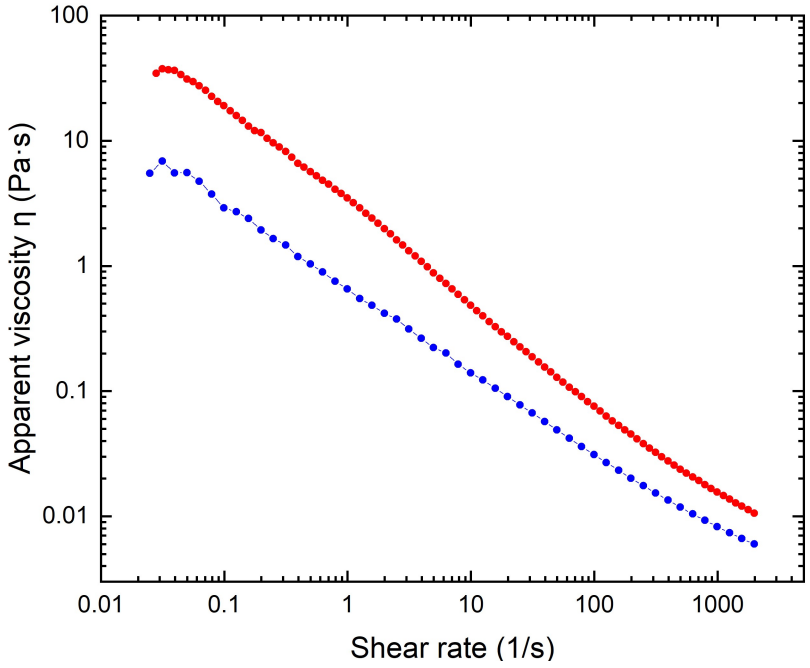

Figure 2.7: Viscosity characterization for Xanthan solutions at 5000 ppm (red curve) and 2500 ppm (blue curve) concentration.

Both concentrations show the power-law region described by the n and A parameters in eq. (1.2.13) and the Newtonian plateau for low shear rates η_0 of eq. (1.2.16), eq. (1.2.20) and eq. (1.2.21). Those parameters are reported in table 2.1.

Xanthan/water solution			
Concentration ppm w/w	n	$A\ (Pa \cdot s^{n-1})$	$\eta_0\ (Pa \cdot s)$
5000	0.17 ± 0.01	3.48 ± 0.01	37.5 ± 1.5
2500	0.35 ± 0.01	0.65 ± 0.01	5.9 ± 0.8

Table 2.1: Viscosity parameters for the Xanthan solutions

The n parameter for both concentration is less than the one found for the emulsion in section 2.2.2, this means that the decrease of the apparent viscosity η with the increase of the shear rate $\dot{\gamma}$ is more pronounced in the Xanthan solution than in the emulsion.

2.4 Microfluidic channels

Following previous works on the complex fluids behaviour in microfluidic channels at LAFSI lab [17,32] we used a herringbone grooves decorated channel for the experiments which is 4 mm wide (y direction), $L = 4.5$ cm long (x direction) and $H = 120\,\mu$m of height (z direction). The bottom wall is the one decorated with the herringbone pattern of grooves, which have the points at the center of the channel along the y direction, which is defined as the origin $y = 0$. The grooves height is $h = 2.5\,\mu$m. A schematic representation of the channel section is represented in fig. 2.8, showing also the flow direction, defined as *forward* ("fwd") if the flow direction is in the converging grooves direction, and *backward* ("bwd") if it is in the diverging one.

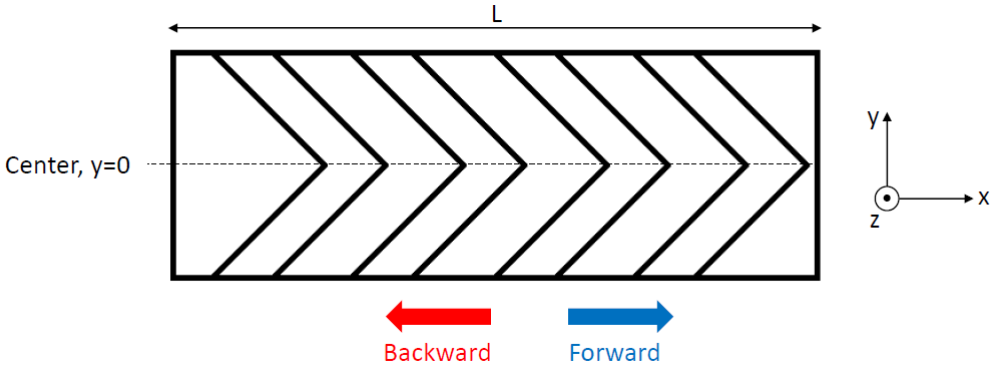

Figure 2.8: Schematic representation of the channel and principal nomenclature.

Patterned surface The grooves patterned surface is manufactured by multilayer UV photolithography using a mask aligner at the Institute of Physical Chemistry of the Polish Academy of Science (Warsaw, Poland) by the group of Prof. Piotr Garstecki. The fabrication quality has been studied at the IPC using an optical profilometer (SENSOFAR S neox, Spain). The grooves are well structured [17], with sharp edges and a mean surfac roughness of 150 nm, which is negligible compared to the height h of the grooves.

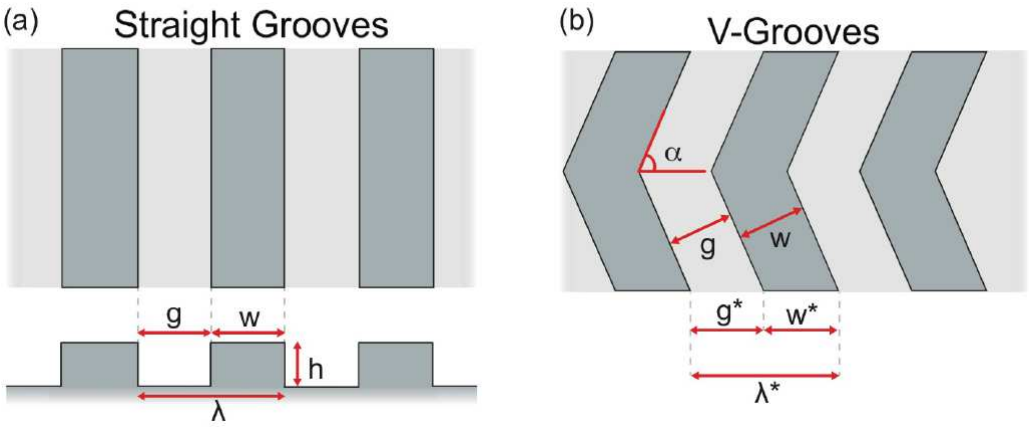

Figure 2.9: Characteristic dimensions of (a) straight and (b) V-shaped grooves. Image taken from [17].

Other parameters that characterize the grooves are the grooves width w, the spacing gap g and the grooves period $\lambda = g + w$. For the herringbone pattern, also called *V-Grooves*, we also have the angle between the groove and the channel longitudinal axis α and the projection of g and w on the longitudinal axis: $g^* = g/\text{sen}(\alpha)$ and $w^* = w/\text{sen}(\alpha)$.

Channel assembly The channel is then assembled using as top walls a microscope slide that has been drilled to apply the tubes for the flow of the liquids. To close the channel, a dry film photoresist (WBR-2000, DuPont, USA) of fixed height of 120 μm is used. The dry photoresist act both as a glue to close the channel and as side walls of fixed height. The dry photoresist is cut to channel shape using a knife plotter (Craft Robo CC200-20, Graphtec, Japan). The dry photoresist mask obtained in this way is applied to the patterned surface, and the drilled microscope slide is put on top of the mask, sealing the channel. The channel is then put under hydraulic press at a pressure of 2 bar

for 5 minutes at 80 °C, to ensure optimal surface adhesion. The channel is completed by exposing it to UV light (i-line 365 nm) for 60 seconds, polymerizing the photoresist. This harden the film between the two plates, giving a robust and stable final device.
After the assembly, the channel is coated with a non-ionic hydrophilic coating by activating the surfaces using a oxygen plasma and then fluxing a water/PVP (Polyvinylpyrrolidone K90, AppliChem) solution (2.5% w/w) into the channel for 2 hours at a flow rate of about 3 ml/h using a syringe pump. This procedure is particularly effective in preventing the coalescence of the emulsion at the walls when it flows inside the channel [17].

2.5 Experimental setup

To measure the flow profiles in the channels we employed the micro-particle tracking velocimetry (μPTV) technique. The μPTV procedure distinguish itself from other tracking techniques such as the Particle Image Velocimetry (PIV) in the fact that it obtain information about the fluid motion by the direct identification of particles in the fluid and determination of their position in space. To this aim, the apparatus shown in fig. 2.10 has been used.

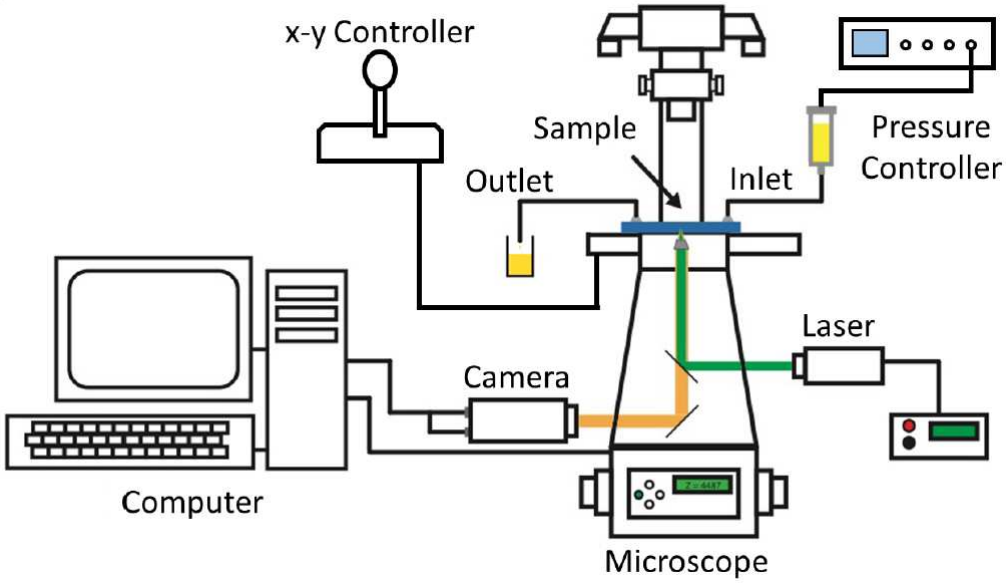

Figure 2.10: Schematic draw of the experimental set-up. Image adapted from [32].

The flow of the fluid in the channel is induced by a pressure drop applied of the reservoir by a microfluidic pressure controller (MFCS^{TM}-EZ, FLUIGENT, France), with an accuracy of 1% on the scale of a few hundreds of mbar. The reservoir is then connected via teflon tubes to the channel inlet, while the outlet is connected to another reservoir. The data acquisition exploits the fluorescent tracers in the fluid, that are stained with Rhodamine B, which is fluorescent with $\lambda_{exitation} \sim 540\,\text{nm}$ and $\lambda_{emission} \sim 560\,\text{nm}$. The tracers are irradiated in a epifluorescence microscopy configuration using a Laser illumination (Reutner, DPSS, $P_{max} = 100\,\text{mW}$, $\lambda = 532\,\text{nm}$ Austria) and an optical inverted microscope (Eclipse Ti-E, Nikon, Japan). The epifluorescence configuration uses a dichroic mirror (TRITC band-pass ($570 - 620\,\text{nm}$, emission filter) that allows for the Laser to illuminate the sample, while it cuts the light reflected by the sample and

leaves only the emission light to reach the camera. In fig. 2.11 we see the exitation and emission spectra, along with the laser wavelength and the filter bandwidth.

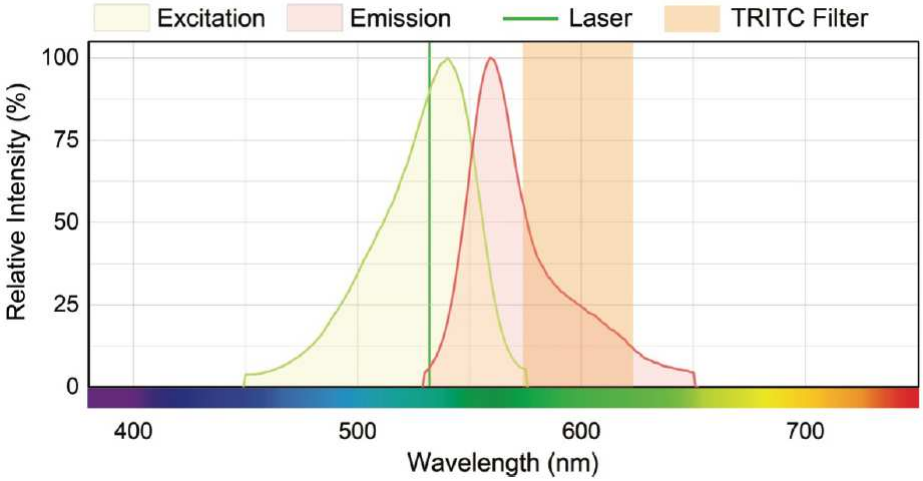

Figure 2.11: Fluorescence excitation and emission spectra of FluoSpheres®. The red line indicate the wavelength of the laser beam utilized. The orange band represent the TRITC filter pass-band. Image taken from [17].

For the experiment we used a 60x magnification, aphocromatic corrected, long working distance (WD = 2 mm) with numerical aperture NA = 0.7 (SuperPlan Fluo, Nikon, Japan). The motorized microscope allows for the regulation of its vertical position (z direction) with a step resolution 0.025 μm. To collect images we selected a Region Of Interest (ROI) of 320 x 64 pixels, corresponding to region of 35 x 7 μm. A visual example of a ROI is reported in fig. 2.12.

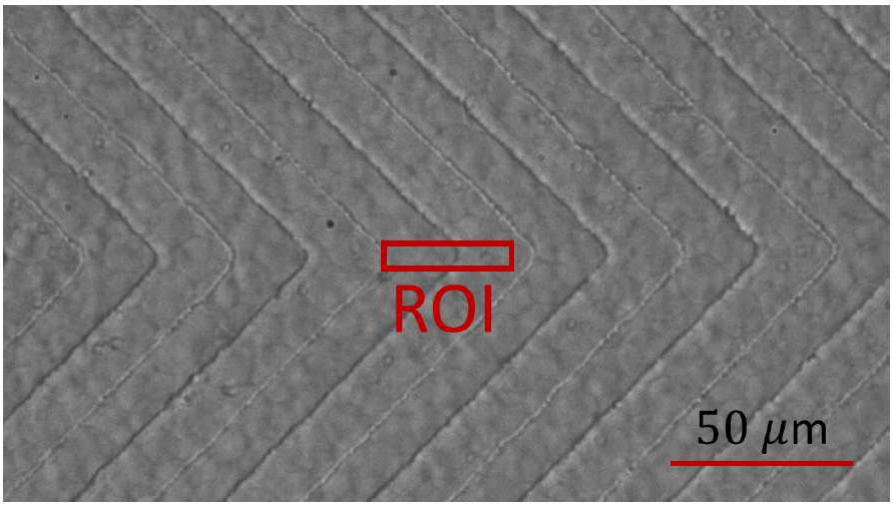

Figure 2.12: An example of the ROI in the center of a V-Grooves channel with ($w = g =$ 21 μm). Image taken from [32].

The sample can be moved with respect to the position of the objective in the $x - y$ plane using a Thorlabs motorized translation stage with sub-micrometrical resolution.

2.6 Experimental procedure

In this section we describe the experimental procedure that we used to collect the flow profiles of the fluids inside the microfluidic channels. Once the channel is set on the microscope, we choose an x, y point using the motorized translational stage and select the ROI. The ROI is always adjusted in position to have the gap in the left part. This ensure consistency of the field of view between the measures and between forward and backward flows. This procedure is done under bright field. After that, we apply the pressure drop and let the fluid to completely fill the channel and the tubes. This step is necessary to ensure the hydraulic resistance is constant during the experiment.
At this point the channel is covered with a shade to suppress every light sources other than the laser beam. The channel is then irradiated with the laser beam and the top and bottom walls z coordinates are identified. Then the data acquisition begins. A single measure of a flow profile consists of a series of stack of images captured at $x = L/2$ and at a given y position. The entire measure is automated by using a custom macro. The motorized microscope moves the objective over the entire channel height (H) starting from the bottom wall coordinate fund in the previous step up until the top wall coordinate. The objective is moved with steps $\Delta z = 2\,\mu$m, and at every step a fixed number of frames N_f is registered by the camera. For the measures shown in this thesis, this number was set to $N_f = 1500$. At each step a single file containing N_f frames is generated.
The final result is a collection of files, each correspondent to a specific z coordinate, relative to the selected $x - y$ point. The exposure time τ_{exp} is set depending on the flow velocity, as faster flow will require shorter exposure time in order to avoid deforming the shape of the tracers. In the measures reported we set $\tau_{exp} = 500\,\mu$m, corresponding to a frame rate of 2000 fps.
Finally, a *3D scan* is performed by taking several flow profiles at different y position within the channel. By doing so we take a measure of $v(z, y)$ as a function of both the channel height z and the channel width y is taken, and we refer to that as a *3D scan*.

2.7 Data analysis

The image stacks collected during the experiment were analysed using a custom TrackMate algorithm [49, 55]. In this section we outline the various steps that lead to the generation of the flow profiles.

1. **Tracers detection**: The tracers irradiated by the laser appear to the camera as bright white spots on a dark background when they are in the focal plane. We used a "Difference of Gaussian" (DoG) alghorithm to detect them in every frame in an automated way. The important parameters to be set in this stage are the *treshold* to define the difference between tracers and background and the expected diameter of the spots.

2. **Quality selection**: The algorithm proceed by filtering the spots by the compatibility between the required diameter and the detected one. Also another filter is put to exclude points that doesn't present sharp boundaries. This step is important to filter out spots that might be out of the focal plane (shallow borders, low brightness) or object that might not be tracers at all (different diameters). This is done by choosing an appropriate *quality* parameter.

3. **Tracking**: The algorithm at this stage make a comparison between the position of the detected spots in different frames. The attempt is to correctly identify which spots correspond to the same tracer. This step requires three parameters:

    - *Linking max distance*: This is the maximum distance between the spots from one frame to another allowed for the program to link them to the same tracer.
    - *Gap-closing max distance*: This is the maximum distance between two tracks to be linked as one. It is important whenever a spots might not recorded in one frame, as this allows to have only one track anyway.
    - *Max Frame Gap*: This is the maximum number of frames between two non consecutive same-spot detection allowed. Together with the *Gap-closing max distance* allows to reconstruct tracks also whenever the spot detection is incomplete between the frames.

4. **Track selection**: Similarly to the filtering we did on the spots, this step put a quality filter on the detected tracks to exclude unreliable ones. The parameters to be set are:

    - *Track mean quality*: This parameter is a quality threshold value for the tracks. The quality of a track is calculated by averaging the quality values of the spots that define the track.
    - *Number of spots*: The program can filter out the tracks based on the minimum number of spots that make up the track itself. This allows us to eliminate tracks made up of few spots that might not be reliable and keep only longer tracks.

5. **Tracers speed analysis**: In this step the program uses the detected tracks to calculate the average speed of the tracers in the stacks of images, each corresponding to a specific $x-y$ plane in the z direction, as described in section 2.6. The velocity of a spot between two consecutive detections in a track is calculated as $v = \Delta x/\Delta t$, where Δt between one frame and the next is defined by the exposure time, and the Δx is calculated from the detected position of the spots. The velocity of the track v_{track} is then calculated as the average of those v values that made up the track. Finally, the flow velocity for the specific z considered ($v_{flow}(z)$) is defined as the average of the v_{track} obtained for that z. The correspondent uncertainty is defined as the *standard deviation* of the distribution of v_{track} values.

6. **Reconstruction of the flow profiles and 3D scan**: By repeating the previous steps for every z is possible to obtain a flow profile inside the channel at a given $x-y$ point along the z direction. We then normalize the z coordinate by setting $z = 0\,\mu$m at the center of the channel. The coordinates of the walls thus becomes $z = \pm H/2$. The patterned wall is chosen to be at $z/H = +1/2$. It is possible to repeat this procedure by taking a series flow profiles moving along the y direction at a fixed x, as described in section 2.6, obtaining what we have defined as a *3D scan* of the flow inside the channel.

A complete scheme that visually represent the steps described in this section is reported in fig. 2.13.

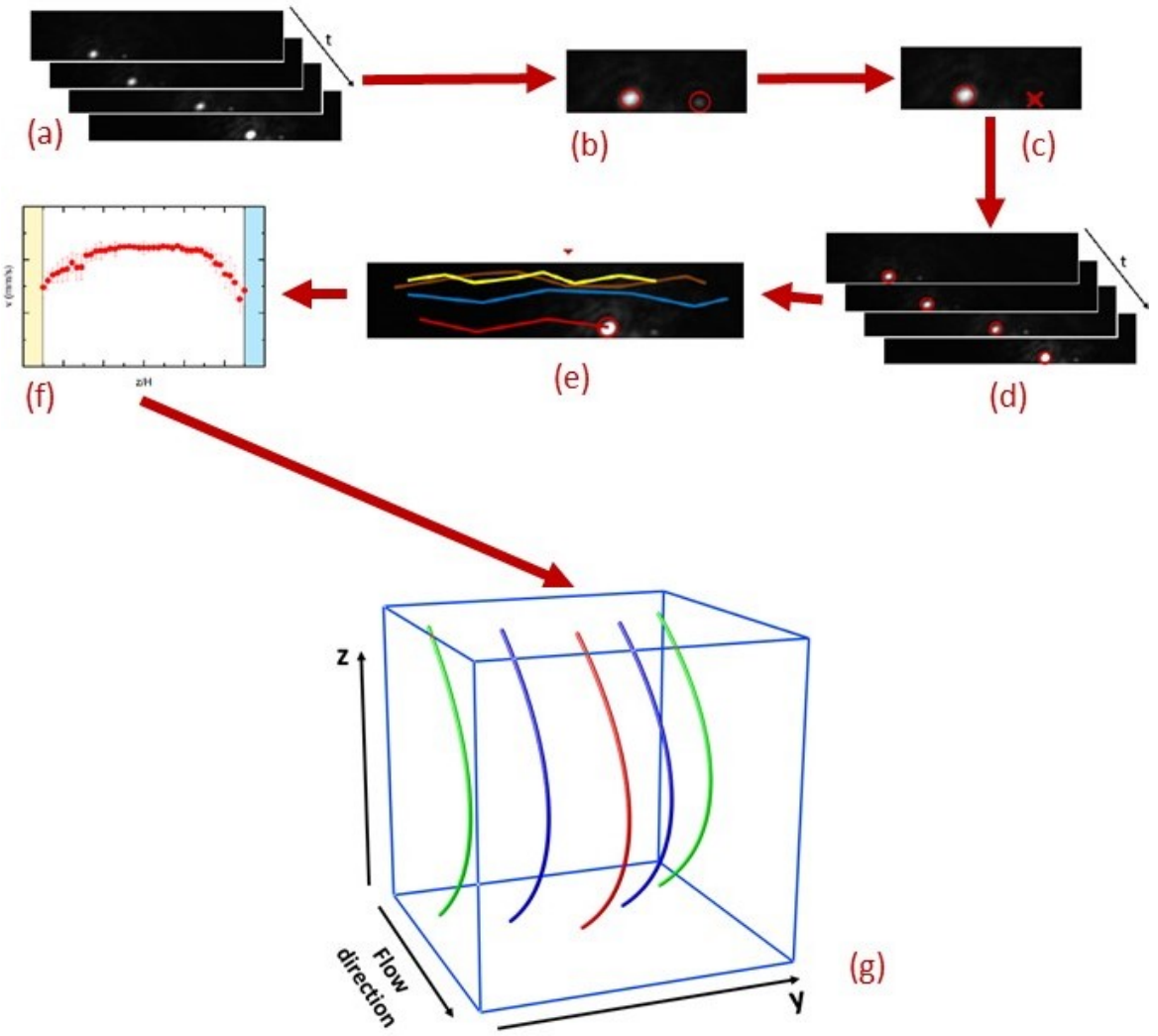

Figure 2.13: Scheme of the steps of data post-processing and analysis. (a) The image stack collected by the experiment. (b) The spot detection with the DoG algorithm. (c) Data cleaning by means of filters on detected spots. (d) Post-processed stack with high quality detected spots. (e) Tracks detection and quality filtering. (f) Reconstruction of the flow profile $v(z)$ for a fixed $x - y$ point. (g) Reconstruction of the flow profile inside the channel at fixed x coordinate by composition of flow profiles at different y coordinates. Image adapted from [32].

From the flow profiles we can extract many properties about the fluid flow such as the plug velocity and the slip velocities at the top and bottom walls. Also, the local rheology of the fluid inside the channel can be obtained: by deriving the flow profile with respect to the z coordinate is possible to obtain the shear rate $\dot{\gamma}$ using eq. (1.1.14). By choosing an appropriate functional form for the viscosity η, such as the power law model described of eq. (1.2.13), we can also calculate the stress σ using eq. (1.2.5).

Chapter 3

Results

In this chapter we will introduce the experimental results obtained by performing 3D Scans for a selection of materials and channels surfaces. In section 3.1 and section 3.2 we will focus on the results obtained for the flow of emulsion. In section 3.3 we will move our attention toward a polymer solution: the Xanthan/water solution at 5000 ppm. In section 3.4 will be reported the result for the more diluted 2500 ppm Xanthan/water solution and in section 3.5 we will study the behaviour of a Newtonian fluid, the anyhrous glycerine. Lastly, in section 3.6, we will discuss our results and make a comparison between all the data collected to infer some properties of the 3D flow of complex fluids inside a microfluidic channel.

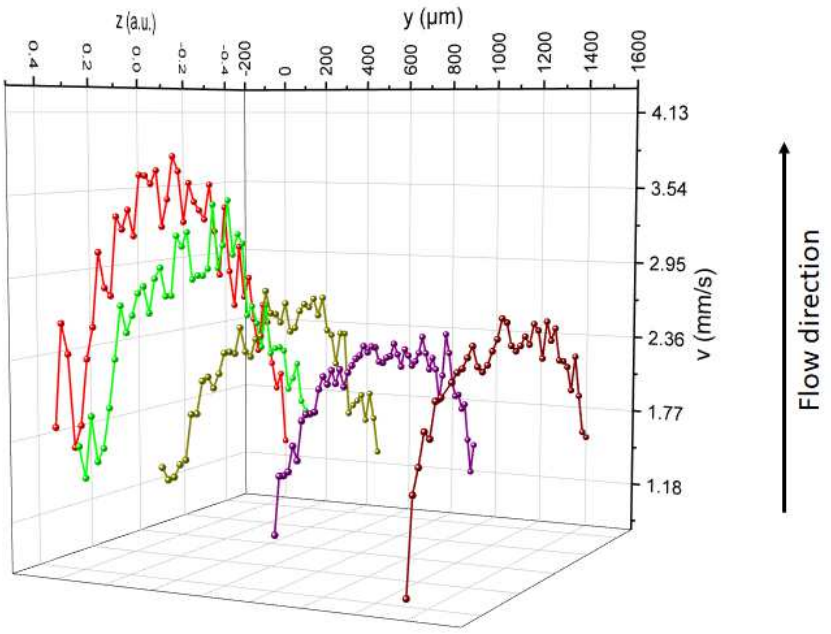

3.1 Reproducibility of emulsion measures

First, in order to study the reproducibility of the measures taken with the $\phi = 0.6$ concentration emulsion, we performed three different identical 3D scan with the same protocol, same pressure drop ($\Delta P = 150\,\text{mbar}$) and the same channel (V-Grooves, $\alpha = 45°$, $w^* = 25\,\mu\text{m}$, $g^* = 25\,\mu\text{m}$). Two of them are performed with emulsion obtained from the same batch and the 3D scans are performed on consecutive days. Being the 3D scans a heavily time-consuming data collection procedure, it is impossible to collect all the flow profile necessary in a short time span. This comparison is needed to verify if it is sensible to compare measurements taken on successive days. The third measure is performed with emulsion obtained from a different batch.
The resulting flow profiles have been fitted with the eq. (1.3.27) to obtain the relevant statistics.

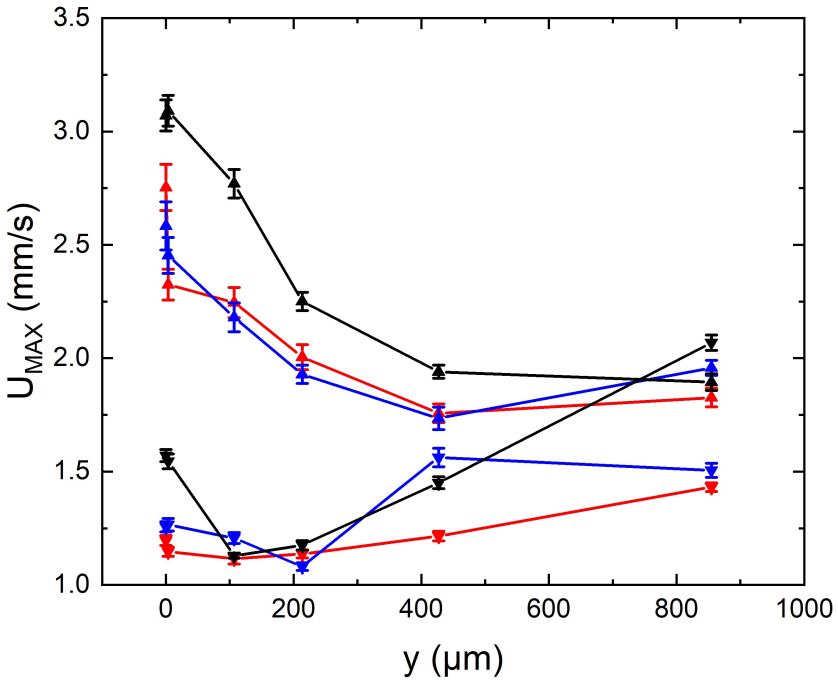

Figure 3.1: Peak velocity U_{MAX} for the forward (upward facing arrows) and backward (downward facing arrows) flows of $\phi = 0.6$ emulsion. In red and blue, the profiles taken with emulsion obtained from the same batch on conseutive days. In black, the profile taken with emulsion coming from a different batch.

The behaviour of the peak velocity U_{MAX} along the y direction of the channel in the three sperimental conditions is shown fig. 3.1.
The 3D scan obtained from the same emulsion (the red and blue curves in fig. 3.1) show a qualitatively consistent behaviour, but there are measurable differences. This could be attributed to a number of factors, including room temperature differences between the measurement and slight differences in the emulsion due to the time passed. This results show that it is reasonable taking measurements on different successive days. The profiles obtained with a different emulsion (the black curves in fig. 3.1) show approximately the same trend, but the U_{MAX} values are this time consistently different.
This shows that the behaviour of the emulsion is very sensitive on the preparation of the emulsion itself. To have reliable data, it necessary to perform all the measures that it is

intended to compare with emulsion coming from the same batch.

3.2 Comparison of emulsion flow at different pressure drops

We performed a series of 3D scans of forward and backward flow of emulsion at $\phi = 0.6$ at various pressures (50, 100, 150 and 200 mbar). The purpose of these measurements is to study how the two profiles moves along the y direction of the channel and to determine if there exist a functional relation between the two.

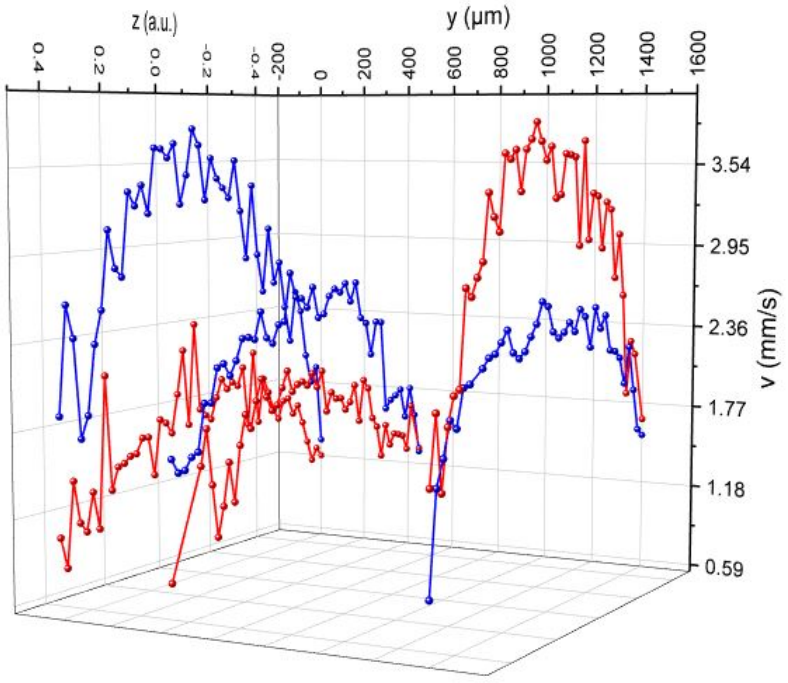

Figure 3.2: A 3D scan of the $\phi = 0.6$ emulsion at $\Delta P = 200$ mbar. In blue are the forward profiles, while in red the backward ones. Only three y points have been represented for visual clarity purpose.

All the profiles taken have been fitted using eq. (1.3.27) to obtain the relevant statistics. In fig. 3.3 are reported the peak velocity U_{MAX} for the forward profiles at the four different ΔP. It is possible to see a common trend of an initial decrase of the peak velocity moving from the center of the channel at $y = 0\,\mu$m toward the lateral wall (situated at $y = 2000\,\mu$m) followed by its stabilization, that appears to happen from the $y = 450\,\mu$m coordinate. The initial is more pronounced in the fastest profiles, namely the $\Delta P = 200$ mbar (black curve) and the $\Delta P = 150$ mbar (green curve).

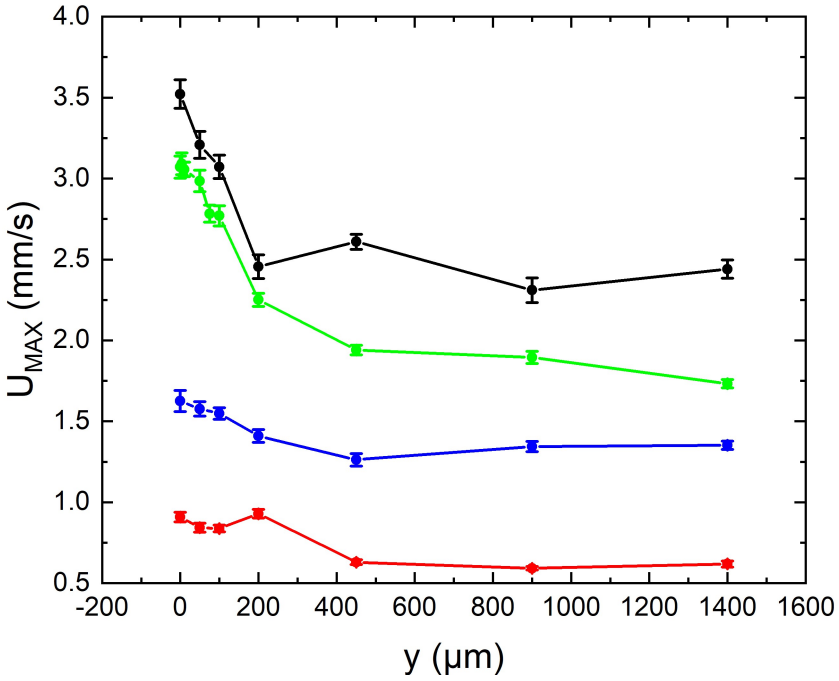

Figure 3.3: Peak velocity U_{MAX} for the forward flows of $\phi = 0.6$ emulsion. The profiles are the $\Delta P = 200\,\text{mbar}$ (black curve), $\Delta P = 150\,\text{mbar}$ (green curve), $\Delta P = 100\,\text{mbar}$ (blue curve) and $\Delta P = 50\,\text{mbar}$ (red curve).

The backward flows, reported in fig. 3.4, show a different behaviour. In this direction, the flow seem to generally accelerate while moving from the center of the channel towards the lateral walls. This trend of the peak velocity $U_{MAX}(y)$ however is non monotonous. It is to be noted that in several cases the peak velocities of the backward profiles in the regions far away from the center are faster than their correspondent forward profiles.

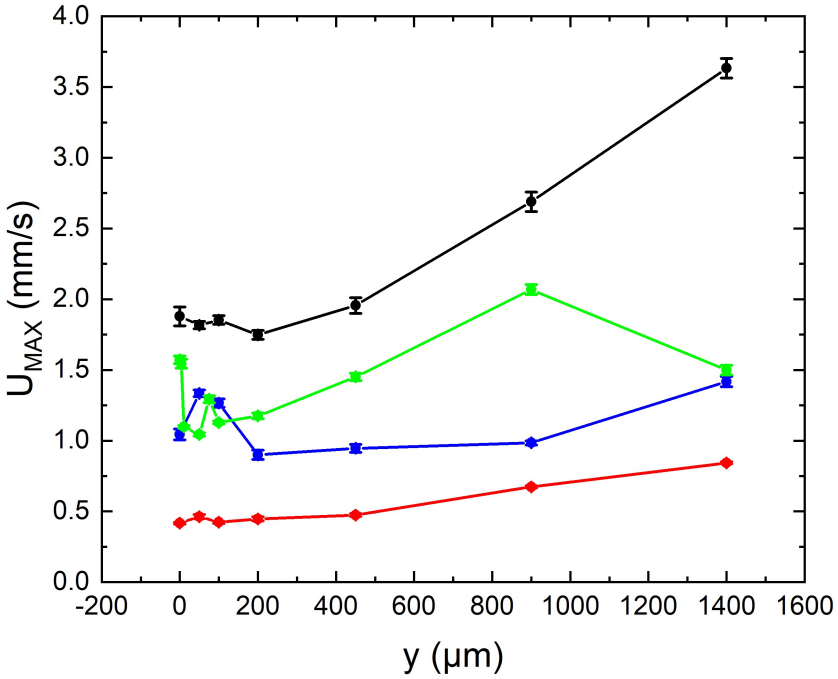

Figure 3.4: Peak velocity U_{MAX} for the backward flows of $\phi = 0.6$ emulsion. The profiles are the $\Delta P = 200\,\text{mbar}$ (black curve), $\Delta P = 150\,\text{mbar}$ (green curve), $\Delta P = 100\,\text{mbar}$ (blue curve) and $\Delta P = 50\,\text{mbar}$ (red curve).

There is thus a qualitatively difference in the behaviour of the flow speed along the y direction in the two different direction.

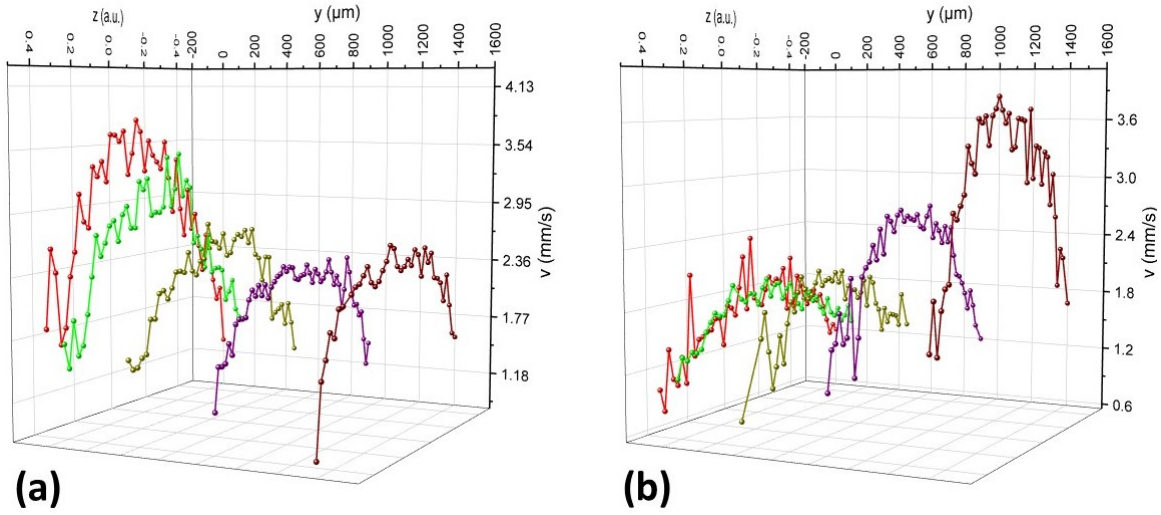

Figure 3.5: 3D scan of the $\Delta P = 200\,\text{mbar}$ flow of $\phi = 0.6$ emulsion. In fig. (a) are reported the forward profiles. It is evident the decrease and subsequent stabilization of the flow speed moving toward the side walls. In fig. (b) are the backward profiles. This time the flow speed increase along the channel while moving away from the center.

While studying the relative velocity of the forward and backward profiles, the important quantity to be considered is the ΔU_{MAX}, the difference between the peak velocity of the forward and the backward profiles. The y profiles of the ΔU_{MAX} are reported in fig. 3.6. The results show that the closure and, in some cases, inversion of the gap

between the forward and backward profiles are slow and do not drop immediately away from the points of the grooves.

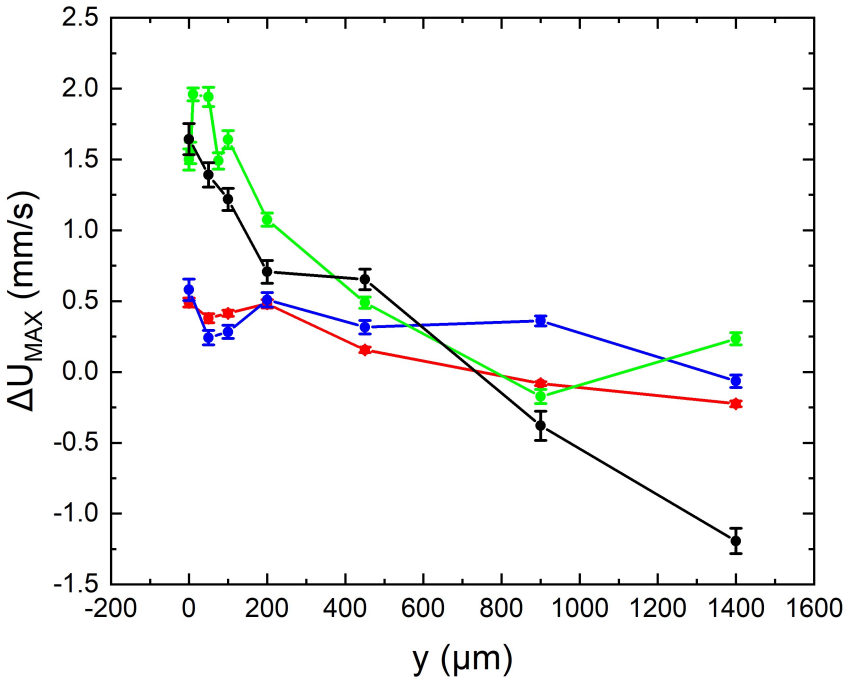

Figure 3.6: Peak velocity difference ΔU_{MAX} for $\phi = 0.6$ emulsion. The profiles are the $\Delta P = 200\,\text{mbar}$ (black curve), $\Delta P = 150\,\text{mbar}$ (green curve), $\Delta P = 100\,\text{mbar}$ (blue curve) and $\Delta P = 50\,\text{mbar}$ (red curve).

Equation (1.3.27) suggest the presence of a z_{MAX} such that $U(z_{MAX}) = U_{MAX}$ that should be different from 0 (the center of the channel along the vertical direction) due to the uneven stress profile caused by the smooth top wall and the grooves patterned bottom one. By fitting the profiles with eq. (1.3.27), it is possible to extract this quantity, however the z_{MAX} seems to oscillate around $z = 0$ and no significant trend is observed. The z_{MAX} along the y direction of the channel for the four pressure drops are reported in fig. 3.7.

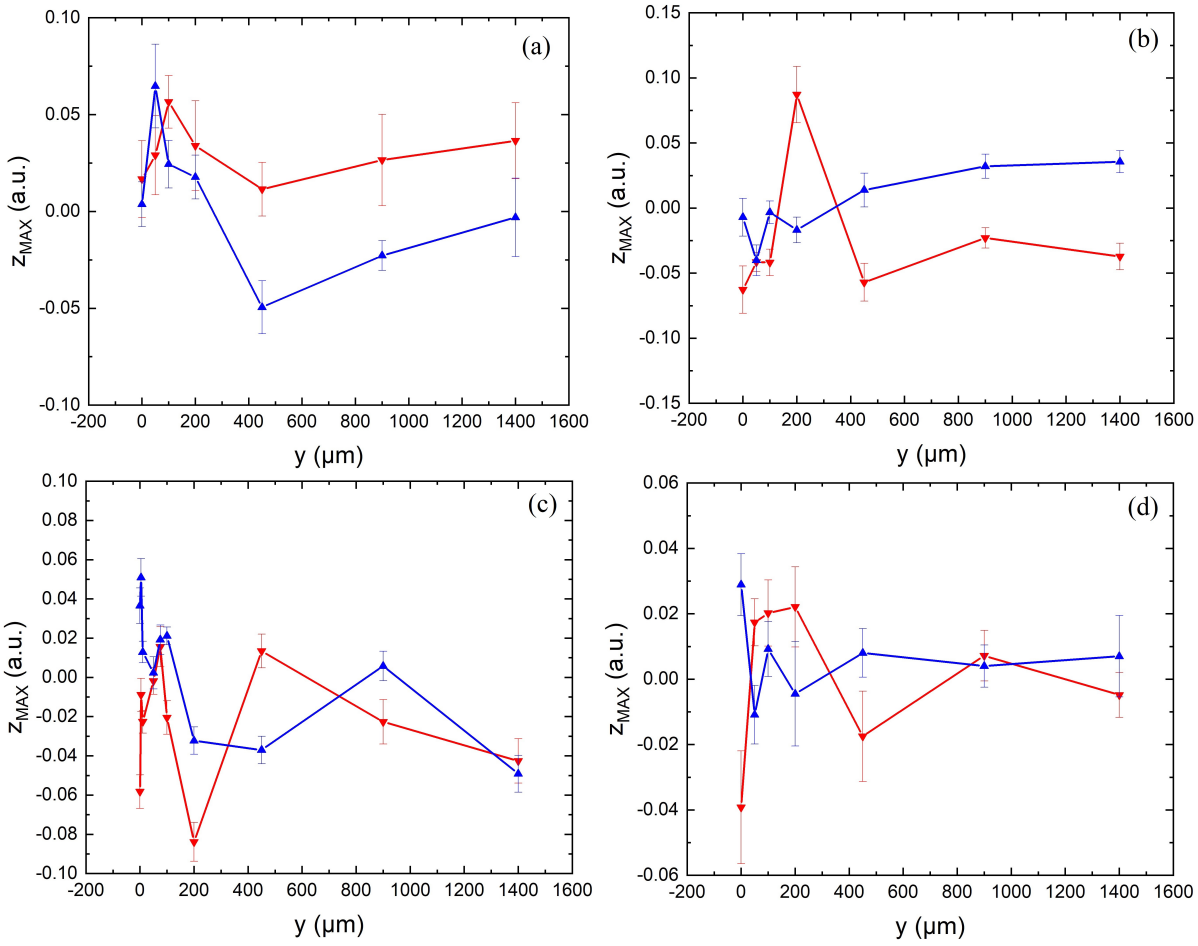

Figure 3.7: z_{MAX} (eq. (1.3.27)) positions for $\phi = 0.6$ emulsion at different pressure drops. The forward profiles are the blue curves with the upward facing arrows, while the backward profiles are in red with downward facing arrows. Fig. (a): $\Delta P = 50\,\text{mbar}$. Fig. (b): $\Delta P = 100\,\text{mbar}$. Fig. (c): $\Delta P = 150\,\text{mbar}$. Fig. (d): $\Delta P = 200\,\text{mbar}$.

3.3 Xanthan/Water at 5000 ppm

The results discussed in the previous section led us to consider what properties of the emulsion could explain the behaviour. At $\phi = 0.6$, as we explained in section 1.4.2, we we are well below the critical concentration to have cooperativity in the bulk of the fluid, and the yield stress appears to be very little, as we cannot see, even at the lowest pressure drop measured ($\Delta P = 50\,\text{mbar}$) any central plug. The emulsion characterization, described in section 2.2.1, showed an index flow $n = 0.849 \pm 0.006$, indicating a shear-thinning behaviour. To continue investigating the forward-backward flow asimmetry we tried with a shear-thinning polymer solution (the Xanthan/water 5000 ppm solution described in section 2.3.2).

The polymer solution offer numerous advantages by an experimental point of view over the emulsion. It is cheap and fast to produce, and is less prone to deteriorating its internal structure. We tested the Xanthan/water 5000 ppm solution in the same channel used for the emulsion (V-Grooves, $\alpha = 45°$, $w^* = 25\,\mu\text{m}$, $g^* = 25\,\mu\text{m}$) at the pressure drop $\Delta P = 150\,\text{mbar}$. We used eq. (1.3.27) to fit the profiles and obtain the relevant

statistics. In fig. 3.8 we can see the peak velocity U_{MAX} for the forward and backward flows. The forward peak velocity show the an oscillating trend moving toward the lateral wall, while the backward flow show a substantial decrease in the same direction.

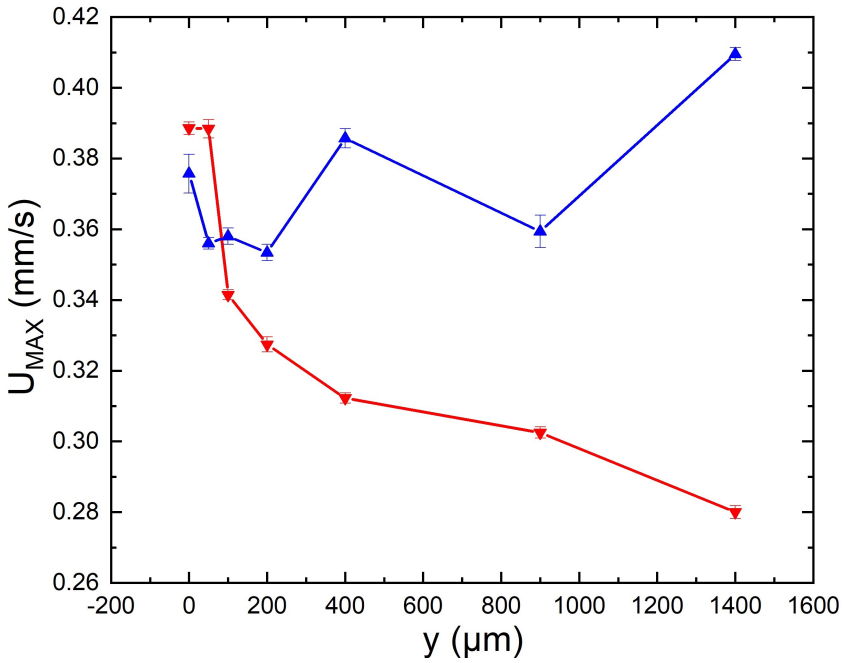

Figure 3.8: Peak velocity U_{MAX} for the forward (blue curve, upward facing arrows) and backward (red curve, downward facing arrows) flows of Xanthan/water 5000 ppm solution at pressure drop $\Delta P = 150$ mbar.

The difference between the peak velocity of the forward and the backward profiles ΔU_{MAX} is shown in fig. 3.9. The combined stability of the forward profiles and the decrease of the backward ones causes this time a previously unseen increase of ΔU_{MAX} moving away from the center of the channel.

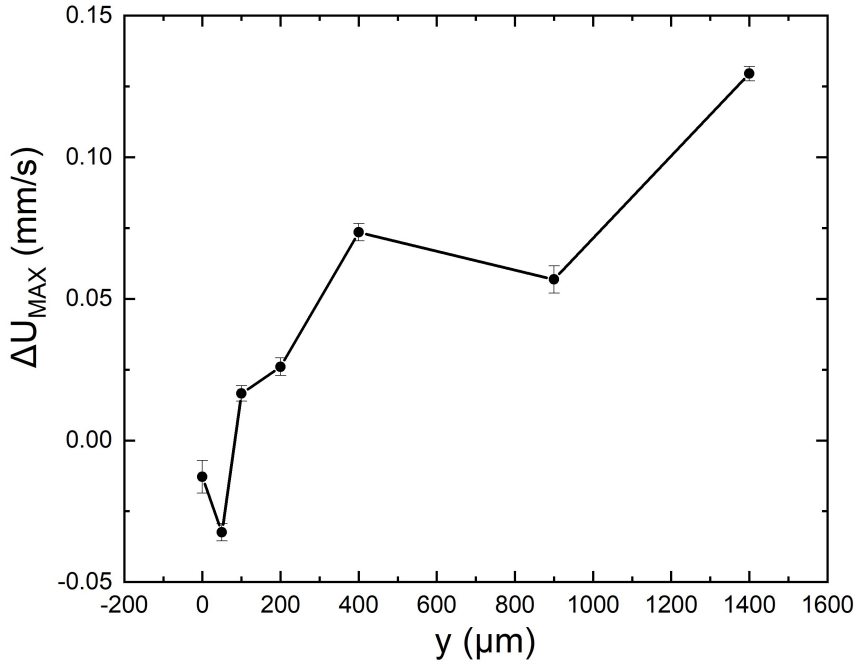

Figure 3.9: Peak velocity difference ΔU_{MAX} for the Xanthan/water 5000 ppm solution at pressure drop $\Delta P = 150$ mbar.

As with the measures with the emulsion, we are unable to find a significant pattern for the z_{MAX} quantity. The z_{MAX} values for the forward and backward profiles are reported in fig. 3.10.

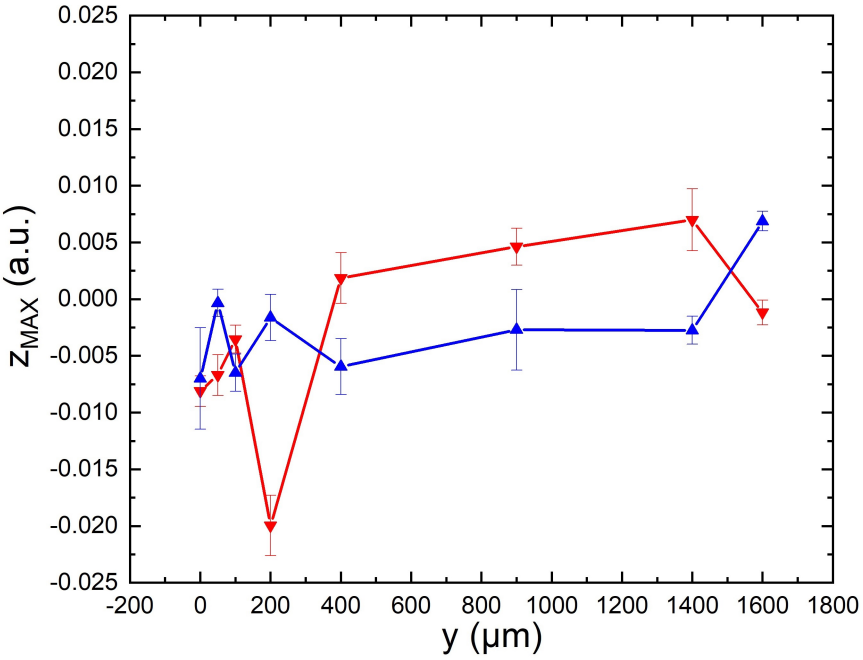

Figure 3.10: z_{MAX} positions for the forward (blue curve, upward facing arrows) and backward (red curve, downward facing arrows) flows of Xanthan/water 5000 ppm solution at pressure drop $\Delta P = 150$ mbar.

The results with the polymer solution differs in a qualitative fashion with those of the

emulsion.
After the completion of the measures with the Xanthan/water 5000 ppm solution the channel used broke. Due to the unavailability of the same patterned surface to produce a new one, we settled for continuing the experiment using a new channel that has similar characteristics (V-Grooves, $\alpha = 45°$, $w^* = 21\,\mu$m, $g^* = 21\,\mu$m). We also performed 3D scans using a straight grooves channel (Straight Grooves, $\alpha = 90°$, $w = 15\,\mu$m, $g = 15\,\mu$m) chosen to have the same g and w of the new V-Grooves channel. Lastly, we also performed measures using a smooth channel, obtained using a microscope slide in place of the patterned surface for the bottom wall.

3.3.1 Comparison between two V-grooves channels with different g and w

We first performed the 3D scan at the same pressure drop of $\Delta P = 150\,$mbar with a new batch of Xanthan/water solution at 5000 ppm. It has to be noted that, while the emulsion preparation is a complex procedure with many possible factor that could contribute to a final different product, the Xanthan/water solution is a much more stable solution with a straightforward preparation procedure. It should be safe to affirm that it is unlikely that the two batches would differ much. Unfortunately, we cannot test the new batch in the old channel due to the aforementioned rupture. Moreover, the variation of the grooves of the channel if of $4\,\mu$m over the total width of the grooves $25\,\mu$m. While this is not an insignificant variation, it has to be noted that those scale are gigantic when compared with the characteristic lenght of the polymer chain of the Xanthan gum that are of the order of $\sim 100\,$nm [52].
In fig. 3.11 are reported the velocity profiles along the channel for the new batch in the new channel as well as the ones for the old batch in the old channel. As we can see, the new profiles are much faster, and have the same qualitative behaviour along the channel, with a strong decrease of the speed around the center of the grooves followed by a smoother decrease moving toward the wall. It has to be noted that the backward flow is consistently faster for all the channel observed. While the backward flow for the old batch seems to have the same qualitative trend of the new measures, the forward flow of the old batch is substantially different, being stable for all the observed channel.

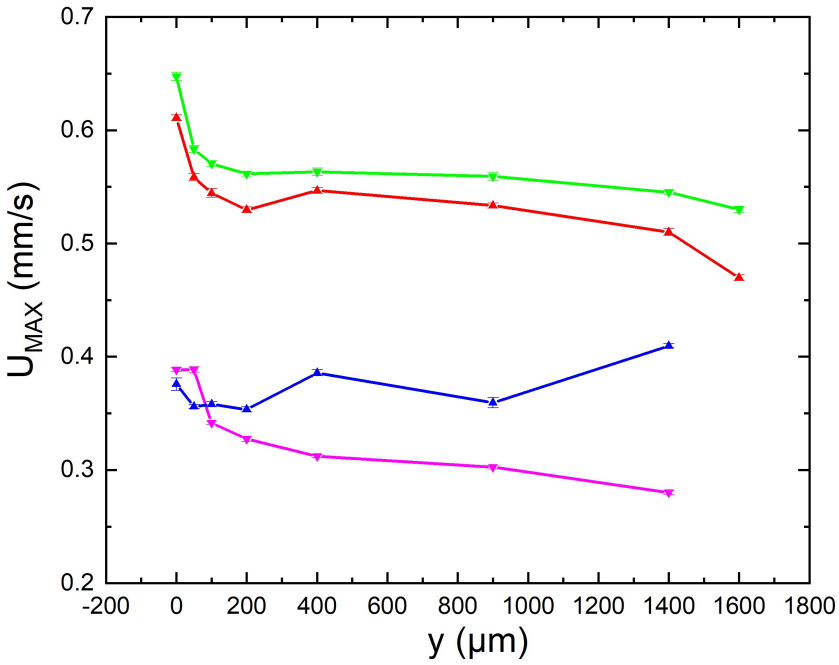

Figure 3.11: Peak velocity U_{MAX} for forward and backward flow of the Xanthan/water 5000 ppm solution at pressure drop $\Delta P = 150$ mbar in the two experimental conditions. New solution in new channel forward (red curve, upward facing arrows) and backward (green curve, downward facing arrows) flows. Old solution in old channel forward (blue curve, upward facing arrows) and backward (magenta curve, downward facing arrows) flows.

Due to those differences the profiles for ΔU_{MAX} in the two experimental conditions are completely different, with the ΔU_{MAX} of the new measures standing stable for all the observed channel. The profiles for the ΔU_{MAX} are reported in fig. 3.12. As in all cases before, we were unable to find a pattern for the z_{MAX} parameter, that oscillates around the $z = 0$ value.

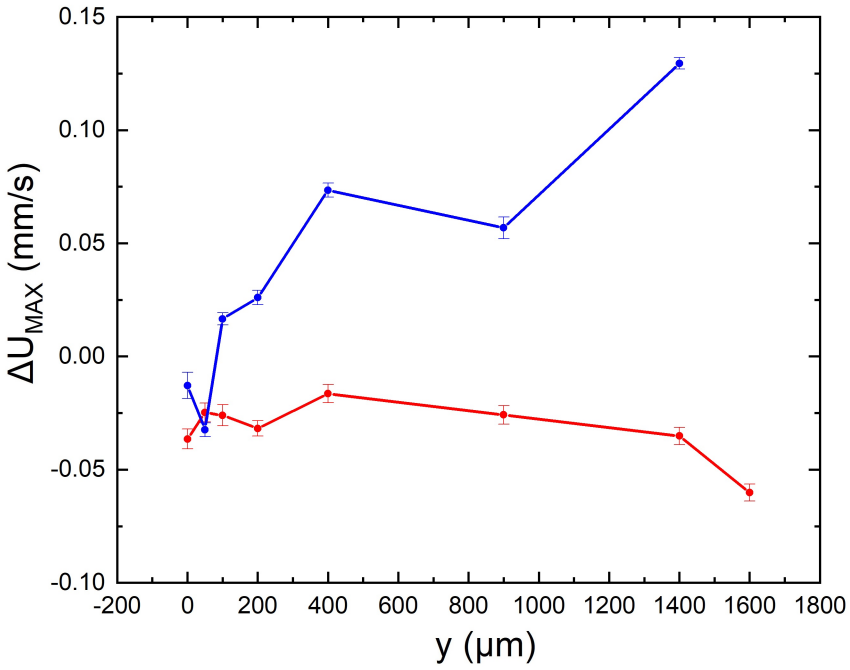

Figure 3.12: Peak velocity difference ΔU_{MAX} for Xanthan/water 5000 ppm solution at pressure drop $\Delta P = 150$ mbar in the two experimental conditions. Old batch and old channel (blue curve) and New batch and new channel (red curve).

3.3.2 Comparison between three different channels

In this section we report the results obtained for the Xanthan/water 5000 ppm solution flow at pressure drop $\Delta P = 150$ mbar in the three different channels we introduced in the last section:

- V-Grooves, $\alpha = 45°$, $w^* = 21\,\mu$m, $g^* = 21\,\mu$m
- Straight Grooves, $\alpha = 90°$, $w = 15\,\mu$m, $g = 15\,\mu$m
- Smooth channel

As we said, the V-grooves channel has the same $g = g^*\text{sen}(\alpha)$ and $w = w^*\text{sen}(\alpha)$ of the Straight grooves one. The purpose of this comparison is to obtain a clear picture of the role of the grooves in the observed difference in the forward and backward flow in the channel.
Obviously, there is no privileged direction in the Straight grooves channel and in the Smooth one. The geometry is completely symmetric and the label "forward" and "backward" are completely arbitrary. Those label are anyway consistent throughout all measures. Labeling the tubes that connect the fluid reservoir at the channel as "inlet" and "outlet", the forward flow is from the inlet to the outlet and vice versa for the backward flow. This is necessary to have consistence between measures.
The velocity profiles in the y direction of the three channel are reported in fig. 3.13. It is possible to see that the same qualitative trend observed in the V-Grooves also in the Straight Grooves and in the Smooth channel. In the smooth channel is the "forward" flow to be faster. In fig. 3.13(d) are reported the velocity profiles $v(z)$ for the forward flow at $y = 0\,\mu$m, the center of the channel, in the three channels. It is possible to see that

the shape of the profiles is almost identical, but they differs in the speed of the central plug region.

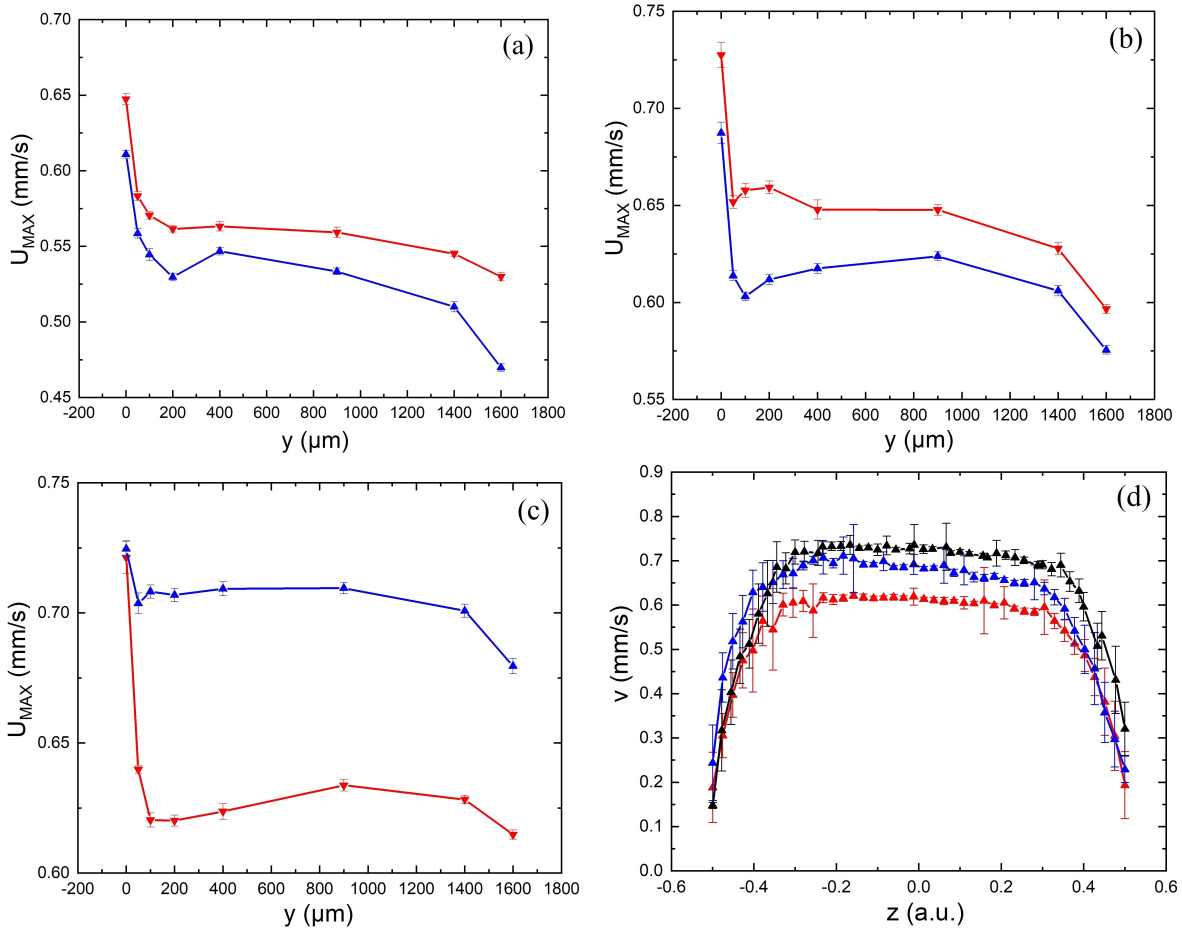

Figure 3.13: Peak velocity U_{MAX} for Xanthan/water 5000 ppm solution at pressure drop $\Delta P = 150$ mbar in different channels, the forward flows are the blue curve with upward facing arrows, while the backward flows the red ones with downward facing arrows. (a) V-Grooves, (b) Straight Grooves and (c) Smooth channel. In (d) are reported the velocity profiles $v(z)$ for the forward flow at $y = 0\,\mu$m (center of the channel) for the V-Grooves channel (red curve), Straight Grooves channel (blue curve) and Smooth channel (black curves).

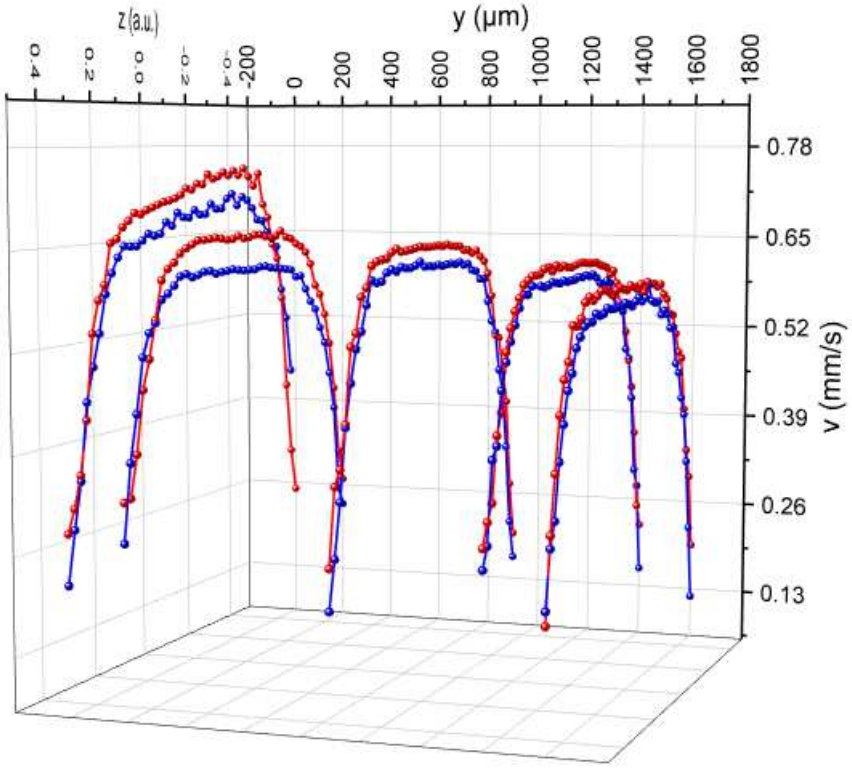

Figure 3.14: A 3D scan of the Xanthan/water 5000 ppm solution at pressure drop $\Delta P =$ 150 mbar in the Straight Grooves channel. In blue are the forward profiles, while in red the backward ones. It is possible to see that even in the absence of V Grooves we have a difference between the flows in the two direction and a rapid decrease of the speed in the central area of the channel. Only five y points have been represented for visual clarity purpose.

The profiles for the peak velocity difference ΔU_{MAX} are reported in fig. 3.15. The ΔU_{MAX} in the Smooth channel appears to be different from the other two due to the strong initial separation between the forward and backward flow speed in the central region of the channel.

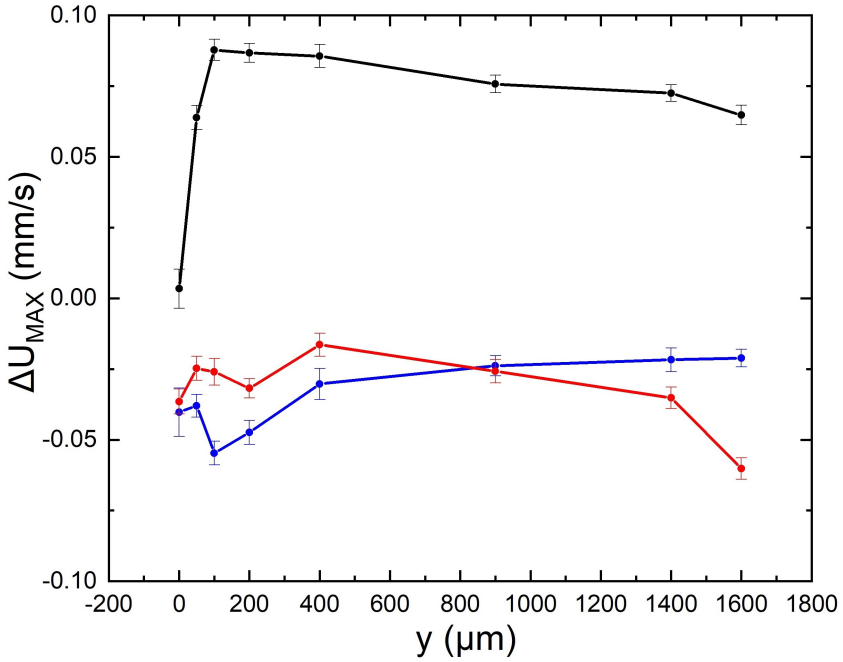

Figure 3.15: Peak velocity difference ΔU_{MAX} for Xanthan/water 5000 ppm solution at pressure drop $\Delta P = 150$ mbar for the V-Grooves channel (red curve), Straight Grooves channel (blue curve) and Smooth channel (black curves).

Also in this case, it was not possible to observe a pattern for the z_{MAX} parameter.

3.4 Xanthan/Water at 2500 ppm

We continued the exploration of the 3D behaviour of the flow inside the microfluidic channels by using a more diluted Xanthan/Water solution at 2500 ppm and a Newtonian viscous fluid, using pure Glycerine (Sigma-Aldrich). The 2500 ppm solution shows a higher value of the n parameter with respect to the 2500 ppm one, as described in section 2.3.2. This means that the decrease of the apparent viscosity with the shear rate is less pronounced. The purpose of those measures is to try to identify if the thinning index is responsible for the complex behaviour of the flow in the channels.
In this section we report the results obtained for the Xanthan/water 2500 ppm solution flow at pressure drop $\Delta P = 50$ mbar in the three different channels. It was not possible to perform the measure at the same pressure drop $\Delta P = 150$ mbar used with the 5000 ppm solution, as the lower viscosity would allow for higher velocities that we would not be able to measure due to the camera employed frame rate limits. The velocity profiles in the y direction of the three channel are reported in fig. 3.16.
This time, the qualitative trend of the flow is inconsistent between the channels and with the measures with the 5000 ppm solution. In the V Grooves channel velocity profiles, reported in fig. 3.16(a), we observe an increase of flow speed moving away from the center of the grooves followed by a strong decrease in the regions towards the lateral walls. This decrease begins much earlier for the forward flow, at $y = 200\,\mu$m, than for the backward flow, happening at $y = 900\,\mu$m. In both directions, moreover, the decrease seems to happen in two different fashions, a smoother one followed by a sharper one for $y > 1400\,\mu$m. This last sharp decrease is common to all the three channels and was also observed, in

all the channels, for the 5000 ppm solution in fig. 3.13(a), fig. 3.13(b) and fig. 3.13(c).
In fig. 3.16(b) are reported the velocity profiles along the channel for the Straight Grooves. It is possible to observe a qualitative difference in the two curves: the forward flow have a sharp decrease immediately away from the center of the channel and regaining speed before the decrease at $y > 1400\,\mu$m, while the backward one have a slight increment of speed moving away from the center of the channel, followed by the same decrease and re-increase of speed of the forward profile. Also the backward flow appears to decrease in speed for $y > 1400\,\mu$m.
In fig. 3.16(c) are reported the velocity profiles along the channel for the Smooth channel. This time the two curves appears very similar up to a constant offset. Here we see a monotone increase of the velocity of the flow moving away from the center of the channel before the decrease for $y > 1400\,\mu$m. It is interesting to note that this time the backward flow is faster than the forward one, while for the 5000 ppm it was the opposite. This inversion is common also to the other two channels. In every channel the faster flow for the 5000 ppm is the slower one for the 2500 ppm. In fig. 3.16(d) it is possible to see the velocity profiles $v(z)$ for the forward flow at $y = 0\,\mu$m, the center of the channel, in the three channels. While comparing this with fig. 3.13(d) is possible to see that also here the shape of the profiles is almost identical and the difference is only in the speed of the central plug region. For the 2500 ppm solution, however, the relative velocity between the channels in the same position is different: in the V Grooves the forward flow is still slower than in the Straight Grooves, but the flow in the Smooth channel is here the slowest of the three, while for the 5000 ppm it was the fastest.

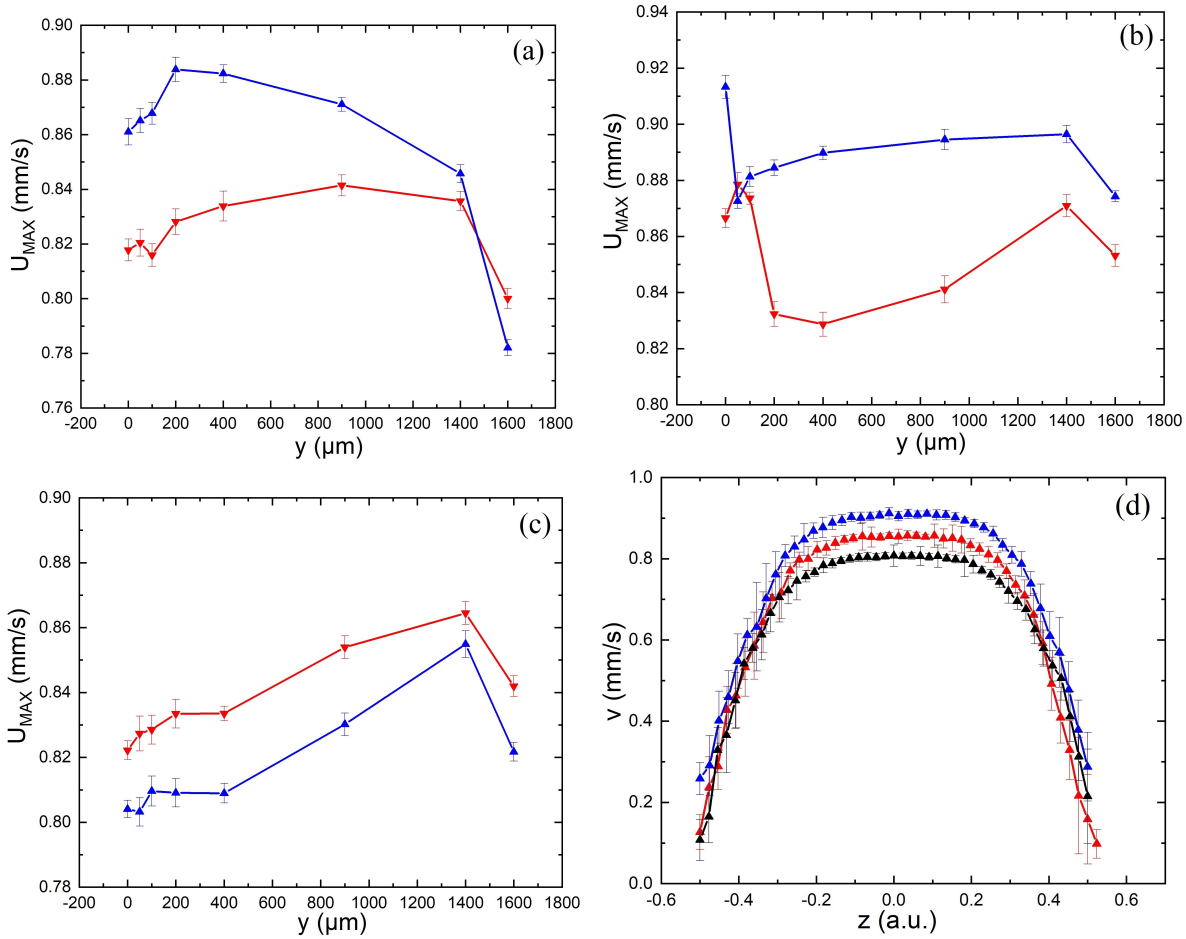

Figure 3.16: Peak velocity U_{MAX} for Xanthan/water 2500 ppm solution at pressure drop $\Delta P = 50$ mbar in different channels, the forward flows are the blue curve with upward facing arrows, while the backward flows the red ones with downward facing arrows. (a) V-Grooves, (b) Straight Grooves and (c) Smooth channel. In (d) are reported the velocity profiles $v(z)$ for the forward flow at $y = 0\,\mu$m (center of the channel) for the V-Grooves channel (red curve), Straight Grooves channel (blue curve) and Smooth channel (black curves).

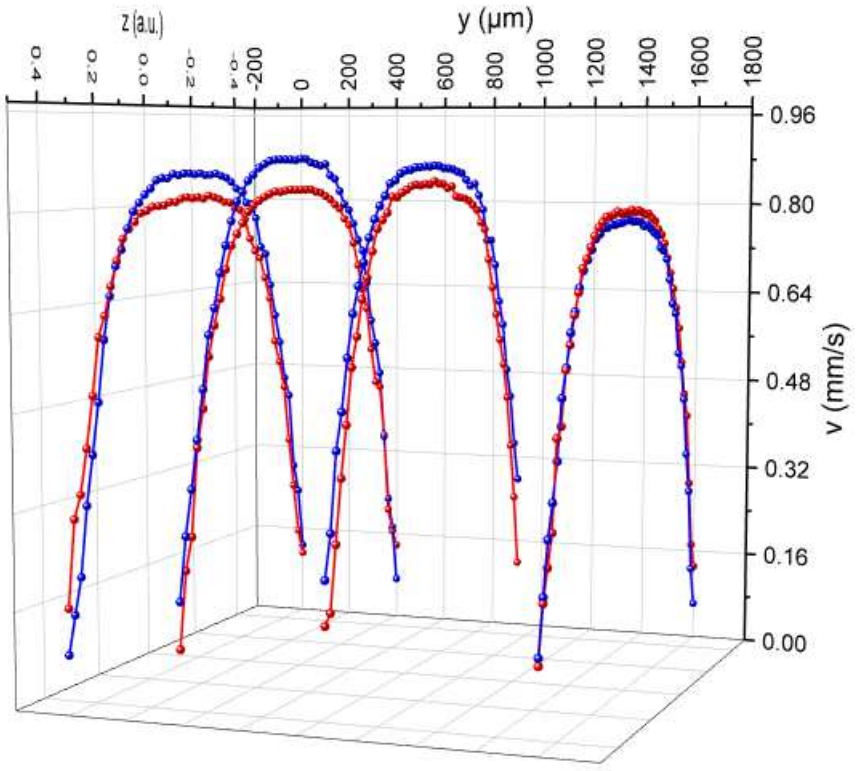

Figure 3.17: A 3D scan of the Xanthan/water 2500 ppm solution at pressure drop $\Delta P =$ 50 mbar in the V Grooves channel. In blue are the forward profiles, while in red the backward ones. It is possible to see that the variation of the forward profiles is faster than that of the backward ones, leading to a surpass of the backward flow in the region towards the lateral wall. Only four y points have been represented for visual clarity purpose.

The profiles for the peak velocity difference ΔU_{MAX} are reported in fig. 3.18. Also this time the ΔU_{MAX} in the Smooth channel appears to be different from the other two standing almost constant for the entire length of the channel due to the fixed separation between the forward and backward flow speed.

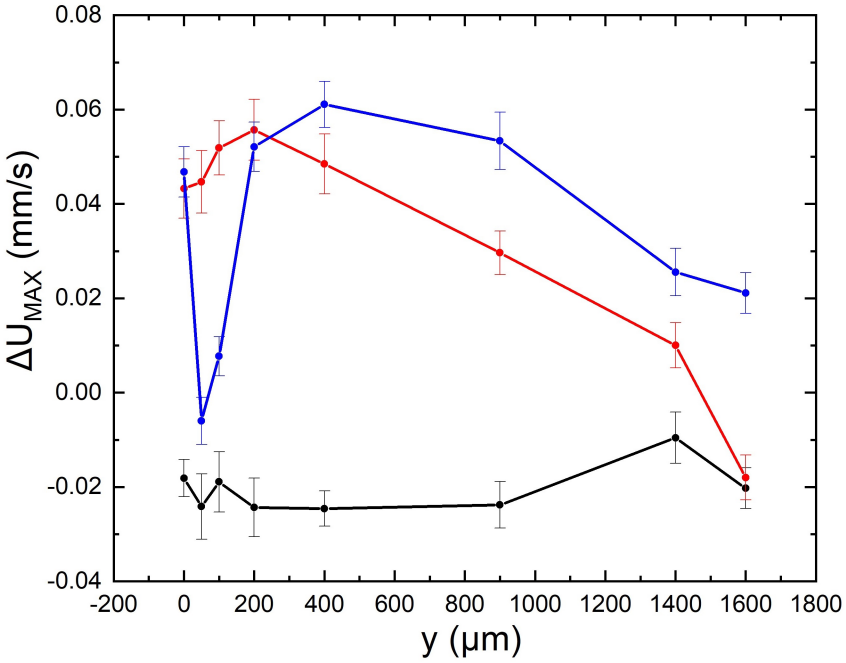

Figure 3.18: Peak velocity difference ΔU_{MAX} for Xanthan/water 5000 ppm solution at pressure drop $\Delta P = 150$ mbar for the V-Grooves channel (red curve), Straight Grooves channel (blue curve) and Smooth channel (black curves).

Also in this case, it was not possible to observe a pattern for the z_{MAX} parameter.

3.5 Newtonian viscous fluid

In this section we report the results obtained for pure anhydrous glycerine at pressure drop $\Delta P = 100$ mbar in the three different channels. The pressure drop was chosen to induce a flow velocity of the same order obtained for the Xanthan/water solutions.

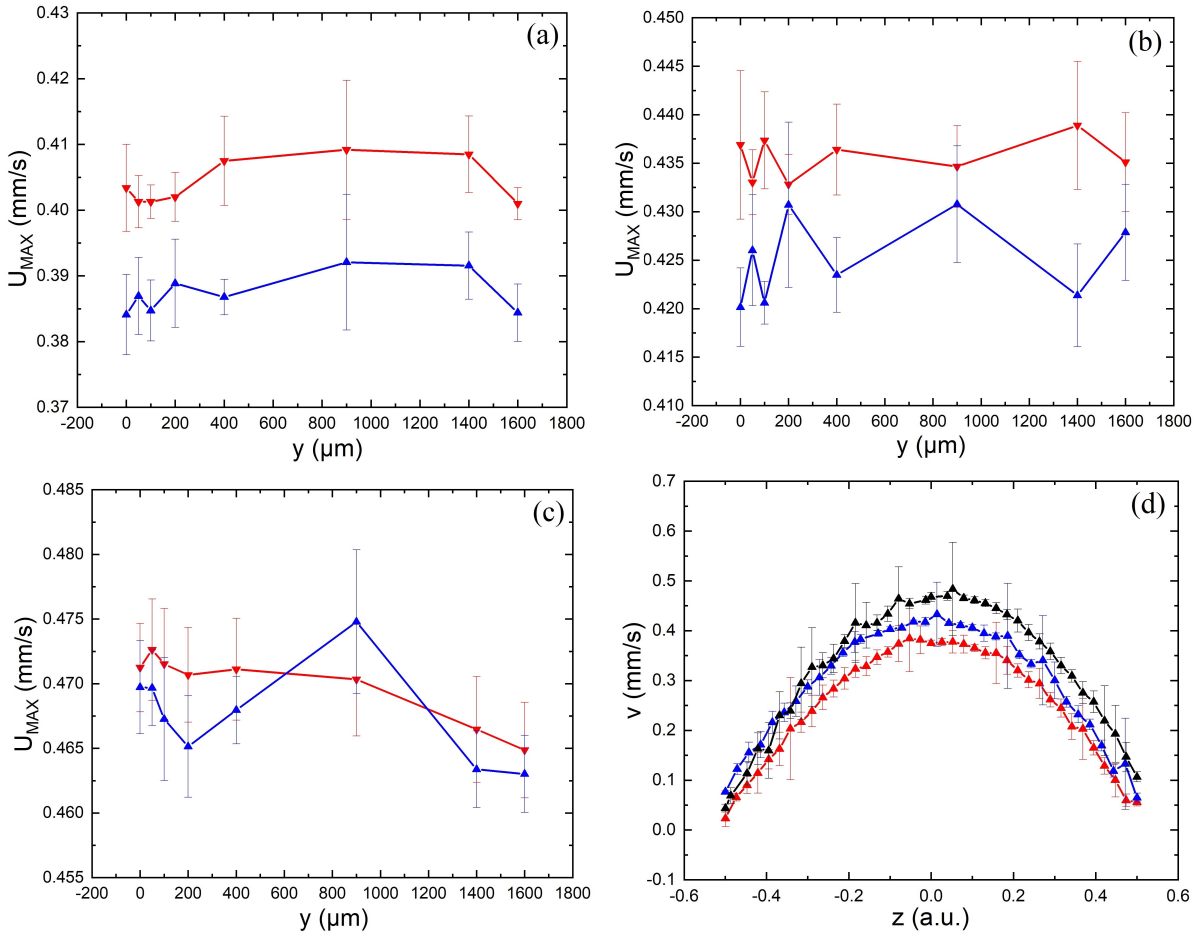

Figure 3.19: Peak velocity U_{MAX} for pure glycerine at pressure drop $\Delta P = 100\,\text{mbar}$ in different channels, the forward flows are the blue curve with upward facing arrows, while the backward flows the red ones with downward facing arrows. (a) V-Grooves, (b) Straight Grooves and (c) Smooth channel. In (d) are reported the velocity profiles $v(z)$ for the forward flow at $y = 0\,\mu\text{m}$ (center of the channel) for the V-Grooves channel (red curve), Straight Grooves channel (blue curve) and Smooth channel (black curves).

The velocity profiles in the y direction of the three channel are reported in fig. 3.19. The flows in the V Grooves channel is reported in fig. 3.19(a). It is possible to observe that in the regions away from the points of the grooves the flow is identical in the two direction up to a constant offset. In the center of the channel the flows have a mirrored behaviour, with the backward immediately decreasing its speed to speed up again and the forward flow increasing its speed and than decreasing slightly.
In the Straight Grooves (fig. 3.19(b)), instead, we observe complete mirror symmetry in the two directions along the entire channel. Lastly, in fig. 3.19(c) we can see the peak velocity profiles for the Smooth channel. It has to be noted that within the error bars, all the points for the forward flow correspond their respective of the backward flow. The only measurable variation is a slight decrease, for both the profiles, moving toward the walls. In fig. 3.20 are reported the profiles measured in the Smooth channel, and it is possible to observe the exceptional agreement between the forward (blue curve) and backward (red curve) flows along the channel.

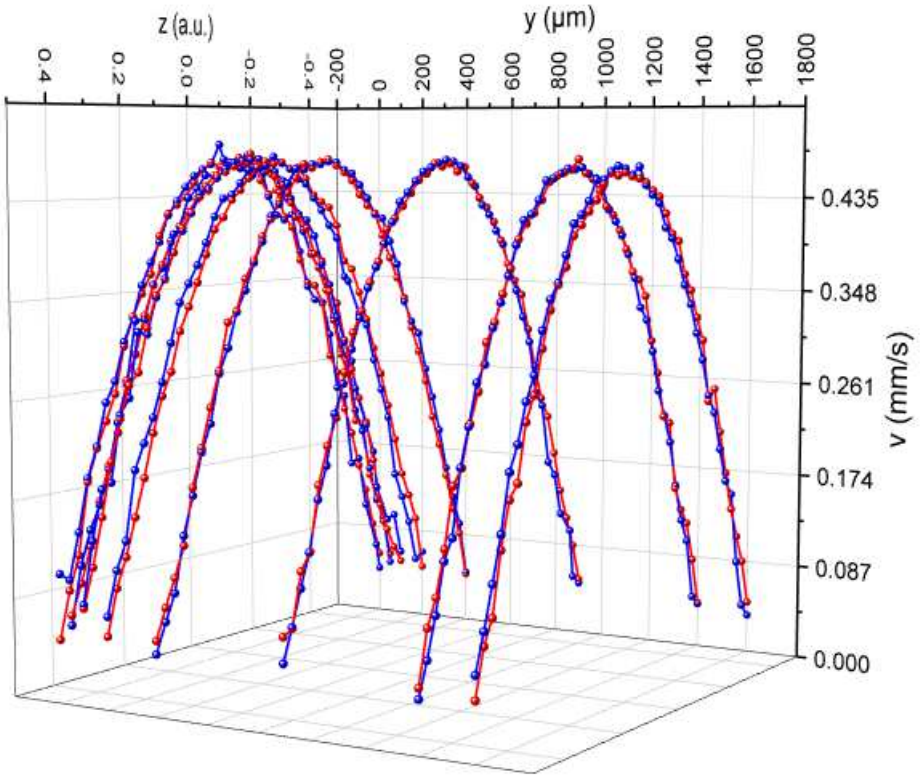

Figure 3.20: A 3D scan of the pure glycerine at pressure drop $\Delta P = 100\,\text{mbar}$ in the Smooth channel. In blue are the forward profiles, while in red the backward ones. It is possible to see the complete superposition of the flow in the two direction for the entire length of the channel.

In the V Grooves and in the Straight grooves the backward flow is moving consistently faster than the forward flow. This is in agreement with the Xanthan/water 5000 ppm solution and opposite to the 2500 ppm one. In fig. 3.19(d) are reported the velocity profiles $v(z)$ for the forward flow at $y = 0\,\mu\text{m}$, the center of the channel, in the three channels. We can see that again the profiles are very similar, except for the maximum velocity. As in the case with the Xanthan/water 5000 ppm solution, the Smooth channel flow is the fastest, followed by the Straight Grooves flow and lastly by the V Grooves flow.
The profiles for the peak velocity difference ΔU_{MAX} are reported in fig. 3.18. Here all the ΔU_{MAX} profiles appear to be almost constant for the entire length of the channel. The profile for the smooth channel is compatible with the value $\Delta U_{MAX}(y) = 0\,\text{mm/s}$.

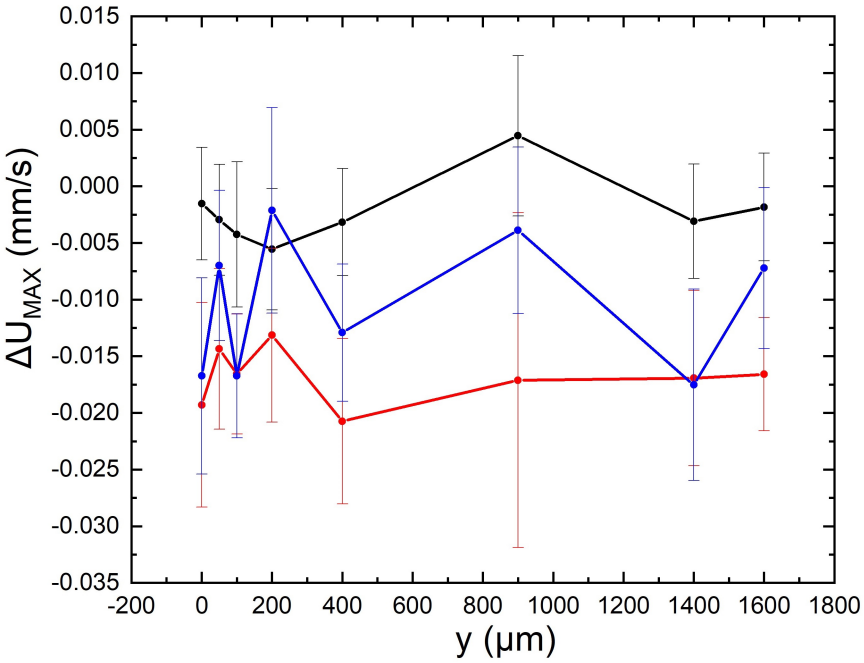

Figure 3.21: Peak velocity difference ΔU_{MAX} for pure glycerine at pressure drop $\Delta P =$ 100 mbar for the V-Grooves channel (red curve), Straight Grooves channel (blue curve) and Smooth channel (black curves).

Also in this case, it was not possible to observe a pattern for the z_{MAX} parameter.

3.6 Discussion

The results obtained for the glycerine described in section 3.5 seem to suggest that the Newtonian fluid moves almost exactly the same in the two direction in every channel. While there are very small measurable differences, those could be imputed to experimental flaws, such as non-ideal channel construction and non complete symmetry of the hydraulic system of the experimental setup in the two directions.
The Xanthan 5000 ppm flows (section 3.3) appear instead to be the the same in the forward and backward directions up to a constant shift. The fact that the shape of the profiles is the same in all the three channels seems to suggest that the grooves play a small role, if any, in the interaction of the fluid with the channel. The 'rigid shift', much greater than the small differences observed for the glycerine, could be instead explained by a stronger coupling of the fluid with the whole channel, due to the complex rheology of the fluid. To support this statement is the fact that the wall effect, i.e. the strong decrease in the velocity of the flow due to the wall presence, seems to appear around $y = 1400\,\mu$m, while it is far outside our measurement range for the glycerine. A stronger coupling between the fluid flow and the channel structure could amplify the systematic errors at the root of the difference observed in the glycerine described in the previous paragraph.
The Xanthan 2500 ppm (section 3.4) show a rigid shift for the Smooth channel, and a more complex behaviour in the two other channels: while the trend is generally the same, it is far more turbulent. It is not easy to interpret this profiles, but it is possible that the fluid, being much less viscous than the 5000 ppm solution and the glycerine and

flowing thus at much greater speed, could be more sensitive to very small variations of the pressure drop or hydraulic resistance of the channel and the hydraulic system as a whole. This could mean that what we observe is in fact a rigid shift, coupled and partially masked by other sources of error.

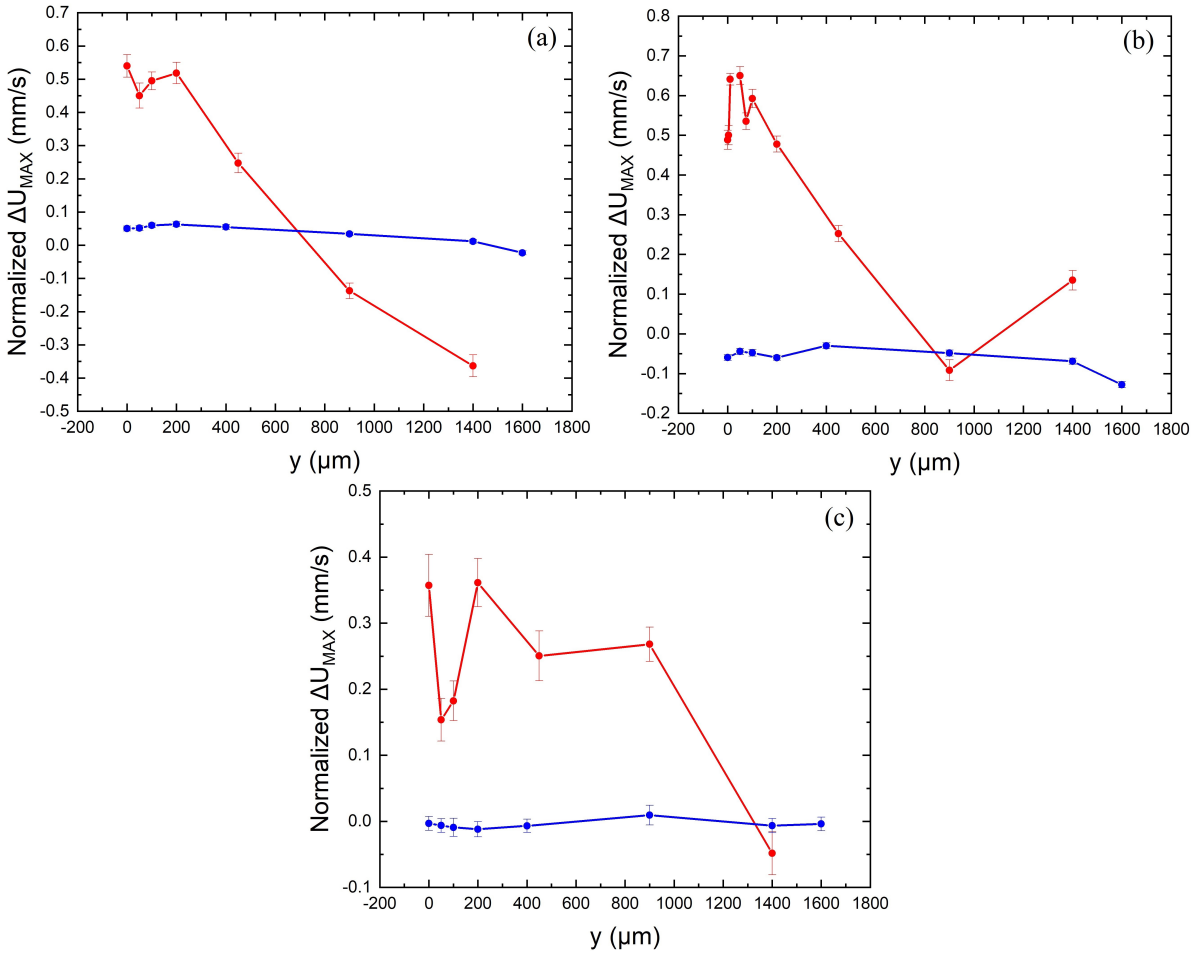

Figure 3.22: Normalized peak velocity difference ΔU_{MAX} for (a) $\phi = 0.6$ emulsion (red curve) and Xanthan 2500 ppm (blue curve) at $\Delta P = 50\,\text{mbar}$, (b) $\phi = 0.6$ emulsion (red curve) and Xanthan 5000 ppm (blue curve) at $\Delta P = 150\,\text{mbar}$, (c) $\phi = 0.6$ emulsion (red curve) and glycerine (blue curve) at $\Delta P = 100\,\text{mbar}$.

Lastly, we focus on the emulsion data, described in section 3.2. This time the profiles are completely different in the two directions. This suggest that the mechanisms that originate the rigid shift observed for the Xanthan solutions could not be the cause of the ΔU_{MAX} observed for the emulsion. The emulsion used ($\phi = 0.6$) have a shear-thinning rheology (section 2.2.2), and the bulk yield stress is, if present at all, negligible (section 1.4.2): it makes sense thus to compare the emulsion behaviour with the Xanthan 5000 ppm and 2500 ppm. In order to make a sensible comparison between different fluids we need to define a new quantity: the *normalized* ΔU_{MAX}, defined as:

$$\text{Normalized}\,\Delta U_{MAX} = \frac{\Delta U_{MAX}}{U_{MAX}(\text{fwd})}\,, \tag{3.6.1}$$

U_{MAX}(fwd) being the peak velocity of the forward profile. This quantity allows us to compare at least qualitatively two fluids that flows at different velocities but are set in motion by the same pressure drop.
In fig. 3.22 we can see the normalized ΔU_{MAX} comparison of the emulsion with the Xanthan 2500 ppm (a) and the Xanthan 5000 ppm (b). In fig. 3.22 (c) we can see also the comparison between the emulsion normalized ΔU_{MAX} and the glycerine one. As we can see, the ΔU_{MAX} for the emulsion are almost an order of magnitude bigger than the others. It seems unlikely that such a difference in the flows could be caused by the same systematic errors in the measurement procedure, if present, that could explain the difference for the Xanthan solutions, nor by the shear-thinning behaviour of the fluid, that would show in systems with much smaller thinning index n such as the Xanthan 5000 ppm. This considerations lead to affirm that the ΔU_{MAX} of the emulsion could not be explained by the shear-thinning properties of the emulsion nor by a measurement flaw.
The justification for a difference between the forward and a backward flow in the dense emulsion ($\phi > \phi_{RCP}$) case was described in section 1.4.4 in terms of droplets interaction with the grooves. Despite not being at such high volume fractions, the $\phi = 0.6$ emulsion is already in the *caged* zone (fig. 1.16) and it is thus possible that the finite size effect of the droplet could be the cause of the difference through the same mechanisms described in section 1.4.4. This hypothesis is corroborated by the fact that no ΔU_{MAX} is observed for $\phi = 0.5$ or in Straight grooves and Smooth channels (section 1.4.4). This could thus be evidence that non-local rheology induced by finite size effect of the droplets in an emulsion is already present at concentrations $\phi < \phi_{RCP}$, and that we thus have a gray area in which finite size effect have a growing importance in the behaviour of the emulsion as the volume fraction increase.

Conclusions

Within this thesis we have studied the three dimensional structure of the flow of emulsion at volume fraction $\phi < \phi_{RCP}$ in microfluidic channels with a micrometric herringbone wall roughness. The use of the herringbone roughness breaks the symmetry of the channel along the longitudinal direction, as the fluid does not encounter the same geometry flowing in the direction of converging (forward) or diverging (backward) herringbone.

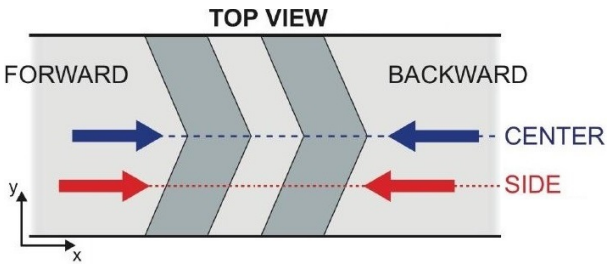

Figure 3.23: Scheme of the herringbone grooves. Picture taken from [17].

We found a difference between the flows in the two directions: the fluid is much faster while flowing in the forward direction at the center of the channel, in line with the point of the grooves. The 3d-flows have shown that this is true only at the center ($y = 0$) of the channel, as we observe an increase of the speed of the flow in the backward direction in the side of the channel. This acceleration eventually leads the backward flow to gain a higher speed than the forward one in the regions far away from the center.

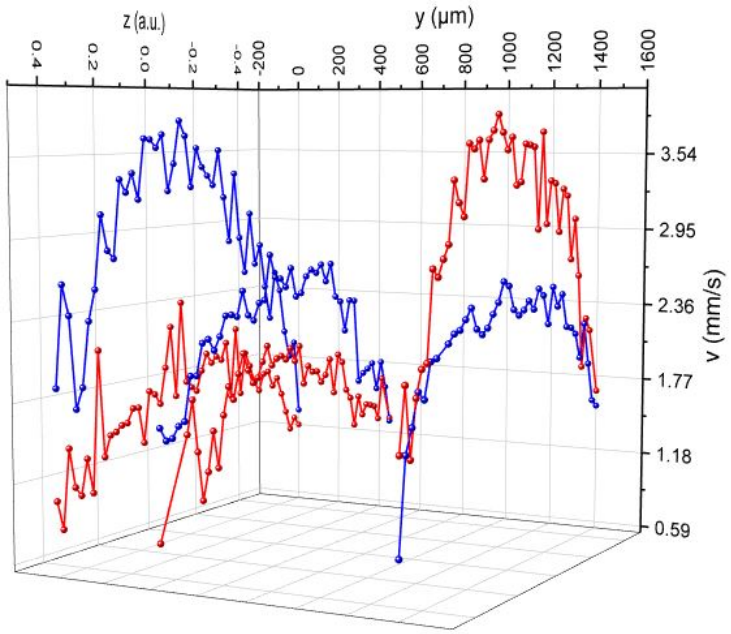

Figure 3.24: 3D scan of the $\phi = 0.6$ emulsion at $\Delta P = 200\,\text{mbar}$. In blue are the forward profiles, while in red the backward ones.

With the purpose of investigating this phenomenon, we tested pure Glycerine, a Newtonian fluid, as control, finding almost no difference in the flow in the two directions.
Continuing on this path, we tested if a shear thinning fluid like the emulsion, but lacking large finite size structures like the droplets, would show a difference in the flow in the two directions. We choose two polymeric solutions to test in the channel: the Xanthan 5000 and 2500 ppm.
The test with the Xanthan solutions has revealed that the shear-thinning rheology of the emulsion could not explain a difference of the magnitude measured for the emulsion.

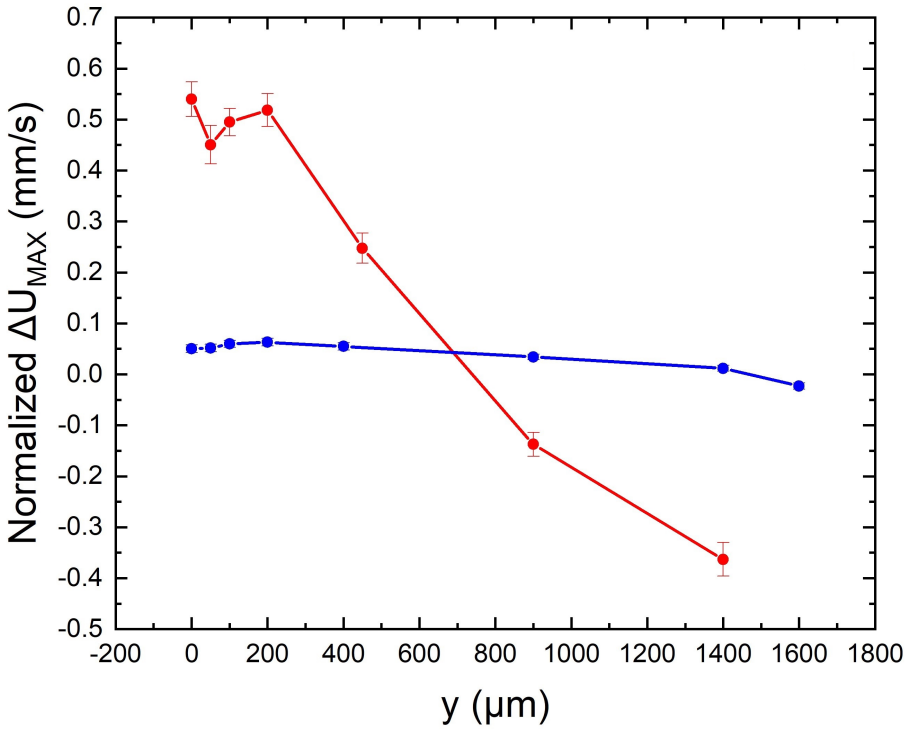

Figure 3.25: Normalized peak velocity difference ΔU_{MAX} (section 3.6) for $\phi = 0.6$ emulsion (red curve) and Xanthan 2500 ppm (blue curve) at $\Delta P = 50\,\text{mbar}$.

Those test excluded that either systematic errors of the experimental apparatus or the rheology of the emulsion could be responsible for the difference observed. This lead to hypothesize that what we observe is in fact a result of a non-local rheology induced by the finite size of the drops in the emulsion in a confined system. We suggest that the cause of the difference observed may be the same, well documented mechanisms (section 1.4) that are at the root of the non-local rheology in concentrated emulsion ($\phi > \phi_{RCP}$), a succession of elastic deformations and plastic rearrangements (finite size effects, section 1.4.3) of the droplets which can be enhanced or hindered by the wall roughness shape.
The presence of rearrangements due to finite size effect in emulsions with $\phi < \phi_{RCP}$ is a novelty not reported in literature, so far.
This result contributes to the wide research on the complex fluids flow in microfluidic channels, that has great relevance in the emerging technology of the lab-on-chip devices, providing insights to couple the fluids and the channel structures. This is expected to help designing chips that can affect only specific fluids, or selectively control their flow in a highly precise way.

Bibliography

[1] SS Abdali, Evan Mitsoulis, and NC Markatos. Entry and exit flows of bingham fluids. *Journal of Rheology*, 36(2):389–407, 1992.

[2] Birnur K Aral and Dilhan M Kalyon. Effects of temperature and surface roughness on time-dependent development of wall slip in steady torsional flow of concentrated suspensions. *Journal of Rheology*, 38(4):957–972, 1994.

[3] Wilder D Bancroft. The theory of emulsification, v. *The Journal of Physical Chemistry*, 17(6):501–519, 2002.

[4] HA Barnes and K Walters. The yield stress myth? *Rheologica acta*, 24(4):323–326, 1985.

[5] Howard A Barnes. A review of the slip (wall depletion) of polymer solutions, emulsions and particle suspensions in viscometers: its cause, character, and cure. *Journal of Non-Newtonian Fluid Mechanics*, 56(3):221–251, 1995.

[6] Lydiane Bécu, Pauline Grondin, Annie Colin, and Sébastien Manneville. How does a concentrated emulsion flow?: Yielding, local rheology, and wall slip. *Colloids and Surfaces A: Physicochemical and Engineering Aspects*, 263(1-3):146–152, 2005.

[7] CR Beverly and RI Tanner. Numerical analysis of extrudate swell in viscoelastic materials with yield stress. *Journal of Rheology*, 33(6):989–1009, 1989.

[8] Eugene Cook Bingham. *An investigation of the laws of plastic flow*. Number 278. US Government Printing Office, 1917.

[9] Robert Byron Bird, Robert Calvin Armstrong, and Ole Hassager. Dynamics of polymeric liquids. vol. 1: Fluid mechanics. 1987.

[10] Lydéric Bocquet, Annie Colin, and Armand Ajdari. Kinetic theory of plastic flow in soft glassy materials. *Physical review letters*, 103(3):036001, 2009.

[11] Peter Chadwick. *Continuum mechanics: concise theory and problems*. Courier Corporation, 2012.

[12] Rajendra P Chhabra. Non-newtonian fluids: an introduction. In *Rheology of complex fluids*, pages 3–34. Springer, 2010.

[13] Malcolm M Cross. Rheology of non-newtonian fluids: a new flow equation for pseudoplastic systems. *Journal of colloid science*, 20(5):417–437, 1965.

[14] Robert J Daniello, Nicholas E Waterhouse, and Jonathan P Rothstein. Drag reduction in turbulent flows over superhydrophobic surfaces. *Physics of Fluids*, 21(8):085103, 2009.

[15] Ladislav Derzsi, Daniele Filippi, Matteo Lulli, Giampaolo Mistura, Massimo Bernaschi, Piotr Garstecki, Mauro Sbragaglia, and Matteo Pierno. Wall fluidization in two acts: from stiff to soft roughness. *Soft matter*, 14(7):1088–1093, 2018.

[16] Ladislav Derzsi, Daniele Filippi, Giampaolo Mistura, Matteo Pierno, Matteo Lulli, Mauro Sbragaglia, Massimo Bernaschi, and Piotr Garstecki. Fluidization and wall slip of soft glassy materials by controlled surface roughness. *Physical Review E*, 95(5):052602, 2017.

[17] Daniele Filippi. Local fluidization of concentrated emulsion in microfluidic channels textured at the droplet scale. 2018.

[18] Julie Goyon, Annie Colin, and Lydéric Bocquet. How does a soft glassy material flow: finite size effects, non local rheology, and flow cooperativity. *Soft Matter*, 6(12):2668–2678, 2010.

[19] Julie Goyon, Annie Colin, G Ovarlez, A Ajdari, and L Bocquet. Spatial cooperativity in soft glassy flows. *Nature*, 454(7200):84–87, 2008.

[20] Steve Granick, Yingxi Zhu, and Hyunjung Lee. Slippery questions about complex fluids flowing past solids. *Nature materials*, 2(4):221–227, 2003.

[21] Heike Karbstein and Helmar Schubert. Developments in the continuous mechanical production of oil-in-water macro-emulsions. *Chemical Engineering and Processing: Process Intensification*, 34(3):205–211, 1995.

[22] William Kozicki, CJ Hsu, and C Tiu. Non-newtonian flow through packed beds and porous media. *Chemical Engineering Science*, 22(4):487–502, 1967.

[23] Pijush K Kundu, Ira M Cohen, and David R Dowling. Fluid mechanics, 2012.

[24] Eric Lauga, Michael P Brenner, and Howard A Stone. Microfluidics: the no-slip boundary condition. *arXiv preprint cond-mat/0501557*, 2005.

[25] Fernando Leal-Calderon, Véronique Schmitt, and Jerome Bibette. *Emulsion science: basic principles*. Springer Science & Business Media, 2007.

[26] Christopher W Macosko. Rheology principles. *Measurements and Applications*, 1994.

[27] Vincent Mansard, Lydéric Bocquet, and Annie Colin. Boundary conditions for soft glassy flows: slippage and surface fluidization. *Soft matter*, 10(36):6984–6989, 2014.

[28] Julian Marschewski, Stefan Jung, Patrick Ruch, Nishant Prasad, Sergio Mazzotti, Bruno Michel, and Dimos Poulikakos. Mixing with herringbone-inspired microstructures: overcoming the diffusion limit in co-laminar microfluidic devices. *Lab on a Chip*, 15(8):1923–1933, 2015.

[29] TG Mason, J Bibette, and DA Weitz. Elasticity of compressed emulsions. *Physical review letters*, 75(10):2051, 1995.

[30] TG Mason, J Bibette, and DA Weitz. Yielding and flow of monodisperse emulsions. *Journal of colloid and interface science*, 179(2):439–448, 1996.

[31] Y Nakayama and RF Boucher. Introduction to fluid mechanics (arnold, london, 1999).

[32] Francesco Nalin. Fluidization of concentrated emulsions in herringbones decorated microfluidic channels. 2018.

[33] C Neto, VSJ Craig, and DRM Williams. Evidence of shear-dependent boundary slip in newtonian liquids. *The European Physical Journal E*, 12(1):71–74, 2003.

[34] Chiara Neto, Drew R Evans, Elmar Bonaccurso, Hans-Jürgen Butt, and Vincent SJ Craig. Boundary slip in newtonian liquids: a review of experimental studies. *Reports on progress in physics*, 68(12):2859, 2005.

[35] QD Nguyen and DV Boger. Thixotropic behaviour of concentrated bauxite residue suspensions. *Rheologica Acta*, 24(4):427–437, 1985.

[36] Kerstin N Nordstrom, E Verneuil, PE Arratia, Anindita Basu, Zheng Zhang, Arjun G Yodh, Jerry P Gollub, and Douglas J Durian. Microfluidic rheology of soft colloids above and below jamming. *Physical review letters*, 105(17):175701, 2010.

[37] Guillaume Ovarlez, Quentin Barral, and Philippe Coussot. Three-dimensional jamming and flows of soft glassy materials. *Nature materials*, 9(2):115–119, 2010.

[38] Corey S O'hern, Leonardo E Silbert, Andrea J Liu, and Sidney R Nagel. Jamming at zero temperature and zero applied stress: The epitome of disorder. *Physical Review E*, 68(1):011306, 2003.

[39] Tasos C Papanastasiou. Flows of materials with yield. *Journal of Rheology*, 31(5):385–404, 1987.

[40] José Paredes, Noushine Shahidzadeh, and Daniel Bonn. Wall slip and fluidity in emulsion flow. *Physical Review E*, 92(4):042313, 2015.

[41] Guillemette Picard, Armand Ajdari, François Lequeux, and Lydéric Bocquet. Elastic consequences of a single plastic event: A step towards the microscopic modeling of the flow of yield stress fluids. *The European Physical Journal E*, 15(4):371–381, 2004.

[42] R Pit, H Hervet, and L Leger. Direct experimental evidence of slip in hexadecane: solid interfaces. *Physical review letters*, 85(5):980, 2000.

[43] HM Princen. Rheology of foams and highly concentrated emulsions: I. elastic properties and yield stress of a cylindrical model system. *Journal of Colloid and interface science*, 91(1):160–175, 1983.

[44] Salima Rafaï, Daniel Bonn, and Arezki Boudaoud. Spreading of non-newtonian fluids on hydrophilic surfaces. *Journal of Fluid Mechanics*, 513:77–85, 2004.

[45] R.S. Rivlin. Solution of some problems in the exact theory of visco-elasticity. *Journal of Rational Mechanics and Analysis*, 5(1):179–188, 1956.

[46] Melik Sahraoui and Massoud Kaviany. Slip and no-slip velocity boundary conditions at interface of porous, plain media. *International Journal of Heat and Mass Transfer*, 35(4):927–943, 1992.

[47] MC Sánchez, C Valencia, JM Franco, and C Gallegos. Wall slip phenomena in oil-in-water emulsions: effect of some structural parameters. *Journal of colloid and interface science*, 241(1):226–232, 2001.

[48] M Sbragaglia, R Benzi, M Bernaschi, and S Succi. The emergence of supramolecular forces from lattice kinetic models of non-ideal fluids: applications to the rheology of soft glassy materials. *Soft Matter*, 8(41):10773–10782, 2012.

[49] Johannes Schindelin, Ignacio Arganda-Carreras, Erwin Frise, Verena Kaynig, Mark Longair, Tobias Pietzsch, Stephan Preibisch, Curtis Rueden, Stephan Saalfeld, Benjamin Schmid, et al. Fiji: an open-source platform for biological-image analysis. *Nature methods*, 9(7):676–682, 2012.

[50] Johan Sjoblom. *Emulsions and emulsion stability: Surfactant science series/61*, volume 132. crc press, 2005.

[51] I Steg and D Katz. Rheopexy in some polar fluids and in their concentrated solutions in slightly polar solvents. *Journal of Applied Polymer Science*, 9(9):3177–3193, 1965.

[52] Bjørn Torger Stokke, Arnljot Elgsaeter, Gudmund Skjrak-Brjek, and Olav Smidsrød. The molecular size and shape of xanthan, xylinan, bronchial mucin, alginate, and amylose as revealed by electron microscopy. *Carbohydrate research*, 160:13–28, 1987.

[53] Abraham D Stroock, Stephan KW Dertinger, Armand Ajdari, Igor Mezić, Howard A Stone, and George M Whitesides. Chaotic mixer for microchannels. *Science*, 295(5555):647–651, 2002.

[54] HS Tang and Dilhan M Kalyon. Unsteady circular tube flow of compressible polymeric liquids subject to pressure-dependent wall slip. *Journal of Rheology*, 52(2):507–525, 2008.

[55] Jean-Yves Tinevez, Nick Perry, Johannes Schindelin, Genevieve M Hoopes, Gregory D Reynolds, Emmanuel Laplantine, Sebastian Y Bednarek, Spencer L Shorte, and Kevin W Eliceiri. Trackmate: An open and extensible platform for single-particle tracking. *Methods*, 115:80–90, 2017.

[56] Derek C Tretheway and Carl D Meinhart. Effects of absolute pressure on fluid slip in a hydrophobic microchannel. In *ASME International Mechanical Engineering Congress and Exposition*, volume 37165, pages 561–564, 2003.

[57] Derek C Tretheway and Carl D Meinhart. A generating mechanism for apparent fluid slip in hydrophobic microchannels. *Physics of Fluids*, 16(5):1509–1515, 2004.

[58] Silvia Varagnolo. Study and control of drop motion on inclined surfaces. 2016.

[59] Silvia Varagnolo, Davide Ferraro, Paolo Fantinel, Matteo Pierno, Giampaolo Mistura, Giorgio Amati, Luca Biferale, and Mauro Sbragaglia. Stick-slip sliding of water drops on chemically heterogeneous surfaces. *Physical review letters*, 111(6):066101, 2013.

[60] Silvia Varagnolo, Giampaolo Mistura, Matteo Pierno, and Mauro Sbragaglia. Sliding droplets of xanthan solutions: a joint experimental and numerical study. *The European Physical Journal E*, 38(11):126, 2015.

[61] Lucia Villanova. Plasticita direzionale indotta da canali microfluidici strutturati. 2019.

[62] Stoyan Yordanov, Andreas Best, Hans-Jürgen Butt, and Kaloian Koynov. Direct studies of liquid flows near solid surfaces by total internal reflection fluorescence cross-correlation spectroscopy. *Optics Express*, 17(23):21149–21158, 2009.